



HAL
open science

Transport properties of internal gravity waves

Ernesto Horne Iribarne

► **To cite this version:**

Ernesto Horne Iribarne. Transport properties of internal gravity waves. Atmospheric and Oceanic Physics [physics.ao-ph]. Ecole normale supérieure de lyon - ENS LYON, 2015. English. NNT : 2015ENSL1027 . tel-01244324

HAL Id: tel-01244324

<https://theses.hal.science/tel-01244324>

Submitted on 15 Dec 2015

HAL is a multi-disciplinary open access archive for the deposit and dissemination of scientific research documents, whether they are published or not. The documents may come from teaching and research institutions in France or abroad, or from public or private research centers.

L'archive ouverte pluridisciplinaire **HAL**, est destinée au dépôt et à la diffusion de documents scientifiques de niveau recherche, publiés ou non, émanant des établissements d'enseignement et de recherche français ou étrangers, des laboratoires publics ou privés.



THÈSE

en vue d'obtenir le grade de:

**Docteur de l'Université de Lyon,
délivré par l'École Normale Supérieure de Lyon**

Spécialité : **Physique**

**Laboratoire de Physique de l'ENS de Lyon
École Doctorale de Physique et d'Astrophysique de Lyon**

Soutenance prévue le 29 Octobre 2015 par:

Ernesto HORNE IRIBARNE

Transport properties of internal gravity waves

Directeur de thèse:

Philippe ODIER

Co-encadrant:

Sylvain JOUBAUD

M. Michael LE BARS	Chargé de recherche au CNRS, IRPHE	Rapporteur
M. Marc RABAUD	Professeur, FAST - Université Paris-Sud	Rapporteur

Devant la commission d'examen formé de :

M. Robert ECKE	Directeur du CNLS, Los Alamos, USA	Examineur
Mme. Patricia ERN	Directrice de recherche au CNRS, IMFT	Examineur
M. Sylvain JOUBAUD	Maître de conférence, ENS de Lyon	Co-encadrant
M. Michael LE BARS	Chargé de recherche au CNRS, IRPHE	Rapporteur
M. Stéphane LABROSSE	Professeur, ENS de Lyon	Examineur
M. Philippe ODIER	Maître de conférence, ENS de Lyon	Directeur
M. Marc RABAUD	Professeur, FAST - Université Paris-Sud	Rapporteur

Acknowledgements

I would like to thank my two supervisors Philippe and Sylvain, each one with a different approach allowed me to evolve in the highly exploratory subject of my thesis, always at disposal for meetings and answering questions. I thank you for the freedom you gave me to attack new problems under my point of view and for rescuing me when ever I got stuck in a dead end. The knowledge acquired during the last three years will stay with me for a long time. For all this I thank you.

I thank the rapporteurs of this thesis, Marc Rabaud and Michael Le Bars for the interest they showed on my work. Their remarks help me to improve the quality of this work. I also highly appreciate the many suggestions of Robert Ecke and the participation of Patricia Ern and Stéphane Labrosse as members of the committee of my thesis defense.

In the course of my thesis I had the opportunity to perform collaborative work with Jeremy and Nelly that allowed to increase the accuracy of the analysis of my measurements, and most important, taught me how to work with researchers of a different field, for that I am thankful. In addition, I thank Diane for the months we spend working on the same experiment and for the exchange of ideas, I am glad we will continue to work together.

The last three years of journey in the Laboratoire de Physique de l'ENS Lyon has not been only an academic experience, it has also been a very strong and fruitful personal one. There are many people I would like to thank, I consider this is a good opportunity to do it.

My integration to the Internal waves group was facilitated thanks to the rich human environment forming the group. In particular, I had the pleasure to learn from Baptiste Bourget the experimental handling in the Lab, who always showed me disposition for answering questions. I would like to thank also H el ene for the many mails with lines of codes that saved me in many occasions. The advice received from Thierry, in conjunction with the meetings he organized with researchers visiting the laboratory, allowed me to expand my vision on various topics related to the subject of my thesis. In addition the conversations with Chris, Evgeny, Yvan, Paco and Antoine allowed me to interchange ideas and enhanced my perception in the field.

I feel very lucky to have landed in the Laboratoire de Physique of the ENS Lyon. The friendly ambiance extends to all the Lab, from the mechanic and electronic workshop, to the informatics, the PSMN, and the secretary team, always happy to help. Many members of the Lab are sport lovers, I enjoyed very much the bike tours done with Philippe, the football matches played and watched with Angel, Thierry, Sylvain, Patrick and Thomas, and the climbing with Nico, Chris, Ronan. Every lunch and coffee pause is pleasant in the Lab, generating a rich space for exchange, for that I thank Rytis, Michel, Chris P., Chris

B., Pierre, Thibaud, Stephan, the SiSyPhe group: Nico, Ronan, Jordan, Roberto, Gabriel and Rodrigo, for the nice moments.

I always had a nice company in the office, for that I thank H el ene, Yvan, Anne, Tess (also for watering the plants), Yiu, Franco, Timoth ee, Antoine.

It was great to meet Sarah and Albert, great company from the beginning until this moment.

My first communication with the Lab was through Mickael Bourgoin, I thank you for your interest and predisposition.

I am very thankful for the multiples triangular discussions with Baptiste and Marc-Antoine whether in the terrace or in the mountain. They allowed to extend our scientific curiosity to any other field. And I thank you both for the advices you gave me respect to my thesis work.

My "colocs" supported me all this time, thanks Perico, Pia, Fode, Mathieu and Fanny.

My curiosity for the ocean and atmosphere has been strongly marked by the travel I did with Brice Mon egie in Podorange, and has been updated by Dario "Polaco" Obere and the Fuga, I hope others trips will come.

I thank my family, that from far away always supported me in my journey.

Contents

Motivation	1
1 Introduction to internal gravity waves	3
1.1 Physics of internal gravity waves	4
1.1.1 Stable density profile and restoring force	4
1.1.2 Linear internal waves	5
1.1.3 Vertical modes	9
1.1.4 Reflection of internal gravity waves	10
1.2 Internal waves in the atmosphere and ocean	13
1.2.1 Stratification of the ocean and the atmosphere	13
1.2.2 Generation of internal waves in the ocean	15
1.2.3 Internal waves near oceanic seafloor	16
2 Internal gravity waves in the laboratory, techniques and implements	17
2.1 Laboratory: experimental techniques	18
2.1.1 Double bucket method	18
2.1.2 Density measurements	19
2.1.3 Generation of internal waves	20
2.1.4 Visualization techniques	24
2.2 Image processing techniques	26
2.2.1 Temporal filtering	26
2.2.2 Hilbert transform	27
2.3 Perspectives	27
3 Sediment transport	29
3.1 Introduction	30
3.2 Physics of erosion, transport and sedimentation of particles in a fluid	31
3.2.1 Sediment transport	31
3.2.2 Shields dimensionless number	32
3.2.3 Particles sedimentation	34
3.3 Conditions in the Laboratory	38
3.4 Results	41
3.4.1 Particles in a mountain-shaped pile	41
3.4.2 Particles in a horizontal and inclined bed	46
3.5 Conclusions of bed load transport	49

4	Internal waves reflection	51
4.1	Critical reflection: Singularity and localization of the reflected wave	52
4.2	Experimental setup and system description	52
4.2.1	Schematic configuration and coordinate systems	52
4.2.2	Experimental setup	53
4.3	Observations and post-processing	54
4.3.1	Temporal filtering	55
4.3.2	Spatial selection and Hilbert transform	56
4.3.3	Variational mode decomposition method (VMD)	58
4.3.4	VMD spectral analysis	60
4.3.5	HT vs VMD and improved VMD	61
4.3.6	Extraction of the incident velocity	64
4.4	Weakly non-linear near critical reflection: Dauxois Young model	66
4.4.1	Dimensional analysis	66
4.4.2	Near critical approximation	68
4.4.3	Inner region	68
4.5	Results	69
4.5.1	Critical reflection: upward wave, downward wave or both?	69
4.5.2	Intensity of the reflected wave	72
4.5.3	Dauxois & Young model: comparison with experiments	74
4.5.4	Shear stress and Shields number	75
4.5.5	Vertical mode reflections	77
4.5.6	Shields and Reynolds numbers	78
4.6	Conclusions	82
5	Particles in suspension	85
5.1	Suspended particles: nature and experiments	86
5.2	Experimental setup and system description	86
5.2.1	System description	86
5.2.2	Experimental setup	86
5.2.3	Particle injector	87
5.2.4	Generation of the column	89
5.2.5	Particles distribution and concentration	89
5.3	Dynamics of the column	90
5.3.1	Formation of the column	90
5.3.2	Evolution of the concentration in the column	90
5.4	Effect of the column over waves	92
5.5	Effect of the waves over the column	95
5.5.1	Oscillation of the column	96
5.5.2	Displacement of the column	98
5.6	Drift generated by internal waves	102
5.6.1	Analysis of the Lagrangian drift	105
5.6.2	Drift estimation for experiments	106
5.7	Conclusions	110
6	Conclusion	111
	Bibliography	115

Motivation

The object of the present work is to investigate experimentally several aspects of the interaction between internal gravity waves and their surrounding medium. In particular, we study the effect of internal waves over particles either, settled at a boundary or in suspension in a fluid. In order to appreciate why the transport properties of internal waves are relevant, it is pertinent to situate internal waves in their natural geophysics context: the atmosphere and the ocean.

Internal gravity waves propagate in stratified environments. The ocean and the atmosphere having this property are a suitable medium for these waves. In the atmosphere, internal waves are principally produced by the passage of wind over topography. In the ocean, the main generation of internal waves is produced by tide forcing over the seafloor [74]. Nevertheless, internal waves can also be generated in the ocean by the interaction with the atmosphere through surface processes as for example large scale thunderstorms [21].

When internal gravity waves interact with oceans boundaries, it is possible to observe strong increases of the velocities respect to their mean value [4]. In particular, when the angle of the bottom seafloor and the angle of propagation of the wave's energy coincide (named critical reflection), it is known that there will be a focalization of the wave and therefore an amplification. This effect has been shown theoretically, [57, 69, 19, 63], verified experimentally [37, 20, 18] and numerically [15, 64], as well as measured in the ocean [29, 44, 53].

The strong bottom shear generated by internal waves reflection can be a possible mechanism of erosion of the seafloor. The reflection of internal waves can, as well, generate turbulence mixing [41, 44, 15, 64], affecting the global oceanic energy budget. Nevertheless, the main interest of this work is centered in the properties of erosion and transport of matter generated by internal waves. In fact, many observational studies indicate that internal gravity waves are a cause of sediment resuspension [40, 5, 11, 59].

Reflections of internal waves can occur by remotely generated waves, or by tidal forcing over sloped topography. In this last case, bottom velocities and bottom shear stresses should be highest where the slopes are critical [24, 76]. This will occur for a specific combination of forcing frequency (semi-diurnal tide) and gradient of density. Therefore, the increase of bottom shear produced by critical reflections generates a feedback process: erosion will be favored to occur for critical angles, and at the same time, the erosion will produce larger regions suitable for the waves to be critical over the slope. In consequence, the angles of energy propagation of semidiurnal internal tides may determine the average gradient of continental slopes in ocean basins (~ 2 to 4 degrees) [12]. In addition, when shear velocities are high enough they can inhibit deposition of fine-grained sediment onto the slopes.

Thesis plan

We propose an experimental study of internal gravity waves for conditions that mimic oceanic situations where erosion and transport of particles may occur. The order in which this work is presented follows chronologically the order in which experiments have been performed. This is a consequence of the explorative character of this investigation.

The propagation of internal waves occur exclusively in stratified fluids. In chapter 1 we introduce the notion of buoyancy restoring force in stratified systems, that lead to the generation of internal waves when perturbed under specific conditions. The principal physical aspects of internal gravity waves are then introduce, in particular the special case of internal waves reflection. We present the conditions of atmospheric and oceanic systems and how internal waves propagate in them, given that one of the main motivation of this work relies on the existence of internal waves processes in geophysical systems.

The study of internal waves has been performed through the realization of experiments. In the second chapter we introduce the main techniques to produce the appropriate conditions for the generation and visualization of internal waves in a well controlled environment in the Laboratory.

In chapter 3 we introduce the principals features of granular motion, in particular, we introduce the physical conditions necessary for motion initiation of settled particle in a fluid. Explorative experiments developed to study the motion of particles induced by internal gravity waves, are presented, where no bed load transports was observed.

The limitations of internal waves in generating bed load transport in the laboratory, motivated us to performed a detailed study of a particle configuration of internal waves reflection, called critical reflection, which is presented in chapter 4. This reflection occurs when the angle of inclination of a boundary slope coincides with the direction of propagation of the waves, in consequence a intense focalization is produced at the proximities of the boundary, enhancing the capability of producing erosion. In order to effectuate an accurate separation of the wavefield in the proximities of the boundary, a signal processing method has been developed in a collaborative work, and is presented in this chapter. The high resolution measurements combined to the post-processing techniques allowed to compare our results with a theory in internal waves near-critical reflections. This comparison shows that the theory predicts fairly well our experimental results. This theory allows us to perform extrapolation to experimental configurations beyond our experiments and to oceanic situations.

In chapter 5 we describe the study performed for the interaction of internal gravity waves and particles in suspension. We describe a technique developed to generate a column of settling particles. We measured the effect that many particles in suspension have over the propagation of internal waves, and we studied the effect that the waves produce over the column of particles. We observed that the particles can be driven by the waves generating oscillatory trajectories and in some cases generating a net displacement of the particles. A model is proposed which describes qualitatively the displacement of the particles induced by internal gravity waves.

Introduction to internal gravity waves



Wave cloud pattern in southern Algeria. Source: Wikipedia.

A stratified environment is a medium that changes its thermodynamics properties (as temperature, salinity, density, velocity, momentum) with its vertical location. When difference of density exists within a fluid, it will tend to redistribute driven by the force of gravity so that the lighter fluid remains above the heavier forming a stable stratification profile. This particular configuration will be stable in time and if not perturbed, static. When the fluid is slightly vertically displaced, it will feel a buoyancy restoring force acting in a direction opposite to the displacement. The force will act as a spring, and therefore the fluid will oscillate around an equilibrium position.

These oscillations are know as internal gravity waves, which differ from the well known surface waves, as they occur inside the fluid where the density of the fluid changes continuously.

The atmosphere is stratified in temperature, and the ocean is stratified in both salinity and temperature. Our main motivation for understanding the dynamics of internal gravity waves is that they occur naturally in these systems. These waves have an effect over the dynamics of stratify systems, and may be taken into account to be able to better predict large scale effects such as transport of energy and matter.

1.1 Physics of internal gravity waves

We will introduce the analytical elements necessary to describe internal gravity waves. We will estimate the forces involved in a stably stratified fluid, and deduced the existence of a restoring force, when the fluid is displaced from its equilibrium position. Force that allows the existence of oscillatory processes, that as will be shown, can be described by waves, under the linear and Boussinesq approximation. The effect of viscous dissipation and diffusive processes over internal waves will be studied. Internal waves own a peculiar dispersion relation that results in nonintuitive properties, in particular when a wave reflects over a solid boundary. We will present special attention to this latest process, as it will be further studied experimentally.

1.1.1 Stable density profile and restoring force

A stratified fluid is a fluid for which its density changes with position. Under gravity, fluid parcels of various densities will arrange in a way that the higher densities are found below lower densities. This effect will generate a vertical layering, leading to an anisotropic medium.

Leaving aside the reorganization and dynamics of a stratified fluid into a vertically stratified fluid, let us consider the static equilibrium in the latter situation. The lack of motion requires the absence of lateral forces, and therefore horizontal homogeneity. The mechanic equilibrium of this fluid relies in the equilibrium between the gravity force and the pressure force, that is, the local hydrostatic relation,

$$\frac{\partial P}{\partial z} = -\bar{\rho}(z)g, \quad (1.1)$$

where g is the acceleration of the gravity, $\bar{\rho}$ the local density of the fluid in repose and P the pressure over the fluid. The direction of the vertical axis, z is upwards, opposite to the direction of the acceleration of the gravity.

If we consider a fluid parcel of density ρ_1 , then the action of the hydrostatic pressure over the fluid parcel can be interpreted, through Archimedes principle, as a vertical force equal to the weight of the volume of the displaced fluid. In units of volume this force is,

$$\mathbf{F}_p = \bar{\rho}(z)\mathbf{g}. \quad (1.2)$$

In addition to this force there is the gravity force, in units of volume $\mathbf{F}_g = \rho_1\mathbf{g}$. The balance of forces is then,

$$\sum_i \mathbf{F}_i = \mathbf{F}_g + \mathbf{F}_p = (\bar{\rho}(z) - \rho_1)\mathbf{g}. \quad (1.3)$$

A fluid parcel will then go upwards if it is lighter than the surrounding fluid, and will go downward when heavier. This balance of forces explains why stable stratified fluid density increases in the direction of \mathbf{g} .

In the case that the fluid parcel have the same density as the surrounding fluid, then the resulting forces will be null and the fluid parcel will be at equilibrium. If this balance is produced at height z_1 such that, $\bar{\rho}(z_1) = \rho_1$, then when displaced δz from the position z_1 , Newton's laws predict the consequent motion of the fluid parcel dynamics,

$$\rho_1 \frac{d^2 \delta z}{dt^2} = (\bar{\rho}(z_1 + \delta z) - \rho_1)g. \quad (1.4)$$

Assuming small displacements δz of the fluid parcel, and recalling that $\bar{\rho}(z_1) = \rho_1$, we obtain,

$$\frac{d^2\delta z}{dt^2} = \frac{\bar{\rho}(z_1 + \delta z) - \bar{\rho}(z_1)}{\bar{\rho}(z_1)} \quad (1.5)$$

$$= \frac{g}{\bar{\rho}(z_1)} \left. \frac{d\bar{\rho}}{dz} \right|_{z_1} \delta z, \quad (1.6)$$

$$= -N^2(z_1)\delta z. \quad (1.7)$$

Equation (1.7) is the differential equation of a harmonic oscillator of frequency N , called the buoyancy frequency. The vertically displaced fluid parcel in a stratified fluid feels a buoyancy restoring force acting in the opposite direction of the displacement.

In general, the buoyancy frequency is defined as,

$$N^2(z) = -\frac{g}{\rho_0} \left. \frac{d\bar{\rho}}{dz} \right|_z, \quad (1.8)$$

where $\rho_0 = \langle \bar{\rho} \rangle$ is the averaged density¹. The value of the buoyancy frequency will be real when the density increases in the direction of \mathbf{g} , and imaginary when the density decreases in the direction of \mathbf{g} , and therefore, unstable. The buoyancy frequency N , therefore, characterizes the gradient of density of a stratified fluid. When N is large, the stratification is strong, and when N is small, the stratification is weak. A perturbation of the fluid within a stratified medium generates an oscillation that will persist until its dissipated by viscosity.

1.1.2 Linear internal waves

The oscillatory perturbations that propagate in a stratified fluid are called internal waves. We will describe under which conditions these waves arises from the equation of motion. We consider an incompressible stratified fluid characterized by a buoyancy frequency N . Under this condition the Navier-Stokes equation in a non-rotating frame is

$$\frac{\partial \mathbf{u}}{\partial t} + (\mathbf{u} \cdot \nabla) \mathbf{u} = \mathbf{g} - \frac{\bar{\rho}}{\rho} \mathbf{g} - \frac{1}{\rho} \nabla P + \nu \nabla^2 \mathbf{u}, \quad (1.9)$$

the incompressibility of the fluid implies,

$$\nabla \cdot \mathbf{u} = 0, \quad (1.10)$$

and the conservation of mass is represented by

$$\frac{\partial \rho}{\partial t} + \mathbf{u} \cdot \nabla \rho = \kappa \nabla^2 \rho, \quad (1.11)$$

where $\mathbf{u} = (u, v, w)$ is the velocity of the fluid in cartesian coordinates, ν is the kinetic viscosity of the fluid and κ is the mass diffusion coefficient of the stratifying agent (temperature or salinity). The density $\rho = \bar{\rho} + \rho'$ is expressed as the addition of a term associated with the average density $\bar{\rho}$, and a term associated to the fluctuations of density ρ' .

We will work in the simplified case in which the flow is two-dimensional and contained in the plane (xOz), that is, there is no variations along (Oy). Under this assumption, the

¹Equation (1.8) is derived assuming that density is independent of pressure, which is not true for extreme deep ocean conditions.

velocity field can be expressed by the streamfunction ψ , so that $(u, w) = (-\partial_z\psi, \partial_x\psi)$. We can then rewrite equations (1.9) and (1.11) as,

$$\partial_{tz}\psi + J(\partial_z\psi, \psi) = -\frac{1}{\rho}\partial_x P + \nu\partial_z\nabla^2\psi, \quad (1.12)$$

$$\partial_{tx}\psi + J(\partial_x\psi, \psi) = \frac{\rho'}{\rho}g\partial_z P + \nu\partial_x\nabla^2\psi, \quad (1.13)$$

$$\partial_t\rho' + J(\rho', \psi) = \kappa\nabla^2\rho' + \frac{d\bar{\rho}}{dz}\partial_x\psi, \quad (1.14)$$

where J is the Jacobian defined by $J(f, g) = \partial_x f \partial_z g - \partial_z f \partial_x g$.

In the limit where the fluctuations of density vary by a small fraction with respect to its average value, that is, $\rho' \ll \bar{\rho}$ and $\bar{\rho} \approx \langle \bar{\rho} \rangle = \rho_0$, it is convenient to assume the Boussinesq approximation. This is justified for the range of densities used in our experiments, between $\rho = 1000 \text{ g}\cdot\text{L}^{-1}$ and $\rho = 1050 \text{ g}\cdot\text{L}^{-1}$, where we observe variations of the density of the order of $\text{g}\cdot\text{L}^{-1}$. In the Navier-Stokes equation, this approximation implies differences of densities are sufficiently small to be neglected, except where they appear in terms multiplied by the acceleration of the gravity g .

In addition to the Boussinesq approximation, we performed the x derivative over equation (1.12), and the z derivative over equation (1.13), so that when both terms are added, the pressure contributions will cancel each other. Equations (1.12-1.14) reduce to,

$$\partial_t(\nabla^2\psi) + J(\nabla^2\psi, \psi) - \nu\nabla^2(\nabla^2\psi) = \frac{g}{\rho_0}\partial_x\rho' \quad (1.15)$$

$$\partial_t\rho' + J(\rho', \psi) - \kappa\nabla^2\rho' = -N^2\frac{\rho_0}{g}\partial_x\psi. \quad (1.16)$$

This system describes the non-linear dynamics of a viscous stratified fluid, where the stratifying agent diffuses in time. We will neglect the non-linear terms of equations (1.15) and 1.16 in order to study the dynamics of linear waves. The system of equations are then,

$$\partial_t(\nabla^2\psi) - \nu\nabla^2(\nabla^2\psi) = \frac{g}{\rho_0}\partial_x\rho' \quad (1.17)$$

$$\partial_t\rho' - \kappa\nabla^2\rho' = -N^2\frac{\rho_0}{g}\partial_x\psi. \quad (1.18)$$

We search for plane wave type solutions, that is, $\psi = \Psi_0 e^{i(\omega t - \mathbf{k}\cdot\mathbf{x})}$ and $\rho' = \rho'_0 e^{i(\omega t - \mathbf{k}\cdot\mathbf{x})}$. The system of equations (1.17) and (1.18) can be written in a matrix form,

$$\begin{pmatrix} -|\mathbf{k}|^2(i\omega + \nu|\mathbf{k}|^2) & i\frac{g}{\rho_0}k_x \\ iN^2\frac{\rho_0}{g}k_x & i\omega + \kappa|\mathbf{k}|^2 \end{pmatrix} \begin{pmatrix} \psi \\ \rho' \end{pmatrix} = \begin{pmatrix} 0 \\ 0 \end{pmatrix}, \quad (1.19)$$

where we have used the explicit form of $\mathbf{k} = (k_x, k_z)$ and $|\mathbf{k}| = \sqrt{k_x^2 + k_z^2}$. This system presents non trivial solution only if the determinant in the matrix containing the ω and \mathbf{k} is null, that is,

$$|\mathbf{k}|^2(i\omega + \nu|\mathbf{k}|^2)(i\omega + \kappa|\mathbf{k}|^2) + N^2k_x^2 = 0. \quad (1.20)$$

Equation (1.20) is the full solution of the dispersion relation for linear internal plane waves propagating in a stratified fluid. We will present some limiting cases for which diffusion and viscosity can be neglected.

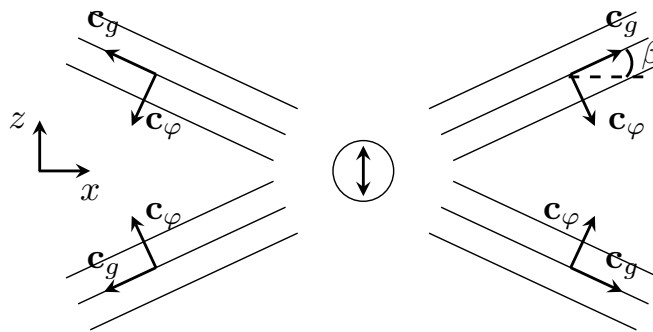


Figure 1.1: The four possible configurations of internal wave beams created by an oscillating body at fixed frequency.

Non-viscous and non-diffusive fluid

We will proceed to describe the case of a fluid where dissipative effects, such as diffusion and viscosity, are negligible. In this case, equation (1.20) is reduced to,

$$\left(\frac{\omega}{N}\right)^2 = \frac{k_x^2}{\mathbf{k}^2} \quad i.e. \quad \frac{\omega}{N} = \pm \frac{|k_x|}{|\mathbf{k}|}. \quad (1.21)$$

This relationship can be rewritten in the form,

$$\frac{\omega}{N} = \pm \sin \beta \quad (1.22)$$

where β is the angle between the wavenumber and the vertical.

For a given frequency, the four possible internal plane waves satisfying equation (1.22) (or equation (1.21)) have wavenumbers, $(\pm k_x, \pm k_z)$, and are shown in figure 1.1. The wavelength of the internal waves will be imposed by the size of the forcing oscillation, since the dispersion relation explicits the direction of propagation of the wave but not its wavelength.

The dispersion relation contains the anisotropic character of the internal waves. The group and phase velocities are, respectively,

$$\mathbf{c}_g = \pm N \frac{|k_x|}{|\mathbf{k}|^3} \mathbf{k}, \quad (1.23)$$

$$\mathbf{c}_\varphi = \pm N \frac{\text{sign}(k_x) k_z}{|\mathbf{k}|^3} (k_z, -k_x), \quad (1.24)$$

We obtain, therefore, that the group and phase velocities have a peculiar relationship: the group velocity is perpendicular to the phase velocity (or to the wavenumber \mathbf{k}). In particular the vertical component of the group velocity is always opposite to the vertical component of the phase velocity, as shown in figure 1.1. Waves that appear to be propagating their phase upwards will be propagating their energy downwards, and vice versa. Energy travels along the crests and valleys and not perpendicular to them. The angle β can also be seen as the angle between the horizontal and the group velocity of the waves \mathbf{c}_g .

Internal waves in a viscous fluid

When taking into account the viscosity of the fluid, and yet neglecting diffusivity, the dispersion relation of equation (1.20) becomes,

$$\left(\frac{\omega}{N}\right)^2 - i\nu\frac{\mathbf{k}^2}{N}\left(\frac{\omega}{N}\right) - \frac{k_x^2}{\mathbf{k}^2} = 0. \quad (1.25)$$

The discriminant of this second order polynomial for ω/N is,

$$\Delta = -\nu^2\frac{\mathbf{k}^4}{N^2} + 4\frac{k_x^2}{\mathbf{k}}. \quad (1.26)$$

Depending on the values of the horizontal and vertical component of the wavenumber \mathbf{k} , the discriminant may be positive or negative for a fixed viscosity ν . The discriminant will be determined if the roots of the polynomial (and therefore the value of ω/N) are complex or purely imaginary. If $\Delta < 0$, ω/N is purely imaginary, and the wave will be evanescent. If $\Delta > 0$, ω/N will present an imaginary and a real part. For the latter case, the frequency can be written as

$$\omega = \omega_r + i\omega_i, \quad (1.27)$$

where

$$\omega_r = \pm N\sqrt{\frac{k_x^2}{\mathbf{k}^2} - \frac{\nu^2\mathbf{k}^4}{4N^2}}, \quad \text{and} \quad \omega_i = \frac{\nu\mathbf{k}^2}{2}. \quad (1.28)$$

The viscosity not only generates the appearance of an imaginary frequency, it also modifies its real part. Nevertheless, for the range of wavenumbers employed in our experiments, the real part of the frequency will be modified less than 1% because of viscosity.

The imaginary part of the frequency is responsible for viscous attenuation of the wave. In a right-handed coordinate system attached to the wave² (η, ξ), where η is in the direction of \mathbf{c}_g . In this coordinate system the wave will be,

$$\psi = \Psi_0 e^{i(\omega t - |\mathbf{k}|\xi)}, \quad (1.29)$$

where the propagation of the wave is such that, $\eta = \mathbf{c}_g t$, and $\mathbf{c}_g = N|k_z|/\mathbf{k}^2$. The contribution of the imaginary part of the frequency will be given by the term $e^{-\omega_i t}$, where,

$$\omega_i t = \omega_i \frac{\eta}{\mathbf{c}_g}, \quad (1.30)$$

$$= \frac{\nu|\mathbf{k}|^3}{2\sqrt{N^2 - \omega^2}}\eta. \quad (1.31)$$

The plane wave can be rewritten in the attached coordinates as,

$$\psi = \Psi_0 e^{-\Lambda\eta} e^{i(\omega t - |\mathbf{k}|\xi)}, \quad (1.32)$$

where $\Lambda = \frac{|\mathbf{k}|^3}{2\sqrt{N^2 - \omega^2}}$, preferentially attenuates the higher wavenumbers (or shorter wavelengths) for a fixed frequency ω .

²The coordinates (η, ξ) attached to the wave will be used repeatedly in this work.

Internal waves in a viscous, diffusive fluid

When diffusion of the stratifying agent is considered, the polynomial on ω/N becomes,

$$\left(\frac{\omega}{N}\right)^2 - i(\nu + \kappa)\frac{\mathbf{k}^2}{N}\left(\frac{\omega}{N}\right) - \left(\nu\kappa\frac{\mathbf{k}^4}{N^2} + \frac{k_x^2}{\mathbf{k}^2}\right) = 0. \quad (1.33)$$

The determinant of this polynomial is,

$$\Delta = -\nu^2 \left(1 + \frac{1}{Sc}\right)^2 \frac{\mathbf{k}^4}{N^2} + 4\frac{k_x^2}{\mathbf{k}^2}, \quad (1.34)$$

where the Schmidt number, $Sc = \nu/\kappa$ compares the viscous and the diffusive effects. Thus, for salt water $Sc \sim 700$, the determinant can be considered as equal to the determinant computed for a viscous non-diffusive fluid.

In the studies presented in this work we will neglect diffusive effects in the fluid.

1.1.3 Vertical modes

We have previously searched for plane wave type solutions, considering that the surrounding medium is arbitrary large. In the ocean and atmosphere, internal waves are vertically confined. We will search for a wave solution of the vertical mode type, that is,

$$\Psi = \Psi_0 f(z) \exp(i(\omega t - k_x x)). \quad (1.35)$$

For a non-viscous and non-diffusive fluid, equations (1.17) and (1.18) can be reduced to the expression,

$$\partial_{tt}\nabla^2\Psi + N^2\partial_{xx}^2\Psi = 0. \quad (1.36)$$

For the vertical mode type solutions we obtain,

$$\frac{d^2f}{dz^2} + k_x^2 \left(\frac{N^2}{\omega^2} - 1\right) f(z) = 0. \quad (1.37)$$

We will impose that the fluid cannot traverse the vertical boundaries (at $-H/2$ and $H/2$), and therefore have null vertical velocity at these vertical locations. These conditions are satisfied if $f(-H/2) = 0$ and $f(H/2) = 0$. The functions f satisfying the differential equation and the boundaries conditions are,

$$f_n(z) \propto \cos\left((2n+1)\frac{\pi}{H}z\right), \quad (1.38)$$

where n is an integer number. The full solution for the vertical mode will correspond to the superposition of all the solutions f_n ,

$$\Psi = \sum_{n=0}^{\infty} A_n \cos(k_{zn}z) e^{i(\omega t - k_{xn}x)}, \quad (1.39)$$

where A_n are integration constants, $k_{zn} = (2n+1)\pi/H$ and k_{xn} is calculated through the dispersion relation (equation 1.21).

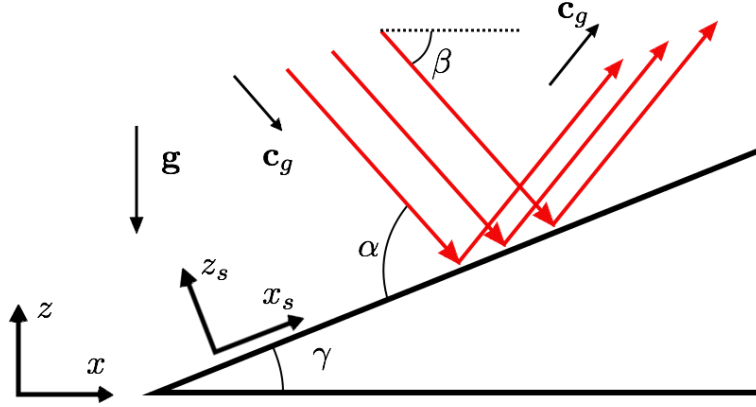


Figure 1.2: Schematic view of an internal wave reflection. The angle between the bottom slope and the horizontal is γ ; the angle between the incident group velocity and the horizontal is β , and $\alpha = \gamma + \beta$. \mathbf{c}_g indicates the group velocity and \mathbf{g} indicates gravity. The horizontal and vertical axis, as well as the axis attached to the slope, are indicated.

This solution represents a stationary wave over the vertical coordinate and propagative over the horizontal coordinate. Moreover, each mode can be decomposed as the superposition of two plane waves with wavenumbers, $\mathbf{k}_{n\uparrow} = (k_{xn}, k_{zn})$ and $\mathbf{k}_{n\downarrow} = (k_{xn}, -k_{zn})$, one going upwards and one going downwards.

In this work we will use the vertical mode associated with $n = 0$, for this case the horizontal and vertical velocities are respectively,

$$u = u_0 \sin\left(\frac{\pi}{H}z\right) \cos(\omega t - k_x x), \quad (1.40)$$

$$w = w_0 \cos\left(\frac{\pi}{H}z\right) \sin(\omega t - k_x x), \quad (1.41)$$

where $k_x u_0 = w_0 \pi / H$, the relation between the horizontal and vertical velocity is obtained from the incompressibility relation.

1.1.4 Reflection of internal gravity waves

The peculiar dispersion relation and the nonintuitive relation between group velocity and the wavenumber lead to some very unusual physical consequences. In particular, when internal waves are reflected on a sloped boundary the frequency is conserved, and therefore, its angle of propagation. In consequence, nonintuitive effects including reflection, focalization and wave attractors [45, 62, 17] will emerge when internal waves interact with boundaries. In the following, we will formally introduce the linear theory of internal wave reflections. This process will be extensively studied through experiments in this work (see chapter 4).

Inviscid incident wave

The linear theory of internal waves reflection was first developed by Phillips [57]. This theory is based on having a known incident wave reflecting at a sloped boundary [56]. For simplicity let us consider a two-dimensional non-viscous incident plane wave propagating in a linearly stratified fluid characterized by the buoyancy frequency N . The representation of this wave by the streamfunction is,

$$\psi^{inc}(\mathbf{r}, t) = \Psi^{inc} e^{i(\mathbf{k}^{inc} \mathbf{r} - \omega^{inc} t)}, \quad (1.42)$$

where the superscripts *inc* refer to the incident wavefield, and \mathbf{k}^{inc} and ω^{inc} satisfy the dispersion relation (1.22). The representation of an internal wave reflection is sketched in figure 1.2.

Boundary conditions

The solid boundary at which the reflection takes place satisfies $z = x \tan \gamma$, where γ is the angle of inclination of the slope with respect to the horizontal. The reflected wave has unknown frequency ω^{refl} and wavenumber \mathbf{k}^{refl} . Nevertheless, we know that the reflected wave satisfies the dispersion relation of equation (1.22). We can write the reflected wave, generally, as

$$\psi^{refl}(\mathbf{r}, t) = \Psi^{refl} e^{i(\mathbf{k}^{refl} \mathbf{r} - \omega^{refl} t)}. \quad (1.43)$$

The complete wavefield is therefore given by,

$$\psi = \psi^{inc} + \psi^{refl}. \quad (1.44)$$

In the non-viscous case, the boundary condition is satisfied when the normal to boundary flow is null at the boundary.

We define the attached to slope coordinates (x_s, z_s) , which simplifies the description of the boundary conditions. This coordinates system can be obtained by performing a counterclockwise rotation of (x, z) by an angle γ , explicitly,

$$\begin{bmatrix} x_s \\ z_s \end{bmatrix} = \begin{bmatrix} \cos \gamma & \sin \gamma \\ -\sin \gamma & \cos \gamma \end{bmatrix} \begin{bmatrix} x \\ z \end{bmatrix}. \quad (1.45)$$

The boundary for this coordinate system is therefore located at $z_s = 0$. The velocity field in this coordinate system is $(u_s, w_s) = (-\partial_{z_s} \psi, \partial_{x_s} \psi)$. In the same way, the wavenumbers can be written as, $\mathbf{k} = (k_{x_s}, k_{z_s})$. The non-normal flow condition at the boundary in this coordinate system, can be written as,

$$w_s |_{z_s=0} = 0, \quad \forall x_s, t. \quad (1.46)$$

Applied to the wavefield, equation (1.46) becomes,

$$k_{x_s}^{inc} \psi^{inc} + k_{x_s}^{refl} \psi^{refl} |_{z_s=0} = 0, \quad \forall x_s, t, \quad (1.47)$$

or,

$$k_{x_s}^{inc} \Psi^{inc} e^{i(\mathbf{k}^{inc} \mathbf{r} - \omega^{inc} t)} + k_{x_s}^{refl} \Psi^{refl} e^{i(\mathbf{k}^{refl} \mathbf{r} - \omega^{refl} t)} |_{z_s=0} = 0, \quad \forall x_s, t, \quad (1.48)$$

which is satisfied if

$$\omega^{refl} = \omega^{inc}, \quad (1.49)$$

$$k_{x_s}^{refl} = k_{x_s}^{inc}, \quad (1.50)$$

$$\Psi^{refl} = \Psi^{inc} = \Psi_0. \quad (1.51)$$

Thus, the frequency and the component of the wavenumber parallel to the boundary are both conserved under reflections. The normal to the boundary wavenumber of the reflected wave can be determined by geometric construction and the dispersion relation.

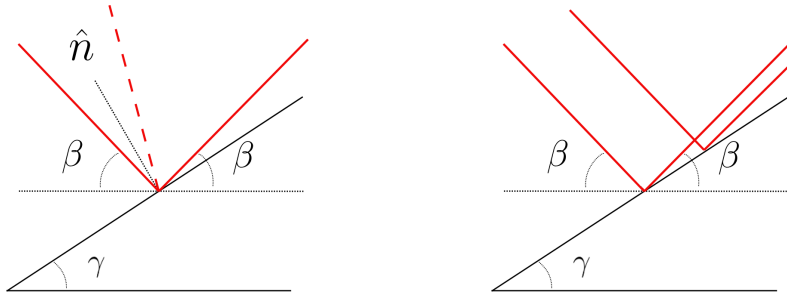


Figure 1.3: Sketch of an internal wave reflection. (a) The wave incoming from the left will be reflected in the direction of the dashed line for an usual wave reflection, and in the direction of the solid line for an internal wave reflection. (b) For an internal wave reflection, a sloped boundary produces focalization of the reflected wave.

Conservation of the frequency and focalization

The conservation of the frequency under reflection implies that $\beta = \sin^{-1}(\omega/N)$, the angle of propagation of the wave, is preserved regardless of the orientation of the boundary. For more familiar specular reflections, as an acoustic or electromagnetic wave reflection, the wavenumber perpendicular to the boundary is conserved. This is not the case for internal waves. This comparison is illustrated in figure 1.3(a). An incident wave coming from the left will reflect following the red dashed line for an acoustic or electromagnetic wave, and will follow the red solid line for an internal wave reflection.

An implication of the conservation of the frequency under reflection is that the sloped boundary focuses or defocuses the wave. Focalization or de-focalization occur depending on the relation between the angle of propagation of the incident wave β and the angle of the slope γ . In this work we will restrict to reflections that produce focalization of the reflected wave (as can be seen in figure 1.3(b)). For a more extensive analysis of internal wave reflections see Gostiaux [35].

For focalization reflections the relation between the magnitude of the wavenumbers is,

$$\frac{|\mathbf{k}^{refl}|}{|\mathbf{k}^{inc}|} = \frac{\sin(\beta + \gamma)}{\sin(\beta - \gamma)}, \quad (1.52)$$

written in terms of the wavelength,

$$\frac{\lambda^{refl}}{\lambda^{inc}} = \frac{\sin(\beta - \gamma)}{\sin(\beta + \gamma)}. \quad (1.53)$$

The focalization of the wave will modify the amplitude of the oscillations. In particular, the shearing amplitude will be given by

$$U^{max} = \frac{2\pi\Psi_0}{\lambda}. \quad (1.54)$$

Therefore, the focalization of the reflected wave implies an amplification of the wave, and as $\beta \rightarrow \gamma$ the amplification increases. To summarize, when a internal wave is focused after a reflection, the reflected wave will have a smaller wavelength and a larger shearing velocity.

Critical reflection

When the angle β approaches the angle γ , the reflected wave focused in a decreasing size section of width λ^{refl} , where all the energy of the incident wave is concentrated, generating large shearing velocities. In addition, the wave propagates increasingly close to the boundary. We expect therefore for $\beta = \gamma$, called critical reflection, the reflected wave to have the following properties,

- A null wavelength.
- An infinite amplitude.
- A null velocity group.

We can anticipate that such short scales would be affected by friction and are likely to be dissipated.

The model for linear reflections is a good representation of internal wave reflection when the angles β and γ are not very close. When $\beta \approx \gamma$ one can observe that there is a singularity for the reflected wavenumber. In chapter 4 it will be shown how this singularity can be healed by considering viscous and non-linear effects.

1.2 Internal waves in the atmosphere and ocean

The atmosphere and ocean are naturally stratified systems. The gradients of density change with height (or depth), seasons and the spatial localization around the globe. The ocean and atmosphere are suitable media for internal waves to propagate.

1.2.1 Stratification of the ocean and the atmosphere

Atmosphere

The atmosphere has been earth's first fluid layer to be studied. The changes in the topography allow to measure the change in the gradients of pressure and temperature in the lower section of the atmosphere. More recently, weather balloons have been widely used to measure these profiles at much higher altitudes, manifesting the layer structure of the atmosphere, as shown in figure 1.4, where the temperature as a function of the vertical location is plotted. The subdivision of these layers is performed following the relative strength of the stratification at different altitudes. Starting from the bottom surface, the first layer is the troposphere which is below the stratosphere. Even higher is located the mesosphere, and finally the thermosphere, which extends to about 600 km altitude. Beyond is the exosphere and space.

In figure 1.4 we can observe that the gradients of temperature will present different behavior at different heights of the atmosphere. In the stratosphere the temperature increases with height, in contrast to the trend in the mesosphere and the troposphere, where the temperature decreases with height. This profile seems to indicate that the atmosphere is not stable.

The study of the stability of the atmosphere, which is a compressible fluid, needs in fact the introduction of lapse rate, which is the measure of the change of temperature with height. The dry adiabatic lapse rate takes into account that if air is lifted upwards, then its temperature will decrease as a result of cooling when it expands in the lower pressure

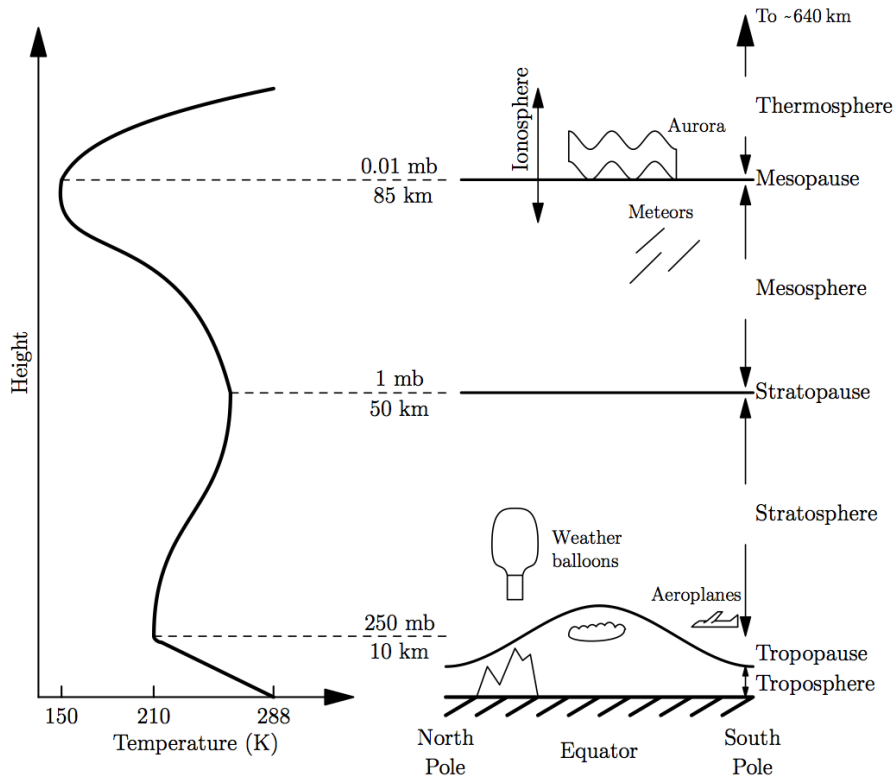


Figure 1.4: Schematic representation of the main layers of the atmosphere, which are determined by the thermal variations with height. Extracted from [67].

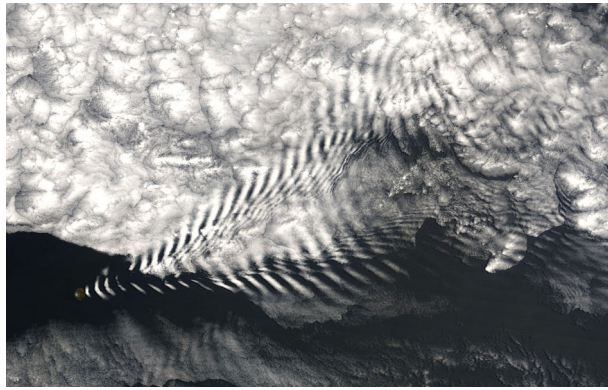


Figure 1.5: Wake of atmospheric internal waves downstream of Amsterdam island, located at southern Indian Ocean.

surroundings at a rate of 10° for each km upwards³. Adjusting the environment lapse rate with the dry adiabatic lapse rate, the profile becomes stable. The environmental mean density profile from which one defines the lapse rate is therefore the relevant magnitude to measure the buoyancy frequency.

At the troposphere, internal waves can be generated by the passage of strong winds over topography. The formation of internal waves downstream from a body is characterized by the Froude number $Fr = U/Nh$, that compares the horizontal kinetic energy of a flow with velocity U to the potential energy necessary to elevate a fluid parcel a height h within

³This is true for air containing no water vapor. The adiabatic lapse rate for moist air is $\sim 6^\circ \cdot \text{km}^{-1}$.

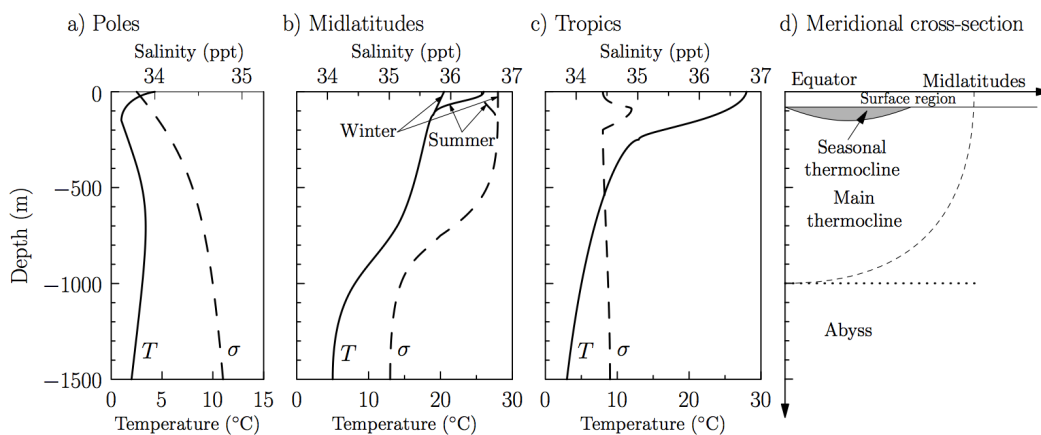


Figure 1.6: Schematic representation of the stratification profile for temperature T (solid line) and salinity σ (dashed line) of the ocean for decreasing latitudes (a), (b) and (c) respectively. The main layers as a function of latitude are indicated in (d). Extracted from [67]

a stratified fluid characterized by buoyancy frequency N . For $Fr > 1$ the kinetic energy is enough to pass over a body of height h and descend back afterward. Therefore, oscillations can occur and internal waves are generated. In the troposphere the buoyancy period is of the order of tens of minutes. Thus, when winds of the order of $40 \text{ km}\cdot\text{h}^{-1}$ pass by mountains of 1 km height, internal waves will be generated.

In some cases it is possible to visualize internal gravity waves in the atmosphere thanks to cloud formation. As the waves generate vertical motion of air, the moisture in the air can condense into water when a strong drop of temperature is generated by upward motion. Therefore, satellite images allow one to visualize internal waves as shown in figure 1.5. These waves can induce mixing in the atmosphere when breaking [28]. It is therefore important for a better prediction of meteorology to model the atmosphere considering internal waves.

Ocean

The internal structure of the ocean has taken longer to be measured because it is much more inaccessible than the atmosphere. Density and temperature measurements identify three main layers in the ocean, as shown in figure 1.6(d). The surface layer, about 100 m deep, is homogenous in both temperature and salinity. This layer undergoes strong mixing generated by contact with the atmosphere through wind and changes in temperature. Below this layer is the pycnocline, a section about 1 km thick with strong stratification where the buoyancy frequency can be of the order of $10^{-2} \text{ rad}\cdot\text{s}^{-1}$. This layer inhibits the vertical motion and acts as a barrier between the surface layer and the abysmal layer. The abysmal layer is the deepest layer, about 4 km thick, and has weak gradients of density.

1.2.2 Generation of internal waves in the ocean

There are mainly two mechanisms that generate internal waves in the ocean, which occur at the bottom seafloor and at the pycnocline region. As with the atmosphere, the displacement of a stratified fluid over topography generates waves at different frequencies depending on the size and shape of the topographies and on the velocity of the flow. These

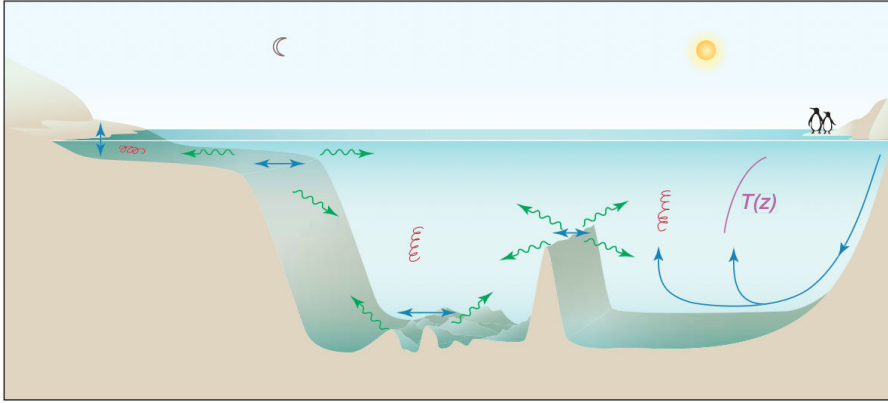


Figure 1.7: Illustration of possible mechanisms that generate internal gravity waves. Extracted from [33]

flows can be due to tides, currents or eddies. The generation of waves in the pycnocline region is due to effects at the surface such as storms that agitate the homogeneous region of the surface's ocean [21]. The different types of wave generation have been summarized by Garrett *et al.* [33] as shown in figure 1.7.

The generation of internal waves due to tidal forcing is a wide spread subject of study. Many advances have been achieved experimentally [24, 36, 42, 76], as well as numerically [54] or *in situ* measurements [25, 26], in order to determine the transfer of energy between tide and internal waves, which is not negligible in estimating the oceanic energy budget [74].

1.2.3 Internal waves near oceanic seafloor

Internal waves are often observed to break close to the seafloor topography that generates them, or from which they scatter. This breaking often generates turbulent structures observed hundreds of meters above the seafloor [44]. In consequence, in the proximities of the seafloor the mean velocities are strongly increased.

It has been observed that in the regions where the continental slope is nearly critical with respect to the semidiurnal tide there is an intensification of near-bottom water velocities and bottom shear stresses [53]. It is suggested that this effect arises from the reflection of remotely generated internal waves. In consequence, the reflection of internal waves can affect sedimentation patterns and bottom gradients. In addition, it is estimated that these shears are high enough to inhibit deposition of fine-grained sediment onto the slopes. Therefore, the angles of energy propagation of semidiurnal internal tides may determine the average gradient of continental slopes in ocean basins (~ 2 to 4 degrees) [12].

The erosion effect of internal gravity waves has been observed by *in situ* measurement. It has been seen that after the passage of internal gravity waves near the seabed, there is an increase of the concentration of particles in suspension, whether in the benthic layer (a 10 m layer on top of the seabed) or in the full water column [5, 11, 40, 59]. It is then pertinent to study the interaction of internal gravity waves over boundaries and the different mechanism for which internal waves can lead to particle erosion.

Internal gravity waves in the laboratory, techniques and implements

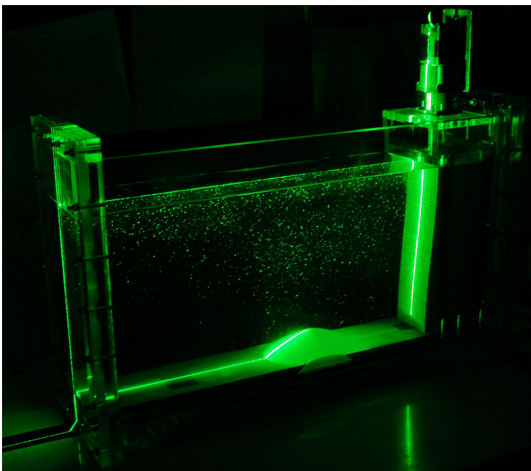


Photo of an experimental setup. A laser sheet illuminating PIV particles seeded in the stratified fluid.

The study of internal gravity waves can be developed through many different approaches, including numerical simulations, ocean and atmosphere measurements in addition to laboratory experiments. All three are necessary for the understanding of internal waves related processes and complement each other. In this work we will develop an experimental approach.

Experiments allow for the control of the main parameters of the generation of internal waves. Establishing a desired density profile plays a fundamental role in the control of internal wave propagation. In addition, the generation of internal waves can be produced by many different setups. In order to obtain a particular type of wave, we use an elaborate mechanism developed at ENS de Lyon.

Given the lack of a well defined interface, the observation of internal waves is not a trivial task when the stratification has a continuous change of density.

In addition to the ability to control physical parameters that can be achieved in experimental setups, experiments are a suitable environment for explorative measurements. This allows one to encounter unexpected phenomena and their further study.

We will detail in this chapter the different experimental stages to perform, observe, and measure internal gravity waves. The experiments performed in this work have been mostly motivated by possible oceanic and atmospheric applications.

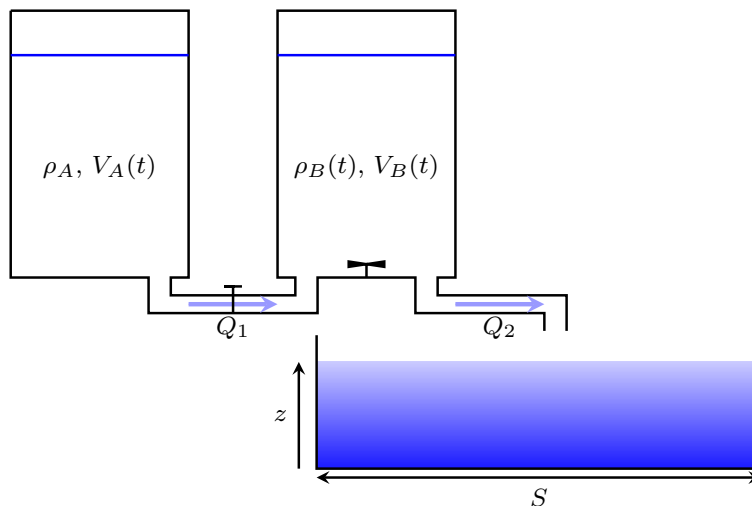


Figure 2.1: Schematics of the double bucket method for the generation of a linear stratified density profile. Extracted from [7].

2.1 Laboratory: experimental techniques

2.1.1 Double bucket method

The generation of a stratified fluid is one of the fundamental steps in the experimental procedure of the experiments performed in this work, given that internal waves propagate exclusively in stratified fluids. Stratification in the fluid can be created through a density or temperature stratification. We performed experiments using density stratification with salt.

We will use salt water with densities ranging between 1000 g.L^{-1} and 1050 g.L^{-1} so that the largest variation of density is less than 5% of the mean density. In consequence, for a 35 cm high tank, we will obtain buoyancy frequencies N of the order of 1 rad.s^{-1} .

We want to generate a stratification that has a constant N for all heights. This can be achieved by generating a linear stratification using the double bucket method [32, 55] illustrated in figure 2.1. A bucket A of fixed density ρ_A is discharged in a bucket B with a flow rate Q_1 . The fluid of density $\rho_B(t)$ in the bucket B , always in agitation, is discharged in the experimental tank with a flow rate Q_2 .

Mass conservation imposed by the flow rates and densities implies

$$\frac{d(\rho_B(t)V_B(t))}{dt} = \rho_A Q_1 - \rho_B(t) Q_2, \quad (2.1)$$

whereas the volume conservation gives

$$\frac{dV_B(t)}{dt} = Q_1 - Q_2, \quad (2.2)$$

from where we derive,

$$V_B(t) = (Q_1 - Q_2)t + V_B(0). \quad (2.3)$$

By combining equations (2.1) and (2.3), we obtain a differential equation for $\rho_B(t)$.

$$\frac{d\rho_B(t)}{dt} = Q_1 \frac{\rho_A - \rho_B(t)}{(Q_1 - Q_2)t + V_B(0)}. \quad (2.4)$$

By solving this differential equation, we extract the evolution of $\rho_B(t)$, that is,

$$\rho_B(t) = \rho_A - (\rho_A - \rho_B(0)) \left(1 + \frac{(Q_1 - Q_2)}{V_B(0)} t \right)^{Q_1/(Q_2 - Q_1)}. \quad (2.5)$$

In addition, the experimental tank can be filled from the bottom or from the top of the free surface. In consequence, a fluid injected at time t will be located at a height,

$$z(t) = \frac{Q_2}{S} t, \quad (2.6)$$

when filled from above, and at a height

$$z(t) = H - \frac{Q_2}{S} t, \quad (2.7)$$

when filled from below, where S is the surface of the base of the experimental tank, and H its height. Combining this results with equation (2.5), we obtain the density in the experimental tank as a function of height,

$$\rho_B(z) = \rho_A - (\rho_A - \rho_B(0)) \left(1 + \frac{(Q_1 - Q_2)}{Q_2} \frac{S}{V_B(0)} z \right)^{Q_1/(Q_2 - Q_1)}, \quad (2.8)$$

when filling from the top, and

$$\rho_B(z) = \rho_A - (\rho_A - \rho_B(0)) \left(1 + \frac{(Q_1 - Q_2)}{Q_2} \frac{S}{V_B(0)} (H - z) \right)^{Q_1/(Q_2 - Q_1)}. \quad (2.9)$$

when filling from below the tank. From the expressions of the density as a function of height we notice that the stratification will be linear only when $Q_1/(Q_2 - Q_1) = 1$, that is, when $Q_1 = Q_2/2$. Two methods allow one to achieve this specific relation between flow rates: the flow rates can be controlled independently by two peristaltic pumps, or can be determined by imposing Q_2 and obtaining Q_1 by communicating both tanks from below. This last method requires equal section of the base of both tanks.

For $Q_1 = Q_2/2$, the density profile will be,

$$\rho_B(z) = \rho_B(0) + (\rho_A - \rho_B(0)) \frac{S}{2V_B(0)} z, \quad (2.10)$$

$$\rho_B(z) = \rho_A + (\rho_A - \rho_B(0)) \frac{S}{2V_B(0)} z, \quad (2.11)$$

for the filling from above and below, respectively.

The densities will be selected depending on whether the filling is performed from above or from below. In order to obtain a stratification that increases its density with depth, we need $\rho_B(0) < \rho_A$ when we fill from below and, $\rho_A < \rho_B(0)$ when we fill from above. The average time to fill a 30 cm deep tank in order to avoid mixing is around 3 h. For the tanks used in this work, this time is roughly independent of the size of the base of the tank.

2.1.2 Density measurements

To ensure that the buoyancy frequency, N , is the same for all height in the experiments, one needs to accurately produce linear stratification profiles. In order to perform a precise measurement of the density profile we use a densimeter ANtonPaar DMA 35. The densimeter consists of a capillary filled with the fluid to be studied. An electro-mechanic

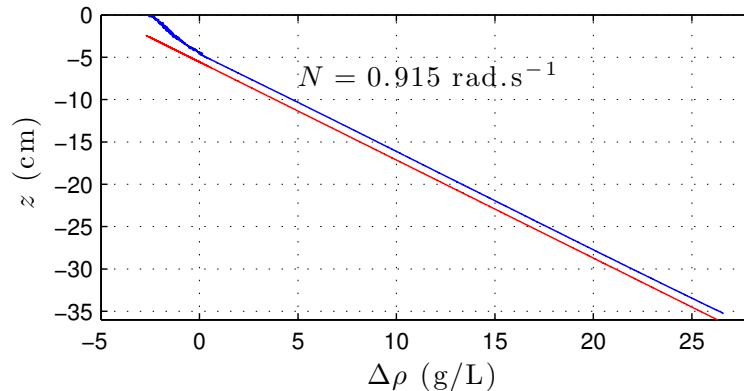


Figure 2.2: Depth as a function of $\Delta\rho = \rho - 1000 \text{ g}\cdot\text{L}^{-1}$. Density profile measured with a conductivity probe in blue and, in red the linear fit displaced 1 cm below. The buoyancy frequency N is computed from the linear fit.

system vibrates the capillary and measures the resonance frequency of the capillary-fluid system. The resonance frequency depends on the mass of both, the known capillary mass and the fluid mass. From where the fluid mass can be extracted. This equipment allows one to measure densities between 0 and $3 \text{ kg}\cdot\text{L}^{-1}$ with a precision of $0.001 \text{ kg}\cdot\text{L}^{-1}$.

This technique allows one to obtain a precise measurement of the density. Nevertheless, in order to measure the stratification we would need to extract fluid from the selected depths before measuring the density. This procedure is complicated, and limits the spatial resolution of the measurement. Therefore, the measurement of stratification is also performed with a conductivity probe that measures the electric resistivity of the fluid between two conductive plates. The resistivity of the fluid depends on the ions present in the solution, and a calibration allows the association of the resistivity value with the density.

The probe attached to a stainless steel bar is moved in the stratified fluid by a stepper motor. The resistivity is measured continuously as the probe descends. The probe descends slowly in order to generate the least possible change in the stratification. An example of the measure of the density is shown in figure 2.2. The buoyancy frequency is obtained by modeling this measurements with a linear fit. When multiplying the linear fit by $-\rho_0/g$ we obtain N^2 . We can observe at the top of the profile that the fluid is less stratify than for the rest of the column. One of the effects responsible for this homogenization is the movement of the air in the free surface. Other effects, such as filling effects and large temperatures change can also influence the density profile, especially at the top and the bottom of the stratification.

2.1.3 Generation of internal waves

Historically, to produce waves propagating in the stratified fluid, a cylinder was oscillated in the fluid. The oscillations of the cylinder imposes the motion to the surrounding fluid and generates internal gravity waves. This experimental device generates four wave beams, and allowed one to perform the first experimental measurements of internal waves [34, 52].

In this work, two types of wave generator were used. Both are based on generating an oscillating boundary along the width of the tank. In one, the conditions of the moving boundary are imposed when built. The other allows the reconfiguration of the boundary at any moment. We will describe both methods.

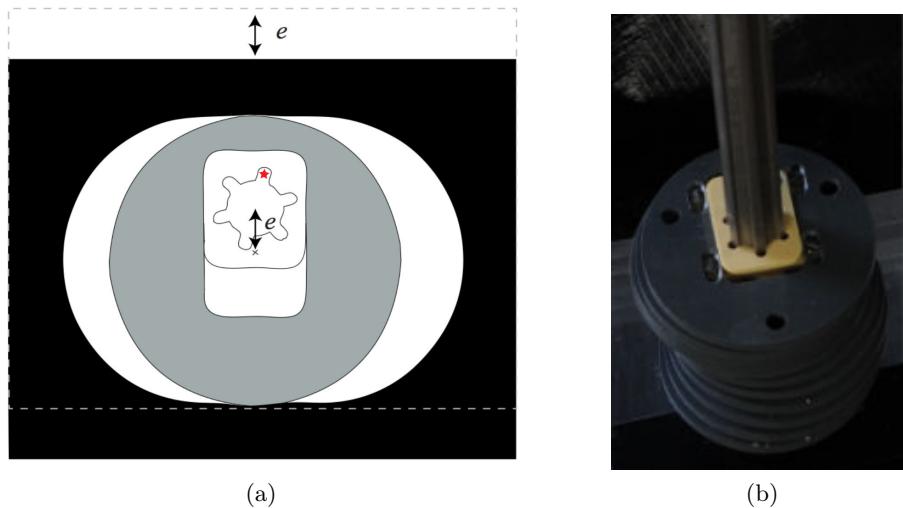


Figure 2.3: (a) Representation of the disc and plate system which transforms the rotation motion into a unidirectional translation. The white piece within the disc can be displaced to change the eccentricity e , and therefore, the translation amplitude of the black plate. (b) Image of discs piled over the camshaft (the discs are continuously shifted in phase). Extracted from [6, 7].

Camshaft based wave generator

We have principally used a wave generator developed at ENS de Lyon by Gostiaux *et al.* [38], characterized by Mercier *et al.* [48] and improved by Bordes [6], which allows the generation of only one wave beam with a selected amplitude, wavelength and frequency. The working principle of this generator is to transform a rotation of a vertical camshaft of plates in an oscillatory horizontal movement. The rotation of the camshaft is generated by a motor, and perforated discs within the plates allow the selection of the amplitude and phase of oscillation.

In figure 2.3(a) is shown a disc (in grey) with the axle positioned inside. The position of the white piece of the inside can be regulated in a way that the axle does not necessarily coincide with the center of the disc. When rotated, the black plate allows one to obtain an unidirectional oscillation, where the amplitude corresponds to the distance between the axle and the center of the disc. The system allows the generation of horizontal displacements of amplitude e , between 0 and 1.5 cm. This setup also has the possibility of changing the relative phase between two contiguous discs. For a fixed e , each plate will perform the same displacement but shifted in temporal phase. The camshaft has 6 slots distributed at 60° . This allows the generation of a whole wavelength using 6 discs, by shifting in one the slot when introduced in the axle. For generating a smaller phase shift (or longer wavelength), the workshop of Mécanique du Laboratoire de Physique de l'ENS Lyon, made several sets of discs which allow one to performed a wider range of phase shifts. The three type of discs are shown in figure 2.4. The difference between these discs is that the position of the grooves in the axle are shifted respect to the displacement direction of the plates. This shift is 0° , 15° , -15° and 30° for the discs A, B, B' and C respectively. By combining these 3 types of discs we can perform shifts up to 15° .

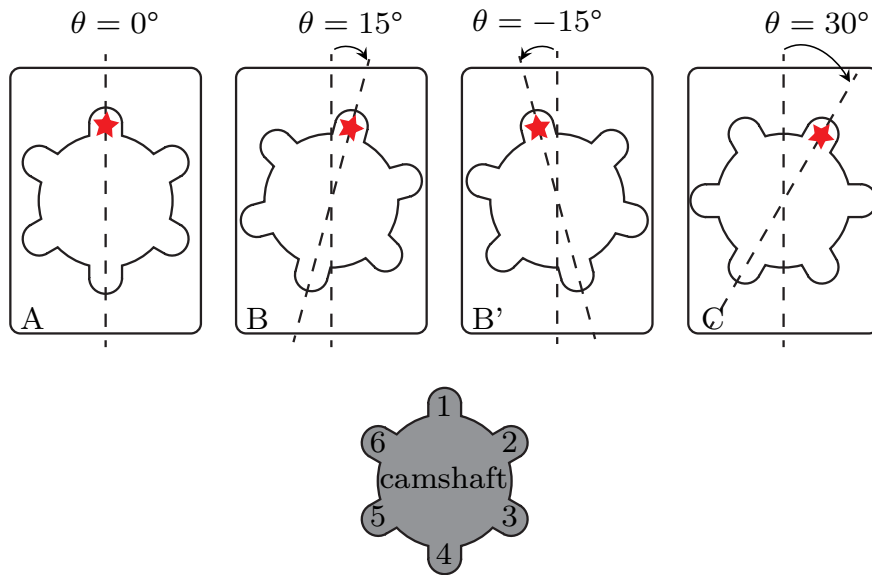


Figure 2.4: Representation of the three sets of discs. θ is the angle between the displacement direction and the closest groove. B' is obtained by rotating B. Below, the camshaft and the grooves are numerated. Extracted from [7].

GOAL

The generator GOAL (Generator of Oscillation As you Like) is an internal wave generator developed through a collaborative work at the Laboratory of the ENS de Lyon between the Internal Wave group and the Electronic and Mechanic workshop¹. The main objective was to construct a generator which allowed one to produce a given boundary profile that evolves in time.

The Goal generator is based on the same principle as the camshaft generator in the sense that the boundary profile is produced by vertically spaced plates moving unidimensionally, as illustrated in figure 2.5. However the GOAL generator allows to control independently each plate. In addition, the settings of the plate motion are controlled electronically and can be modified at any moment.

The wave generator can be divided in two main parts: the section consisting of 50 plates of 6.5 mm thick that is immersed in the tank filled with the stratified fluid, and the part which controls the oscillation of the plates, consisting on 50 linear stepper motors controlled by an automata and controlled through a LabView interface.

The horizontal motion of each plate x_i , where $i \in [1, 50]$, will be given by the temporal function, $x_i = X_i(t)$, where $X_i(t)$ can be any classic periodic function (sinusoidal, triangle or square function). In particular, we used sinusoidal functions in this work for which the amplitude, phase, and frequency of the signal are adjusted.

In this work the GOAL generator has not been fully exploited given that it has been used for the generation of plane waves only. It has been used mainly because of its facility in modifying experimental parameters during the experiment.

¹For further details of the GOAL generator contact Pascal Metz: pascal.metz@ens-lyon.fr.

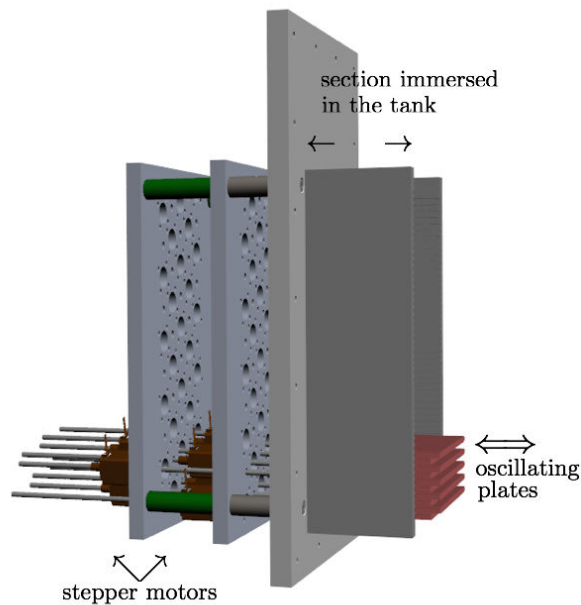


Figure 2.5: Schematics of the GOAL wave generator. The moving boundary is composed of 50 vertically spaced plates which are controlled independently. Each plate is driven by a linear stepper motor which can be command through a LabView interface.

Wave generator profile

As previously detailed, the camshaft wave generator allows the adjustment of the phase and amplitude of each plate, and, during the experiment, the frequency of oscillation of the set of plates can be varied. The GOAL generator, allows one to change the phase, amplitude, and frequency independently for each plate during the experiment. This allows a broad range of possible oscillating boundaries. In addition, the camshaft wave generator can be positioned vertically or horizontally within the tank. In this work, we will always place the generator vertically. Two types of boundary profile have been used: a boundary profile that generates plane waves and a vertical mode.

To generate,

- Plane waves

The horizontal velocity at $x = 0$ generated by this profile can be expressed as,

$$u = \Psi_0 k_z \sin(\omega t - k_z z), \quad (2.12)$$

where the horizontal velocity of each plate will have amplitude $\Psi_0 k_z$, and the velocity of each plate will be shifted as a function of the position z . The set of discs available allows one to generate wavelengths $\lambda^g = 2\pi/k_z$ between 3 and 24 times the thickness of the plates.

- Vertical mode

The horizontal velocity at $x = 0$ generated by the vertical mode profile is,

$$u = u_0 \sin\left(\frac{\pi}{H} z\right) \cos(\omega t), \quad (2.13)$$

where H is the height of the fluid, and $k_z = \pi/H$. The horizontal velocity is a sinusoidal function of time, where the amplitude changes with height. This profile is generated by discs with the same phase, whose eccentricity changes with height in order to generate a sinusoidal profile.

In both types of profiles, the magnitude of the velocity is imposed by the rate of rotation. We will use wavelengths not smaller than 6 discs in order to avoid rough discretization of the shape of the wave. The largest wave generator used 50 vertically spaced plates where each plate is 0.65 cm thick.

2.1.4 Visualization techniques

The observation of internal gravity waves is not a trivial task. Unlike surface gravity waves and perturbations in a bilayer system, internal waves propagate in the inside of a continuously stratified fluid. Specific techniques have been developed in order to observe these perturbations. In this work we have used PIV and Schlieren visualization techniques which we detail.

Synthetic Schlieren

The Synthetic Schlieren technique exploits the fact that the concentration of salt in water modifies the refractive index of the solution, in order to detect the densities perturbations [16, 68]. A ray of light passing through a medium with inhomogeneous refractive index will be spatially bent. When the refractive index only varies in one direction (z in our case), it is possible to compute the gradient of the refractive index by measuring the bending angle.

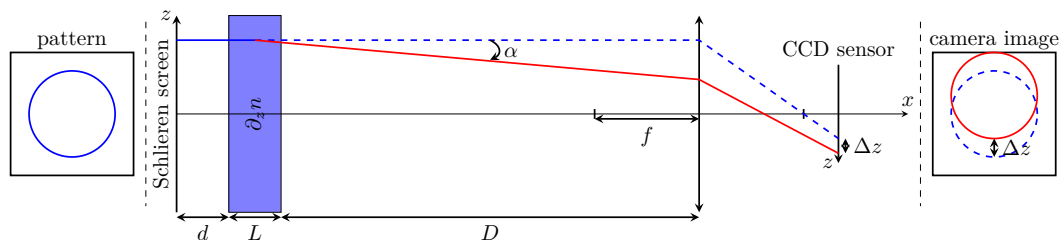


Figure 2.6: Schematics of the Schlieren visualization setup. The rays of light generated from luminous screen traverse a pattern (a circle in this example). The camera of focal length f and CCD sensor, is focused on the Schlieren screen. The stratified fluid between the screen and the camera shifts the position of the circle at the CCD sensor in Δz . Extracted from [7].

A camera with focal length f measures in time a pattern placed over a luminous screen (Schlieren screen) with a CCD sensor. Between the screen and the camera is located a tank filled with a fluid that is stratified in density and, therefore, in the refractive index, which bends the light rays in an angle α , as shown in figure 2.6. This angle is related to the spatial gradient of the refractive index through the relation,

$$\alpha = \frac{L}{n} \frac{dn}{dz} = \frac{L}{n} \frac{dn}{d\rho} \frac{d\rho}{dz}. \quad (2.14)$$

In the salt concentration range of salt used in this work, the variation of the density as a function of the refractive index is linear and the slope is, $d\rho/dn = 4.1 \text{ g}\cdot\text{cm}^{-3}$.

The deviation of the ray of light will generate a displacement of the pattern over the CCD sensor. For the approximation of small angles the deviation of the pattern with respect to the homogenous medium case is,

$$\Delta z = \alpha f \frac{d + L/2}{d + L + D - f}. \quad (2.15)$$

We can translate the spatial displacement of the detected pattern to pixel displacement through the relation $\Delta p = \Delta z/r$, where r is the physical size of a pixel.

The density gradient can be therefore written as,

$$\frac{\partial \rho}{\partial z} = r \Delta p \frac{d\rho}{dn} \frac{n}{L} \frac{(d + L + D - f)}{f(d + L/2)}. \quad (2.16)$$

When internal waves propagate, the density gradient is locally modified. In consequence, the refractive index is locally modified and therefore so will it be the pattern on the camera. The comparison of an image of the fluid with and without waves allows one to determine the local variations of the refractive index caused by the internal waves. Considering that at $t = 0$ no waves are present in the fluid, the perturbations of the refractive index will be,

$$\frac{\partial \tilde{\rho}}{\partial x} = \frac{\partial \rho(t)}{\partial x} - \frac{\partial \rho(0)}{\partial x} \quad \text{and} \quad \frac{\partial \tilde{\rho}}{\partial z} = \frac{\partial \rho(t)}{\partial z} - \frac{\partial \rho(0)}{\partial z}. \quad (2.17)$$

From where we can obtain the evolution in time of the perturbations of the gradient of density, by comparing the perturbed density profile at t with the unperturbed at $t = 0$. This specific procedure will be explained in detailed below.

If vertical mixing occurs, so that the average density profile is changed, then the measure of the wave will be distorted, as the mixing and the wave perturbation will both contribute in the term $\partial \rho(t)/\partial z$. In order to have reliable measurements, mixing and long experiments should be avoided. It is important to mention that this technique is developed for flows with specific features, usually two-dimensional and linear flows, with some exceptions as can be seen in [60], for example.

Particle image velocimetry (PIV)

Particle image velocimetry is a technique that allows one to measure the velocity field of a flow [70]. This is performed by seeding the fluid with particles that can be observed when illuminated. The particles will be dragged by the flow, and their motion will represent the flow. The selection of the particles is such that the particles are advected by the flow, having very little inertia.

In our experiments, the particles are slightly heavier than the surrounding fluid ($\rho_p = 1.1 \text{ g}\cdot\text{cm}^{-3}$) and of a typical size of $10 \mu\text{m}$. For the flow velocities measured in the experiments, the Stokes number is $\text{St} \approx 10^{-5}$. The Stokes number, $\text{St} = \tau_p/\tau_f$ measures the ratio between the characteristic time of the particle, τ_p , and the characteristic time of the flow, τ_f . It is also an indicator of the flow tracer fidelity. For acceptable tracing accuracy, the particle response time should be faster than the smallest time scale of the flow. For $\text{St} < 0.1$ the tracing accuracy errors are below 1% [70].

The fluid is illuminated with a vertical laser sheet and the position of the particles is measured by a camera at different times. Two successive images are compared in order to obtain the displacement of the particles, and estimate their velocity and therefore the fluids velocity.

Image correlation algorithm

To measure the evolution of a magnitude as a function of time, either the velocity or the perturbed density gradient, we compare two successive images through a PIV algorithm visualized in the *uvmat* graphic interface [66]. Each image is divided in boxes of a selected size. The size of the box is such that a recognizable pattern can be observe within the box, but small enough to present little perturbation of the shape of the pattern between two successive images. The pattern is generated with seeded particles for PIV and with the pattern on the screen for Synthetic Schlieren. The algorithm determines the position of the pattern in the successive image by calculating the correlation coefficients [30], the maximal correlation defines the position of the pattern in the successive image. This algorithm allows to estimate the displacement of the pattern in a time Δt defined by the acquisition frequency. That is, the change of the position of the particles in time for the PIV technique and distortion effects from density changes for the Synthetic Schlieren technique.

2.2 Image processing techniques

The visualization techniques presented in section 2.1.4, allows one to determine the spatial distribution of the velocity or density gradient field as a function of time, which we call $\mathbf{f}(x, z, t)$. We will introduce some post processing techniques performed over $\mathbf{f}(x, z, t)$ that will be used to produce many results presented in this work.

2.2.1 Temporal filtering

The temporal filtering technique allows one to extract the spatial contribution of \mathbf{f} related to a specific frequency ω . This allows one to focus on the spatial contribution of each specific frequency. The temporal filtering technique is performed independently over each component of the field; let us consider, for example, the horizontal component of the field $f_x(x, z, t)$. This field can be expressed as,

$$f_x(x, z, t) = \frac{1}{N_0} \sum_{n=1}^{N_0} \hat{f}_x(x, z, \omega_n) e^{i2\pi\omega_n/N_0}, \quad (2.18)$$

$$= \frac{1}{N_0} \sum_{n=1}^{N_0} f_x^{\omega_n}(x, z, t), \quad (2.19)$$

where N_0 (the number of partitions) and the frequency resolution, $\Delta\omega = \omega_{n+1} - \omega_n$, will be given by the temporal size and resolution of the field. The spatial field associated to the frequency ω_n is,

$$f_x^{\omega_n}(x, z, t) = \hat{f}_x(x, z, \omega_n) e^{i2\pi\omega_n/N_0}. \quad (2.20)$$

The spatial field $f_x(x, z, t)$ is the addition of the contributions of the spatial fields associated to each frequency ω_n .

In practice, we will be interested in the contribution of the field associated with a frequency interval and not with an individual frequency. We will analyze the field associated with the frequencies $\omega \in [\omega_-, \omega_+]$, where ω_- and ω_+ are the limits of the frequency interval we are interested in.

In order to extract the temporal frequency content of the field, a Fast Fourier Transform (FFT) is performed for the time evolution field signal related to each spatial point. This process is performed over a selected spatial region, small enough to have similar spectral

characteristics in the region. The resulting spectrum is averaged for all the points within the region to increase the signal-to-noise ratio. Then, a frequency filter is performed over the spectrum. The resulting spectrum \hat{g} , can be written,

$$\hat{g}(x, z, \omega) = \hat{f}_x(x, z, \omega) \cdot H(\omega), \quad (2.21)$$

where, $H(\omega)$ is a rectangular function smoothed at the sides by a cosine function so that the amplitude of H is 1 for $\omega \in [\omega_-, \omega_+]$ and zero elsewhere. Finally, the field associated with the frequencies $\omega \in [\omega_-, \omega_+]$, $f_x^\omega(x, z, t)$, is determined by applying the inverse FFT to $\hat{g}(x, z, \omega)$.

2.2.2 Hilbert transform

The Hilbert transform is a filtering technique which allows the extraction of the spatial contribution of $\mathbf{f}(x, z, t)$ related to a specific wavenumber (k_x, k_z) . This spatial filtering is analogous to the temporal filtering presented previously. The application of this method to internal gravity waves has been developed by Mercier *et al* [46, 47].

The utility of the Hilbert transform is manifested in the fact that an internal plane wave propagating in a linearly stratified fluid cannot be fully identified by only the temporal frequency ω and the absolute value of the wavenumber $|\mathbf{k}|$. It is necessary to explicitly defined the sign and value of the components of the wavenumber. In figure 2.7 the four possible waves that exist for a pair of values $(\omega, |\mathbf{k}|)$ are shown. To extract one of the four waves we apply the Hilbert transform.

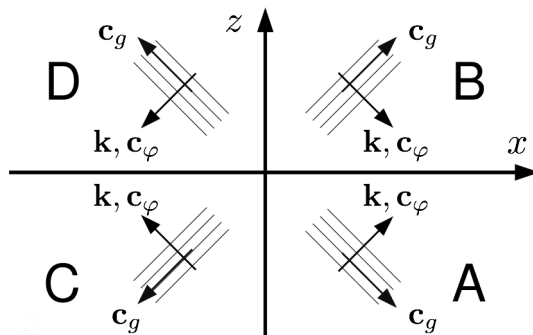


Figure 2.7: Illustration representing four possible waves generated from one pair of values $(\omega, |\mathbf{k}|)$, A, B, C and D.

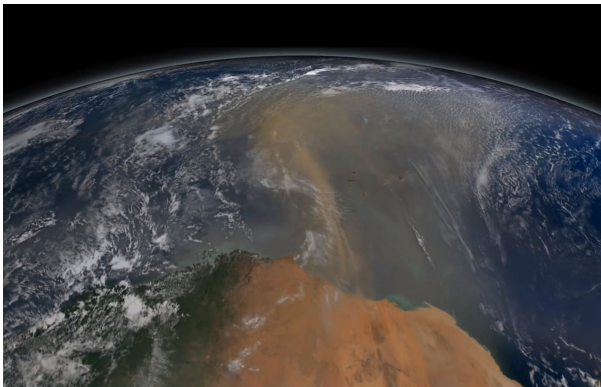
The procedure to extract from the full field \mathbf{f} the field associated to a specific wavenumber (or interval of wavenumber) is performed in the same way as for the temporal filtering. But rather than performing the FFT over time, the spectrum is performed over the space coordinate, x or z , and the spectrum is filtered around k_x or k_z , respectively. The Hilbert transform together with the temporal filtering allows one to identify a wave through the triple (ω, k_x, k_z) within a complex field.

2.3 Perspectives

We have presented procedures with which internal gravity waves are generated in a well controlled environment. In addition, visualization techniques allow one to observe the resulting wave field. After the acquisition is performed, we can apply additional processing to the wave field to isolate the particular process we are interested in.

In the following chapters we will use internal gravity waves under a large variety of situations, that will require the good handling of the experimental techniques detailed in this chapter.

Sediment transport



Satellite view of sand particles driven from Sahara desert towards Amazons. Photo Credit: NASA.

The oceans and the atmosphere are dynamical systems globally connected through large scale processes, as for example, the Thermohaline current and Rossby waves, which are usually composed of multi-scales behavior (eddies, costal currents, internal waves). Among other things, these processes have an effect on the accumulation, dispersion and transport of mineral and organic particles present in these systems.

Biological life processes, fish resources, pollutants and volcanic ash dispersal, and sand formation depend, among other things, on the transport of sediments and nutrients in the ocean

and the atmosphere.

Resuspension of sediments can be caused by many phenomena in the ocean (surface waves, density currents, etc.). A common feature in all these processes is the generation of a shear stress intense enough to induce particle motion therefore generating erosion at the seafloor boundary.

Since internal waves are created in great part owing to tidal forcing and oceanic topography jointly, internal waves are candidates to be a considerable source of sediment resuspension and transport.

3.1 Introduction

The physical processes involved in sediment transport are complex and influenced by many hydrodynamical (or aeolian) and sedimentological factors over a wide range of spatial and temporal scales. In the ocean, internal wave forcing plays a significant role in the transport of sediments, from coastal zones [71] to deep-water environments [23].

Despite the ubiquity of granular systems in nature and industry, the physics of granular media is yet not well understood. Grains behavior exhibits a great variety of characteristics with unique properties, and at the moment no theoretical framework allows to explain the wide range of possibilities that these systems display.

Sediment grain size in ocean basin environments typically range from non-cohesive sand to cohesive clay. We therefore need a basic understanding of the fundamental physics of erosion and sediment transport.

The results of laboratory experiments and discrete numerical simulations have enlarged the understanding of granular media, and the present description of sediment transport is based largely on empirical results obtained by field and laboratory measurements.

Motivation: state of the art and background

Sedimentation in the ocean is controlled by a large variety of interacting factors such as surface waves, tides and internal waves, sea level changes, sediment supply, as well as climatic and geological long term dynamics. In particular, density gradients due to changes in salinity, temperature or particulate matter are found everywhere in the ocean, generating a medium where internal gravity waves can propagate. Internal tides (internal waves with diurnal and semi-diurnal periods) are believed to be a mechanism that provides energy to deep marine areas, that otherwise might not receive much energy flux [27]. Since the primary source of internal waves generation is the interaction of surface tides and seafloor topography, internal waves create shear stresses in marine boundaries when they are created and also when they are reflected over other seafloor boundaries after being radiated out from the source.

Many observational studies have been done that indicate that internal gravity waves are a cause of sediment resuspension. Usually, measurements of the propagating perturbation and sediment resuspension are done in an independent way. Bogucki *et al.* [5] reported the observation, thanks to temperature measurements, of internal solitary waves propagating upstream along a strongly stratified bottom layer on the California shelf, which was accompanied by an increased concentration of particles in the water column (increase in water turbidity). In the western Portuguese mid-shelf, Quaresma *et al.* [59] complemented these observations by a CTD survey (conductivity, temperature, and depth measurements) and bottom sediment sampling, in order to observe the propagation of large amplitude internal solitons forcing strong bottom current pulses. In agreement with these results, Hosegood & van Haren [40] observed an $O(10^2)$ larger than the background value increase in sediment fluxes at 2 and 30 m above the bed after the passage of a solibore (which they named because it displays the properties of both turbulent internal bores and nonlinear internal solitary waves). In the Massachusetts Bay, by measuring the bottom velocity increase (1 m from bottom), Butman *et al.* [11] estimated that the resuspension time associated to large-amplitude internal waves, is about the same order of magnitude as resuspension time caused by surface waves.

In every case the capacity of generating sediment transport through the interaction of internal waves over the seafloor is limited by the shear stress generated at the boundary and the physical characteristics of the particles.

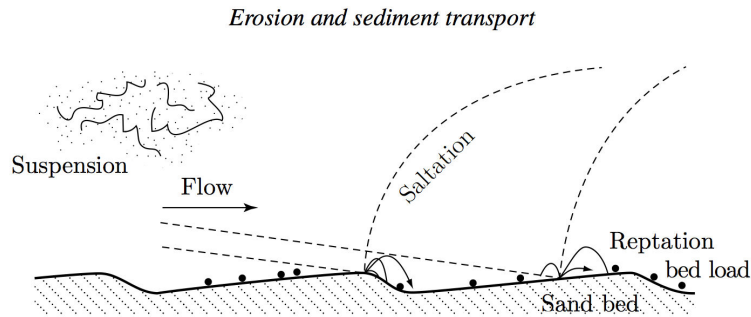


Figure 3.1: A schematic diagram showing the different modes and trajectories of sediment transport. Extracted from [1].

3.2 Physics of erosion, transport and sedimentation of particles in a fluid

When a fluid flows over a stationary solid surface, a boundary layer develops. In this boundary layer the fluid velocity tangential to the boundary goes from the mean value in the interior to zero at the boundary, where viscosity is dominant. If we consider that the boundary is actually formed by sediment particles, then, if this flow is sufficiently intense, an erosion of the boundary is expected.

3.2.1 Sediment transport

In this section we will introduce the basics of erosion and transport of granular material in a fluid through a classical approach in which different types of transport modes are described. This characterization of granular transport is based on the description of Andreotti, Forterre & Pouliquen [1].

The dynamics of granular movement in a fluid can be expressed through three forces acting over the particle: hydrodynamical forces, the force of gravity and contact forces between particles. The relative effect that each of these forces have over the grains will change the qualitative behavior and dynamics of these particles. Depending on the dominating forces involved in the transport of sediment, different modes are distinguished (see figure 3.1). The *suspension* mode will develop if the hydrodynamic forces dominate. This will be expected for fine and/or light sediments and strong fluxes. If the gravity effect over the particles is large enough so that the transport occurs in a thin layer near the boundary, then the transport mode is called *bed load*. The typical bed load transport is composed by large and heavy grains. Within the bed load transport one can make different distinctions in the type of particles trajectories. When the gravity and hydrodynamic forces are dominant, the grains will make successive jumps. In this case, the transport is by *saltation*. When the grains that are driven by the fluid roll at the surface of the particles bed, spending long time intervals of contact between particles, the trajectory is named *traction*. In this case, the three forces are present in the dynamics of the grain. Finally *reptation* is a mode of transport dominated by contact forces and gravity. This trajectory occurs when the grains transported in saltation collide with the bed with enough energy to induce a motion of the lying particles. The idea of mode and trajectory decomposition of granular transport is expressed in the schematic network diagram of figure 3.2.

In this chapter, we will focus on the incipient movement of settled particles in a boundary. We will start by presenting a formalism to relate the sediment flux (or the initiation

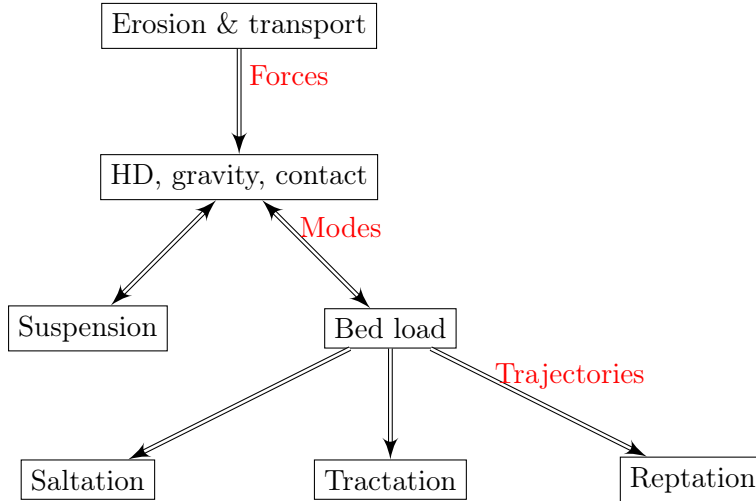


Figure 3.2: Diagram of the different types of granular transport separated by modes and trajectories, which respond to a particular combination of the relative hydrodynamic, gravity and contact forces acting over an individual grain.

of grains movement) to the fluid flow in the bed load transport mode.

3.2.2 Shields dimensionless number

In order to predict the initiation of sediment motion in a horizontal bed composed of particles, the use of the Shields dimensionless number is widely accepted. This number measures the ratio between the apparent weight of the particle in the fluid and the drag exerted by the fluid on the particle. The particle will lose equilibrium and will start moving when these forces balance.

To describe the existence of a transport threshold in the Shields number, we will consider the configuration presented in figure 3.3. The grains are located in a horizontal bed, above which a fluid flows in the horizontal direction with a velocity profile which is zero in the bed and increases away from the bottom. The transition of the velocity field in the region between the surface of the bed and the height where the velocity is null, is very complex, since the exact position where the velocity is null is very difficult to determine, and the non-slip condition will depend on the motion of the particles. For our purposes, it will be satisfactory to approximate that the velocity field is null at the surface of the bed, although we will consider that the particles at the surface will perceive a difference of velocity of the fluid within their size. The boundary condition of the velocity field at the bottom will then be: the fluid does not traverse the boundary (no normal flux $\mathbf{u} \cdot \hat{\mathbf{n}}|_{\text{boundary}} = 0$), and because of viscosity, a layer in the boundary is formed so that the tangent velocity is zero at the boundary (no-slip condition). The exact shape of the velocity profile in the fluid bulk will depend if we are in a turbulent or laminar regime.

The motion of a particle at the surface of the bed will depend on the balance between two horizontal forces: the drag force exerted by the upper flow F_{drag} and the frictional force F_{friction} produced by the contact with other particles. These forces are in opposite direction by definition. The drag force is related to the hydrodynamics of the fluid. This force is proportional to the shear stress at the boundary σ , times the surface of the particle, that is, $F_{\text{drag}} \propto \sigma d^2$. The friction force, F_{friction} will be related to the normal force (in this case, equal in magnitude to the gravity force F_g) through an effective friction coefficient

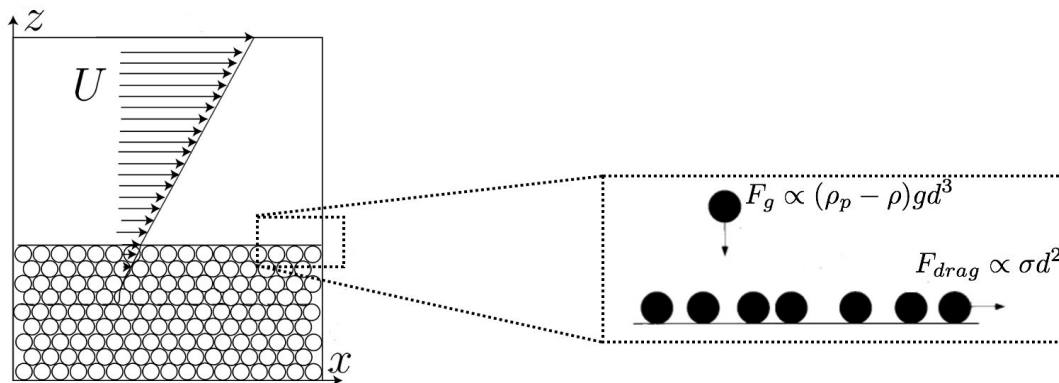


Figure 3.3: Schematics showing the forces acting over an individual grain located in a bed underneath an horizontal stationary flow.

term c_{cont} to model the contact forces between particles [1]. The weight/buoyancy balance that the immersed particle experience, F_g in the vertical direction \hat{z} , will be related to the density and size of the particle and the density of the displaced fluid, this is, $F_g = \rho gV - \rho_p gV = -(\rho_p - \rho)d^3 g\pi/6$, where ρ and ρ_p are respectively the densities of the fluid and of the particle, V and d are the volume and diameter of the particle (which we will consider spherical for simplicity), and g is the acceleration of gravity.

In order to initiate motion of a grain, it is necessary that the force imposed by the fluid overcomes the frictional force imposed by the contact with the boundary, that is, $F_{drag} > F_{friction}$. The Shields dimensionless number is defined as the ratio between these two forces acting over a grain,

$$\Theta = \frac{\sigma}{(\rho_p - \rho)gd} \propto \frac{F_{drag}}{F_{friction}}. \quad (3.1)$$

It characterizes the relative effect of these two forces, and therefore the initiation of transport through a threshold value¹.

The threshold that defines the initiation of grains transport will be given by the balance between the drag force exerted on the upper half of the particle and the gravity force $F_{drag} \gtrsim c_{cont}F_g$, that is,

$$\frac{3\pi d^2 \sigma}{4} \gtrsim \frac{\pi}{6} c_{cont} (\rho_p - \rho) g d^3. \quad (3.2)$$

Writing this balance as a function of the Shields number (equation (3.1)), we obtain a threshold value,

$$\Theta_{th} = \frac{2}{9} c_{cont}, \quad (3.3)$$

this value will vary between 0.09 and 0.14 for a range of particles roughness going from smooth glass to angular grains.

Viscous regime

In this work we will focus on flows in which viscous effects are dominant in the boundary. For these regimes, the viscous shear stress can be expressed as $\sigma = \mu \partial u / \partial z$, where μ is the dynamic viscosity and u the component of the velocity parallel to the granular bed.

¹In equation (3.1) the cohesion between particles has not been considered

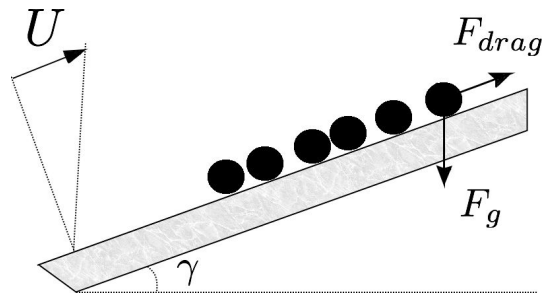


Figure 3.4: Schematics showing the forces acting over a individual grain located in a bed over an inclined slope underneath an horizontal stationary flow.

We will consider that the velocity profile is linear near the boundary, which is a good approximation for viscous flows (for our experiments $Re \approx 100$).

The threshold for an inclined slope

In the case where the bed of grains lies on an inclined slope, as shown in figure 3.4, the threshold value of equation (3.3) obtained for the Shields number will vary as a function of the angle γ between the slope and the horizontal [1]. This can be understood by considering the limit case where the angle γ is near the value where the bed will not be stable, known as the avalanche angle ($\sim 30^\circ$). For this case, with a small perturbation the grains will loose balance more easily than when the particles are lying on a horizontal bed.

For a particle in a bed on a tilted slope the balance of forces can be rewritten. The normal force will be $\frac{\pi}{6}d^3(\rho_p - \rho)g \cos \gamma$ and the tangential force $F_{drag} - \frac{\pi}{6}d^3(\rho_p - \rho)g \sin \gamma$. Through the balance of forces we obtain the transport threshold, that is

$$F_{drag} - \frac{\pi}{6}d^3(\rho_p - \rho)g \sin \gamma = \frac{\pi}{6}d^3(\rho_p - \rho)g \cos \gamma. \quad (3.4)$$

So that the Shields threshold value is modified following,

$$\Theta_{th}(\gamma) = \Theta_{th}(0) \left(\cos \gamma + \frac{\sin \gamma}{c_{cont}} \right), \quad (3.5)$$

this result implies a change of the order of 40% in the Shields threshold value for inclinations of $\gamma = 20^\circ$.

3.2.3 Particles sedimentation

Placing the particles at the bottom of the tank is a non-trivial aspect of the experimental setup. In order to explain the details of the experimental setup we will introduced some concepts of sedimentation in stratified fluids. First we will consider the case of an individual particle in sedimentation in a linearly stratified fluid. Then we will describe sedimentation for a cloud with a large number of settling particles.

Individual grain settling

The classical form to describe a settling sphere of radius $a = d/2$, in a homogenous fluid is through the drag force F_{drag} , which can be written as [75],

$$F_{drag} = 6\pi\mu a w_s + \frac{4}{3}\pi a^3 \frac{\rho}{2} \frac{dw_s}{dt} + 6a^2 \sqrt{\pi\rho\mu} \int_{-\infty}^t \left(\frac{dw_s}{dt} \right)_{t=s} \frac{ds}{\sqrt{t-s}}, \quad (3.6)$$

where ρ is the density of the fluid, w_s the settling velocity and μ the dynamic viscosity. The first term on the right corresponds to the Stokes drag for steady settling velocity w_s . The second and third term are related to the acceleration of the sphere. The second is the added mass term, which is associated to the fact that an accelerating sphere accelerates the surrounding fluid and therefore spends energy. The third term is the Basset history drag, and is due to diffusion of vorticity from an accelerating sphere as the boundary layer forms. The last two terms are negligible for steady conditions. In this case, F_{drag} is usually written using the following expression

$$F_{drag} = C_{drag}^H \frac{1}{2} \rho w_s \pi a^2. \quad (3.7)$$

This formalism can also be used for a settling sphere in a stratified fluid [75]. Considering that the settling velocity is steady, the drag force in a stratified fluid will be $F_{drag} = C_{drag}^S \frac{1}{2} \rho w_s \pi a^2$, where the influence of the stratification is introduced through the unknown coefficient C_{drag}^S . For the range of values explored in this work, it is a good approximation to consider that the settling is steady, of course this will stop being valid for positions where the density of the fluid $\rho(z)$ is close to the density of the particle ρ_p . The force balance in a stratified fluid is:

$$C_{drag}^S \frac{1}{2} \rho w_s \pi a^2 = \frac{4}{3} \pi a^3 (\rho_p - \rho(z)) g. \quad (3.8)$$

From equation (3.8) we can obtain the drag coefficient

$$C_{drag}^S = \frac{8ga}{3w_s^2} \frac{(\rho_p - \rho(z))}{\rho(z)}. \quad (3.9)$$

Defining $\hat{C}_{drag}^S = C_{drag}^S / C_{drag}^H$, where C_{drag}^H is the local homogeneous drag coefficient. Yick *et al.* [75] showed experimentally and numerically that $\hat{C}_{drag}^S \geq 1$, and that it increases with the particles viscous Richardson number $Ri_p = a^3 N^2 / w_s \nu$, where ν is the kinematic fluid viscosity. This behavior is shown in figure 3.5. The particles viscous Richardson number, defined as $Ri_p = Re_p / Fr_p^2$, where $Re_p = w_s a / \nu$ and $Fr_p = w_s / (Na)$, expresses a balance between buoyancy, inertial and viscous forces. The fact that $C_{drag}^S \geq C_{drag}^H$ implies that the particle settles slower in a stratified fluid than in an homogeneous one, where the homogenous fluid corresponds to $Ri_p = 0$.

The reduction of the sedimentation velocity can be explained by considering the entrainment of fluid on the contour of the particle. Given that the particle entrains the surrounding fluid with it, it is useful to consider an apparent particle in which the size and density of this apparent particle is modified with respect to the original particle. Let us consider the example of an apparent particle with density and volume ρ_a and V_a as a consequence of a particle of density and volume ρ_p and V_p in sedimentation which entrains a volume of fluid V_e with density ρ , so that $V_a = V_p + V_e$. Now, we consider the two cases illustrated in figure 3.6, that is: the particle settles in a homogeneous fluid of density ρ_2 producing an apparent particle of density ρ_a at the height z_1 ; and the particle settles in a fluid in which density increases with depth, from the density ρ_1 to ρ_2 , where $\rho_1 < \rho_2$, producing an apparent particle of density ρ'_a at the height z_1 .

If we consider the gravitational force on the apparent particle when descending to the position z_2 , one can see that this force is proportional to the difference of density between the apparent particle and the surrounding fluid. To compare the sedimentation of the particle in the homogeneous fluid and in the stratified fluid, we consider the gravity force exerted on the apparent particle when displaced to the position z_2 . The apparent particle

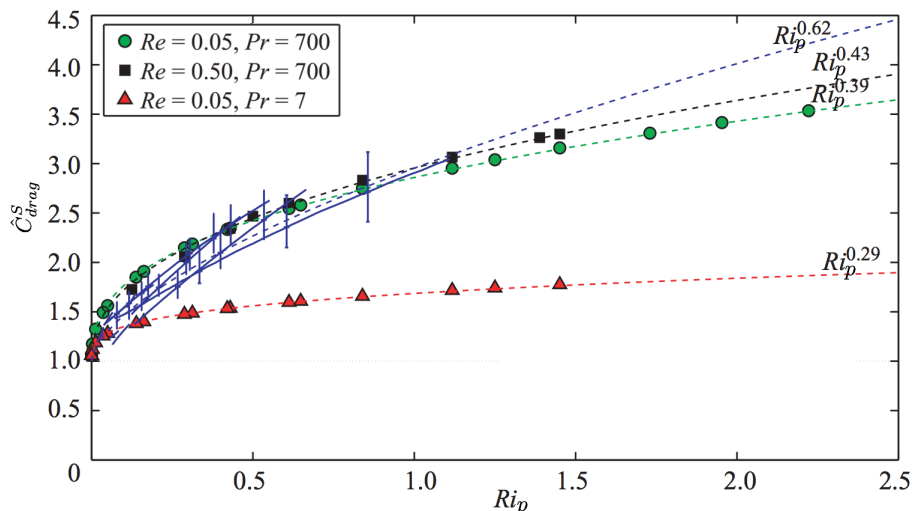


Figure 3.5: Drag coefficient \hat{C}_{drag}^S of a sphere in a stratified fluid as a function of Ri_p . Adapted from Yick *et al* [75].

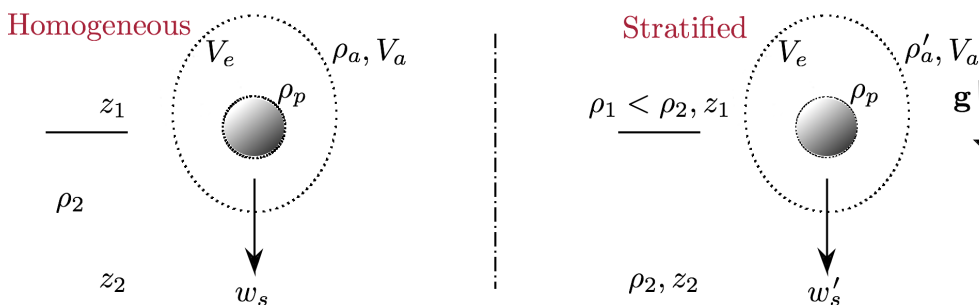


Figure 3.6: Sketch of a particle in sedimentation. On the left side of the sketch, the particle is in a homogeneous fluid with density ρ_2 . On the right, the particle is in a stratified fluid in which density increases with depth, going from ρ_1 at the top to ρ_2 below ($\rho_1 < \rho_2$). To indicate the entrainment of fluid in the boundary of the particle a dotted circle is drawn around the particle.

with density ρ_a feels a force $F_g^H = (\rho_a - \rho_2)V_a g$, whereas, the apparent particle with density ρ'_a , feels a force $F_g^S = (\rho'_a - \rho_2)V_a g$. The difference between the two forces will then be,

$$F_g^H - F_g^S = (\rho_a - \rho'_a)V_a g. \quad (3.10)$$

Considering that the volume of entrained fluid V_e is equal in both cases the apparent density will then be, $\rho_a = (V_e \rho_2 + V_p \rho_p)/V_a$, and $\rho'_a = (V_e \rho_1 + V_p \rho_p)/V_a$, so that $F_g^H - F_g^S = (\rho_2 - \rho_1)V_e g > 0$. One would expect that the particle in the lighter surrounding will sediment faster downwards, nevertheless, what is most influential over the sedimentation is the change in the density of the surrounding fluid. The particle entrains lighter fluid and becomes more buoyant. Through this simple but representative example one can see that the gravity force exerted over the particle in the homogeneous fluid is stronger than in the stratified fluid.

Another important aspect to notice is that stratification tends to suppress vertical motion of fluid. To see this let us consider the displacement of a particle of fluid (a volume of fluid in which the density is considered constant). When the particle of fluid is displaced from equilibrium in the horizontal direction, no force will inhibit the particle motion other

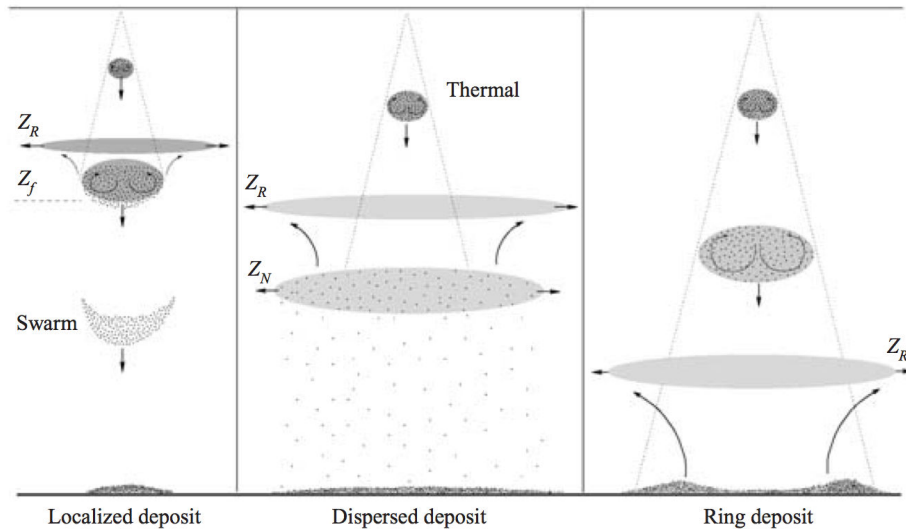


Figure 3.7: Particle cloud sedimentation. Three different scenarios are present, when the deposit is localized, disperse and in ring shape. Extract from Bush *et al.* [10]

than the drag force. On the other hand if the particle is moved vertically, energy will have to be spent in order to overcome the potential energy related to the difference of density between the particle of fluid and the new surrounding. This effect prevents the formation of eddies and therefore particles horizontal dispersion as they are settling, making the trajectory of the particles considerably more straight downward than when the fluid is homogeneous.

Collective grains settling

Now that we have presented the behavior of one settling particle, we proceed to describe the case in which many particles (particles cloud) settle in a fluid.

In order to describe the complete process of particles sedimentation it is useful to distinguish two regimes. When the number of particles forming the particle cloud is very small then, the dynamics will be dominated by the behavior of a single particle in sedimentation, which has been previously described in section 3.2.3. For a sufficiently large number of particles, the cloud behaves as a second phase of fluid. And therefore if strong motion exists, the particles cloud will present characteristics of a negatively buoyant plume. A plume is a column of fluid moving through another which can be driven by momentum and/or buoyancy. A plume grows by turbulent entrainment, in consequence, its radius (distance between the axisymmetric vertical axis and the boundary of the plume) increases linearly with distance from the source, as the density difference between plume and ambient decreases. In a homogeneous environment a plume grows indefinitely; on the other hand, in a stratified fluid, the plume is continually reduced until it stops growing and intrudes at its neutral buoyancy height (in some cases the plume rebounds up to a height Z_R after the particles rain down from the intrusive fluid). This description can vary significantly for cases that exceed the interest of this work, for example, if the density difference between plume and ambient is very large, or if the plume has significant initial momentum.

In summary, when particles are introduced from above in a stratified fluid, the particles will first form a particle cloud that will behave as a plume, followed by a later state in which the particles rain out of the cloud as individuals. The settling of the particles in a stratified fluid can be reduced to three possible scenarios as illustrated in figure 3.7, depending on

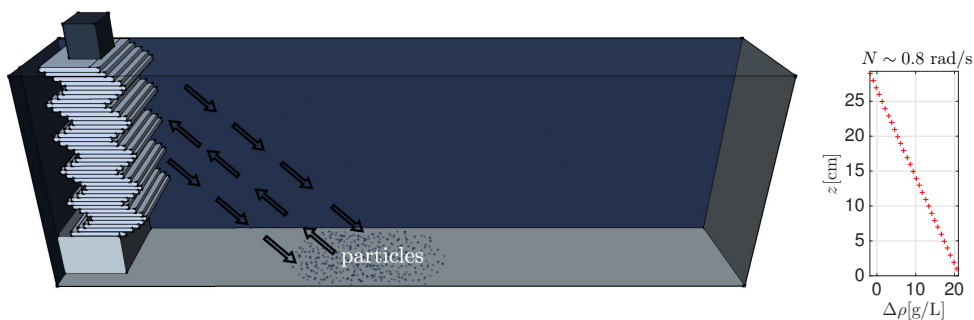


Figure 3.8: Schematics of the experimental setup used to study particle transport by internal gravity waves. The internal waves are generated at the side of the tank thanks to a wave generator. The particles are deposited at the bottom boundary in the region where the internal waves will pass through. On the right is plotted an experimental measurement of the density (crosses) as a function of the water depth.

Table 3.1: Main parameters of the experimental configurations used to study transport and erosion of sediment grains (S.S. represents Synthetic Schlieren technique).

particles	deposition	view	generator	A [cm]	λ^g [cm]	View	slope
PVC	mountain	front	vertical mode	1	30	S. S.	No
Hollow glass	bed	above	plane waves	1.5	4	S. S.	No
Hollow glass	bed	above	plane waves	1.5	4	S. S.	Yes
Polystyrene	bed	above	vertical mode	1	30	S. S.	Yes

the relative magnitudes of: the depth between source and bottom H , the fall out height Z_f which is the height where the particles separate from the cloud as individuals, and the intrusion height Z_N , which is the height where the plume reaches buoyancy equilibrium with the surrounding environment. The deposition of particles will be localized when the particles fallout of the cloud before reaching the neutral height. The deposition will be dispersed when the particles settle irregularly at the neutral depth Z_N , and then rain down. The latest case occurs when the cloud maintains its plume form through all the descent, that is, $H < Z_f$. In consequence, the plume collides with the bottom as a turbulent vortex ring generating a doubly peaked deposition pattern.

For a more general description of sedimentation of cloud particles in a stratified fluid see [10]. One can then use these different scenarios according to the deposition pattern desired. In the work presented in this thesis we will make use of the first two scenarios described.

3.3 Conditions in the Laboratory

We present the experimental setup used in this work to study sediment transport and erosion in a stratified fluid where internal gravity waves interact with settled grains.

Experiments are done in a tank 80 cm long, 17 cm wide and 42 cm deep, filled with 36 cm of salt water. Using the two bucket method described in section 2.1.1, the fluid is linearly stratified in density in order to produce a constant buoyancy frequency N . Vertical density measurements are performed with a conductivity probe along the tank.

Table 3.2: Size and density of particles used to study particle transport.

compound	$d[\text{cm}]$	$\rho_p[\text{g.cm}^{-3}]$
PVC	0.02 ± 0.01	1.4
Polystyrene	0.02 ± 0.01	1.05
Hollow glass	0.001 ± 0.0005	1.1

The generation of internal waves is performed by a moving boundary generator described in detail in section 2.1.3, which is positioned vertically at the side of the tank as sketched in figure 3.8. Two types of displacement profiles have been used: plane waves profile, and vertical mode profile, which are detailed in section 2.1.3. The velocity of the fluid is measured using synthetic Schlieren technique detailed in section 2.1.4.

After the tank is filled by the stratified salt water, particles introduced from the top surface of the fluid are deposited on the bottom of the tank. This procedure is performed by introducing particles through a sifter placed above the fluid at the horizontal location where one wants the particles to be deposited. A small amount of particles are placed in the sifter which is shaken producing the fall of the particles over the surface of the fluid. The particles will stay momentarily attached to the surface because of surface tension. After the accumulation of enough particles at the surface of the fluid, the particles weight overcomes the surface tension and the particles sediment inside the fluid. The particles experience turbulent 3D dynamics before raining straight down as described in section 3.2.3.

Three experimental configurations have been used for the study of particles transport. These experiments aim at observing the effect internal gravity waves on particles settled in the lower boundary of the tank. These configurations are:

1. In the first experiment a mountain-shaped pile of particles is built on the bottom boundary of the tank.
2. The second experiment consists in producing a shallow horizontal bed of particles in the bottom of the tank.
3. Finally, particles forming a bed are deposited on an oblique slope, where reflections of internal waves are produced.

The main features of these experimental configurations are listed in table 3.1.

Three types of particles have been used to study the transport of settled grains. The characteristics of these particles are listed in table 3.2. The variety of sizes and densities of the grains allows to explore different threshold conditions of the Shields dimensionless number.

Mountain of particles

Using a localized deposition of settling particles as described in section 3.2.3, a vertically symmetric mountain-shaped pile of the PVC particles (physical characteristics described in table 3.2) is produced, about 4 cm tall and width of diameter of about 18 cm. The mountain is built as a consequence of the accumulation of particles in the same localization. The center of the mountain is located at 27 cm from the wave generator. Figure 3.9 shows an image illustrating the relative position of the mountain with respect to the generator.

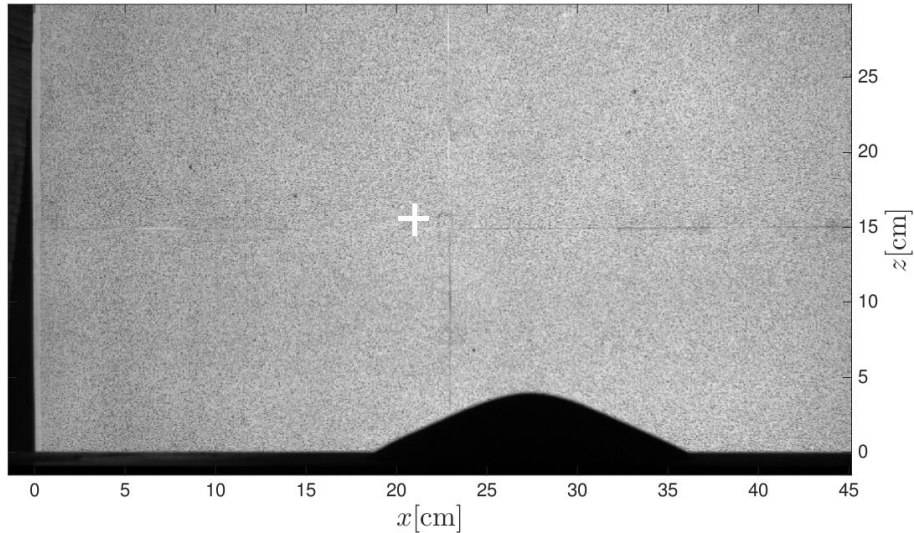


Figure 3.9: Image of the field of view. The wave generator is positioned vertically on the left of the image, the mountain-shaped pile can be observed at the bottom, and in the background one can observe the Synthetic Schlieren dotted screen. A white cross indicates the position where the time evolution of the wavefield is taken.

On the left, at the position $x = 0$ cm is located the wave generator with a vertical mode profile, with vertical wavelength $\lambda^g = 30$ cm, and amplitude $A = 1$ cm. In order to produce internal waves propagating in a linearly stratified fluid with constant buoyancy frequency, $N = 1.3$ rad/s, the wave generator is forced with a frequency $\omega_0 = 0.77$ rad/s, so that $\omega_0/N = 0.6$. The experiment is ran during 600 minutes.

The wave field is obtained by performing Synthetic Schlieren technique. The illuminated screen is used for the visualization of the change in the refractive index, and also to generate a contrast with the contour of the mountain. A camera focused on the dotted screen, is used to take 2450×1650 pixel size images, which allow to compute the wavefield. The change in height of the mountain from a front view is obtained by a 3100×2100 pixel size image taken with a 14 bits resolution Nikon D3S camera focusing on the contour of the mountain. The temporary filling of each camera is well controlled, nevertheless, the cameras are not synchronized.

Horizontal bed of particles

Introducing particles from above the fluid, a bed of hollow glass particles, described in table 3.2, is created on the horizontal bottom boundary. The thickness of the bed is approximately 10 times the diameter of the particles. The particles are deposited in a region such that the distribution of particles is homogenous over the width of the tank and occupying between 10 and 15 cm along the bottom of the tank. The bed of particles is centered in the position where the center of the wave beam will reflect with the bottom boundary, 35 cm from the generator, as schematized in figure 3.8. Internal plane waves are generated and propagate in a linearly stratified fluid with buoyancy frequency $N = 0.8$ rad/s, the vertical wavelength and amplitude of the wave generator are $\lambda^g = 4$ cm and $A = 1.5$ cm respectively. The forcing frequency of the generator is $\omega_0 = 0.41$ rad/s, so that the angle of propagation of the wave is 30° . The experiment is run during 200 minutes. In order to obtain the wavefield, Synthetic Schlieren technique is performed. During this

time, top view images of the bed of particles are taken with a Nikon D3S camera located above the tank in order to observe movement of the grains.

Bed of particles on a inclined slope

The experimental configuration presented here consists in generating a bed of particles as presented in the above experimental configuration, only that in this case, the bed of particles is created over an inclined slope in which the internal waves will reflect. For this configuration we use a 160 cm long tank, so that the reflected wave propagates away from the region of interest without perturbing twice the field of view. This experiment is motivated by the peculiar properties of internal waves reflection which can enhance the shear stress near boundary as has been described in section 1.1.4.

We will present results of two representative experiments, that have a different forcing profile. The first consists in generating internal plane waves with vertical wavelength and amplitude $\lambda^g = 4$ cm and $A = 1.5$ cm respectively, in a linearly stratified fluid with $N = 1.3$ rad/s. The slope is inclined 20° from horizontal, and the waves are forced at the frequency $\omega_0 = 0.44$ rad/s, so that the angle of propagation of the waves is the same as the angle of the slope. The granular bed is composed by PVC particles. The second experiment consists in generating internal waves with a vertical mode profile with $\lambda^g = 30$ cm and $A = 1$ cm, in a fluid with $N = 1.43$ rad/s. The forcing frequency was varied around $\omega_0 = 0.33$ rad/s, which is the frequency that will be critical for the inclination of the slope, equal to 13° . The bed of particles is composed by the polystyrene particles. In both cases, the wave field is obtain by performing Synthetic Schlieren technique, and top view images of the bed of particles are taken with a Nikon D3S camera located above the tank.

3.4 Results

We studied the behavior of settled particles when forced by internal wave perturbations for different configurations. The results presented in this section aim to relate the grain behavior with the internal wavefield, which are measured independently and simultaneously.

3.4.1 Particles in a mountain-shaped pile

The characteristic time of a single particle motion is much smaller than the internal wave period. For this reason, in order to observe both, particle displacement and the internal wavefield during many periods, we will focus in the average displacement of the grains and not in the individual grain movement.

Shape of the mountain

The evolution in the shape of the mountain of particles after the passage of internal gravity waves can be observed from a front view image in figure 3.10. Figure 3.10(a) and (b) respectively show the profile of the mountain before the internal waves are generated, at $t = 0$, and after 4000 periods of the internal waves, that is at $t/T = 4000$, with $T = 2\pi/\omega_0$, where ω_0 is the forcing frequency. Initially the shape of the mountain presents a more pronounced peak than after the passage of the waves, where, the mountain is stretched horizontally.

The height profile of the mountain at different times, which we name $h(x, t)$, is illustrated in figure 3.11. Initially the contour does not vary significantly. After $t/T \sim 900$ the contour presents an abrupt change where the peak of the mountain profile is reduced by

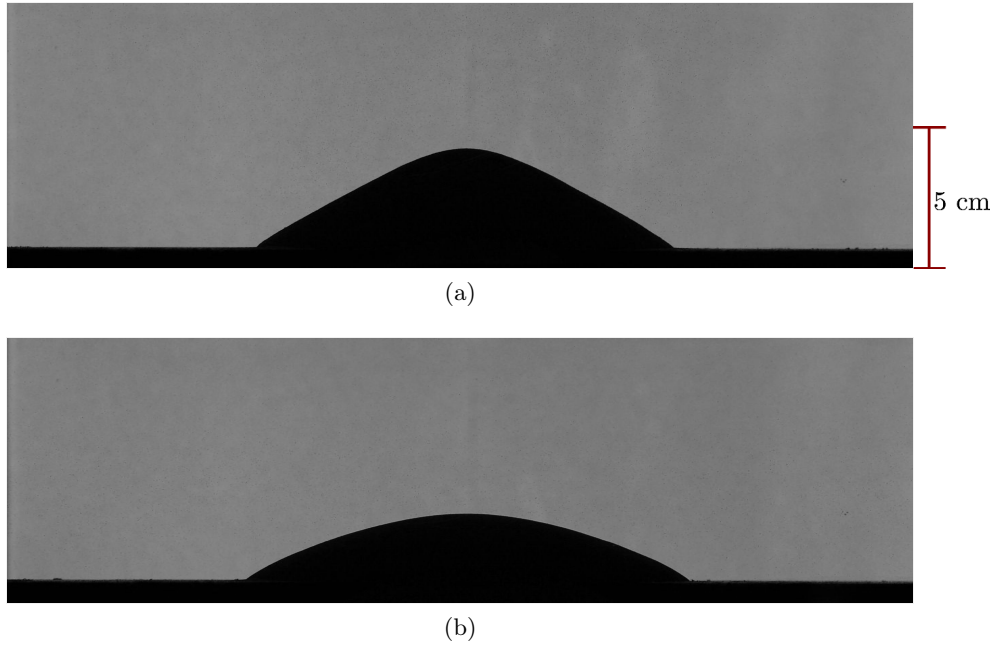


Figure 3.10: Front view of the mountain of particles for $t/T = 0$ (a), and for $t/T = 4000$ (b).

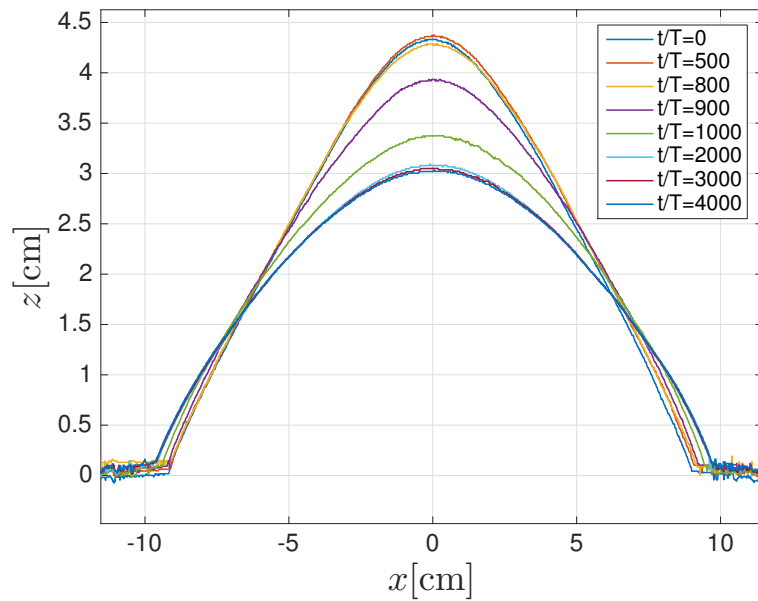


Figure 3.11: Height of the mountain $h(x, t)$ for different instants.

30% and the mountain is spread horizontally at the base, until $t/T \sim 2000$, after which the contour barely changes. The change of the shape of the mountain in time can be observed more synthetically by considering the evolution in time of the maximum height of the contour. It is plotted in figure 3.12(a) the height of the profile as a function of time and normalized by the height of the mountain averaged over the first $100 T$. The rapid change in the shape of the mountain is evidenced in the evolution of the maximum height at $t/T \sim 1000$.

The profile height of the mountain is symmetrical with respect to the center of the

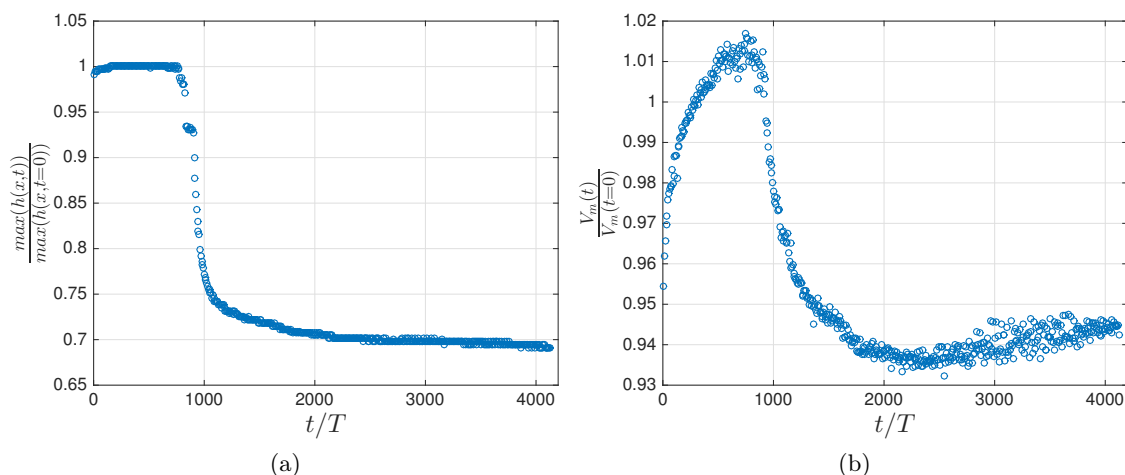


Figure 3.12: Evolution in time of: (a) the normalized maximum height of the contour, and (b) the normalized volume of the mountain.

mountain. This symmetry is conserved throughout the evolution of the shape of the mountain, even though the wave generator is located on one of the sides of the tank only.

Considering that the mountain presents symmetry of rotation with respect to the center peak, we can estimate the volume of the mountain for every instance t . We will then write $h(r, t)$ instead of $h(x, t)$, where r is the distance between the center vertical axis of the mountain ($x = 0$ for figure 3.11) and the boundary of the mountain. We define,

$$V_m(t) = 2\pi \int_0^r h(r', t)r' dr', \quad (3.11)$$

which is the volume of the mountain as a function of t . In figure 3.12(b), we show the evolution of $V_m(t)$ in time, normalized by the volume of the mountain averaged over the first 100 periods T .

The plot of figure 3.12(b) shows variations in the volume of the mountain of the order of $\pm 4\%$ with respect to the initial value. Initially the volume of the mountain increases, and at $t/T = 900$ the volume decreases until $t/T = 2000$ where it settles. Given the way the mountain is constructed, it will be initially in a loose packing state. Under these conditions it is very unlikely to have an increase in the volume of the mountain. We believe that the change in volume detected is related to the fact of supposing valid that the mountain conserves symmetry of rotation with respect to his center. This is based on the fact that there is no considerable change in $\max(h(x, t))$ before $800 T$ as shown in figure 3.12(b). If the height does not increase but the volume does, then we can expect a increase of the width of the mountain on the slopes. If the rotation symmetry is not conserved there will be positions of the mountain at the same height with different inclinations of the slope. In the way the mountain is constructed, the angles of the slope are slightly underneath the avalanche angle, and therefore a small perturbation can trigger an avalanche. Since some regions have steeper slopes than others, the distribution of avalanches would not be the same. This not uniform distribution of avalanches will change the symmetry of the mountain and therefore the height profile, with no need of modifying the height $\max(h(x, t))$, and hence modifying the volume V_m . Unfortunately we did not measure accurately the rotation symmetry of the mountain when performing this experiment, thus this idea remains

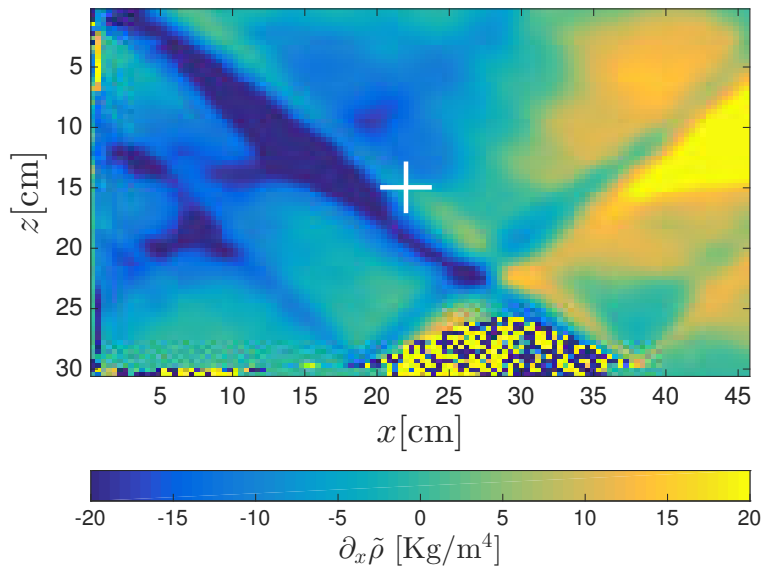


Figure 3.13: Snapshot of the wavefield generated by a vertical profile mode for $t/T = 300$. The mountain of particles is centered at 27 cm from the wave generator, and acts as a source of waves. A white cross indicates the position where the time evolution of the wavefield is taken.

as an hypothesis since the dynamics of the shape of the mountain depends strongly on the initial conditions of the experiment which can be changed with a slightly perturbation.

At approximately $T/t = 900$ there is an abrupt change in the shape of the height profile, in particular a decrease of $\max(h(x, t))$. As we will discuss below, this effect is related to a qualitative change of the velocity field. The change in the shape of the mountain produces an effect on the volume of the mountain V_m as can be observed in figure 3.12(b). This change in volume can be in part related to a change in the symmetry of the mountain because of avalanches, however the main effect is probably a compaction effect on the mountain.

Wave field

As mentioned, the internal gravity waves are generated by a vertical mode profile. The wave perturbation will propagate and will be reflected on the boundaries and on the mountain of particles. The reflections of the vertical mode on the mountain will generate new waves. These waves will be mostly generated in a region of the mountain where the slope angle matches the direction of propagation of the internal waves [76]. In figure 3.13 is shown a snapshot at $t/T = 300$ of the wavefield over the mountain of particles. We can observe two large patches on the wavefield with different sign at the right and at the left of the mountain, this is the outcome wavefield of the wave generator. In addition, two beams are produced at the slopes of the mountain and propagate upwards.

Figure 3.14 shows the time evolution of the horizontal gradient of the density $\partial_x \rho$ between $t/T = 0$ and $t/T = 1550$, for a point located above the mountain (indicated with a white cross in figure 3.9 and figure 3.13). Given the fact that the experiment is very long (~ 1500 periods of the wave) it is expected that mixing will occur, therefore, the horizontal gradient of the density is produce by the sum of: the fluctuations of the density profile (internal waves) and the variation of the average density profile (mixing). These magnitudes are related through the relationship: $\partial_x \rho = \partial_x \tilde{\rho}(t) + \partial_x \bar{\rho}(t)$.

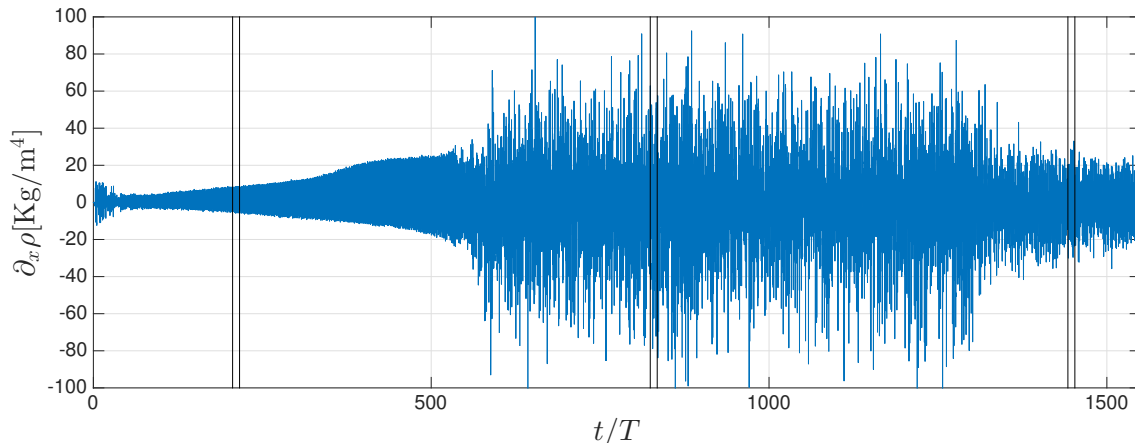


Figure 3.14: Time evolution of $\partial_x \rho$ as a function of t/T . Three pair of vertical lines indicate time intervals that will be detailed in figure 3.15.

Three different situations can be distinguished, which are detailed in figure 3.15 with a zoom in time. From the start to $t/T \sim 600$ the wave field oscillates with the dominant frequency ω_0 and the amplitude increases monotonically (figure 3.15(a)), then the wave field is less monochromatic and presents strong variations in the amplitude (figure 3.15(b)), until $t/T \sim 1300$ where the wave field becomes again dominated by the forcing frequency ω_0 (figure 3.15(c)).

Between $t/T \sim 600$ and $t/T \sim 1300$ the Synthetic Schlieren technique cannot resolve the wavefield, we deduce in consequence, that overturns occur in the density field and therefore the changes of refractive index cannot be obtained through this method. Even though we do not have access to the wavefield, this behavior is an indication that the wavefield is non-linear, which can be corroborated by the strong change of the density profile (shown in figure 3.16) measured before and after performing the experiment.

In a control experiment without the mountain of particles, after several wave periods T , we observe as well the appearance of many frequencies related to non-linearities in the wavefield. The mixing generated by internal gravity waves in similar experimental configurations has been study by Bourget [8] through parametric subharmonic instabilities, and by Brouzet [9] through internal wave attractors. Nevertheless, the non linear behavior of the wavefield within all the depth of the tank has not been observed yet, probably because in the experiment presented here the experimental parameters have been chosen to intensify as much as possible the characteristic velocities, which is not the case in the works before mentioned. In addition, the experiment is performed for longer time than the ones performed by Bourget and Brouzet.

Conclusions: mountain of particles

The mountain-shaped pile of particles has been used to study grain transport behavior induced by internal waves because it reproduces some particular oceanic conditions: the slope of the mountain changes for different positions generating diverse conditions for the settled grains in the contour; the mountain height is large enough so that the difference of densities of the fluid at the bottom and at the top of the mountain are appreciable.

We have observed that after the passage of a vertical mode internal gravity wave, there is a change in the shape of the mountain of particles, in particular when the wavefield presents strong non-linearities. We infer that the change in volume and height of the

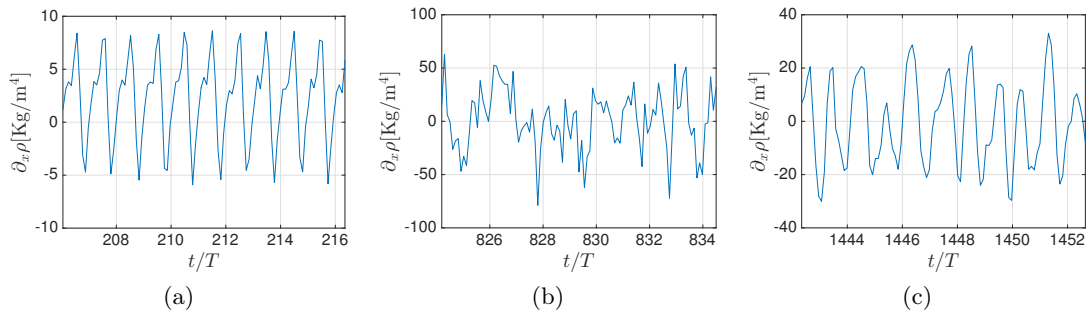


Figure 3.15: Time evolution of $\partial_x \rho$ for three time intervals detailed with pairs of vertical lines in figure 3.14, (a) corresponds to the pair of lines on the left, (b) at the center and (c) on the right. Note the change in vertical scales between the three graphs.

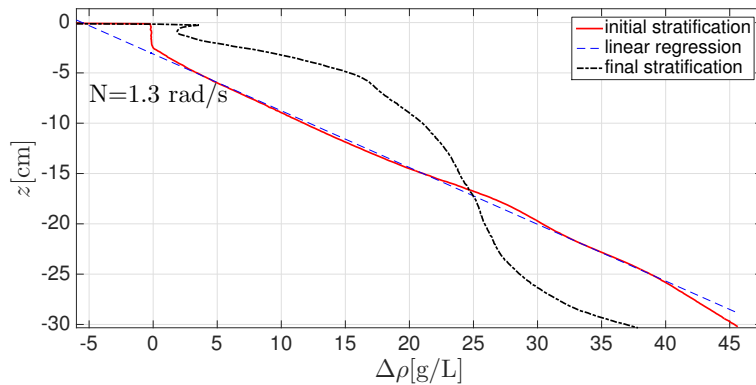


Figure 3.16: Measurements of the density profile, where $\Delta\rho = \rho - 1000$ g/L, for the initial state before internal waves are generated, and for $t/T = 4000$. The linear approximation of the initial density profile is plotted with dashed line.

mountain is produced by two main effects: avalanches and compaction. In a first stage the avalanches are the dominant effect in the change of shape of the mountain. After the wavefield becomes non-linear, there is compaction of the mountain and a decrease of the maximal height of the mountain.

There is no distinguishable difference in the symmetry of the height profile $h(x, t)$ respect with the center of the mountain, despite the fact that the generator is positioned in one particular side of the setup, we conclude that no bed load transport is then present.

Large velocities are needed in order to produce large shear stresses at the contour of the mountain. We used a vertical mode profile which is the wave generator that injects the highest energy rate in the stratified fluid. The presence of the mountain together with the long duration of experiments generated perturbations in the fluid that enhanced mixing. This complex outcome process in the wavefield inhibits the possibility of quantifying the effect of internal waves over the grains. Therefore, we proceed to use internal waves generated with a plane wave profile, which are less energetic than the vertical mode, and are less likely to produce turbulence and mixing.

3.4.2 Particles in a horizontal and inclined bed

A snapshot of the wave field of the second experimental configuration described in section 3.3 can be observed in figure 3.17. The plane waves propagate from the top-left side

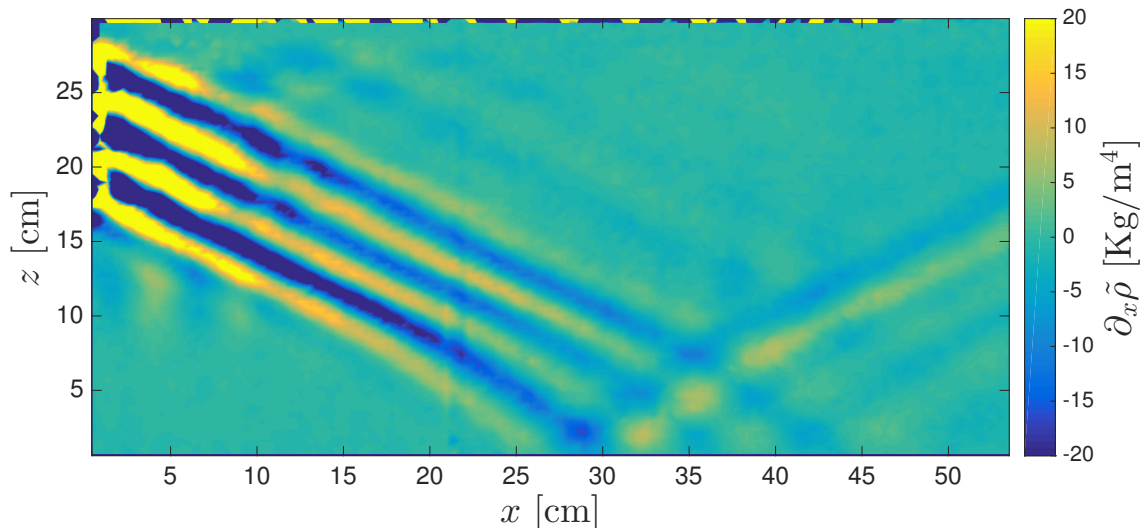


Figure 3.17: Snapshot of the wavefield of a plane wave propagating from left to right and reflecting on the bottom.

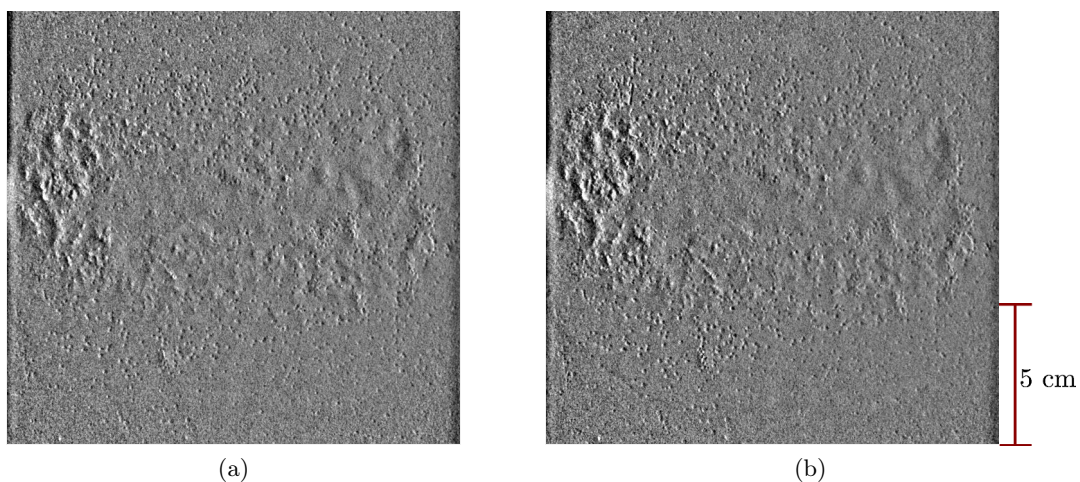


Figure 3.18: Image of a bed of particles taken from above, before internal waves are generated in the tank (a), and for $t/T = 500$ (b), where T is the period of the wave. No significant change in the bed is observed between these two moments.

of the image and reflects on the bottom boundary. The intensity of the wave decreases as it departs from the source. The center of the beam reflects on the bottom boundary at 35 cm from the wave generator, where the bed of particles is located. No change in the stratification profile has been observed during the course of this experiment.

The particle bed motion was controlled by images taken from above the position of the bed, as shown in figure 3.18, (a) before the waves are generated, and (b) after 500 periods of the wave. During the course of the experiment no appreciable difference was observed in the bed of particles, and therefore, we conclude that no motion of grains was induced.

To generate larger shear stress over the bed of particles, and yet make use of plane waves, we used the property of internal waves focusing over an oblique slope. Figure 3.19 shows a snapshot of the wavefield of internal plane waves, corresponding to the third experiment described in section 3.3. The plane waves propagate from the upper-left corner

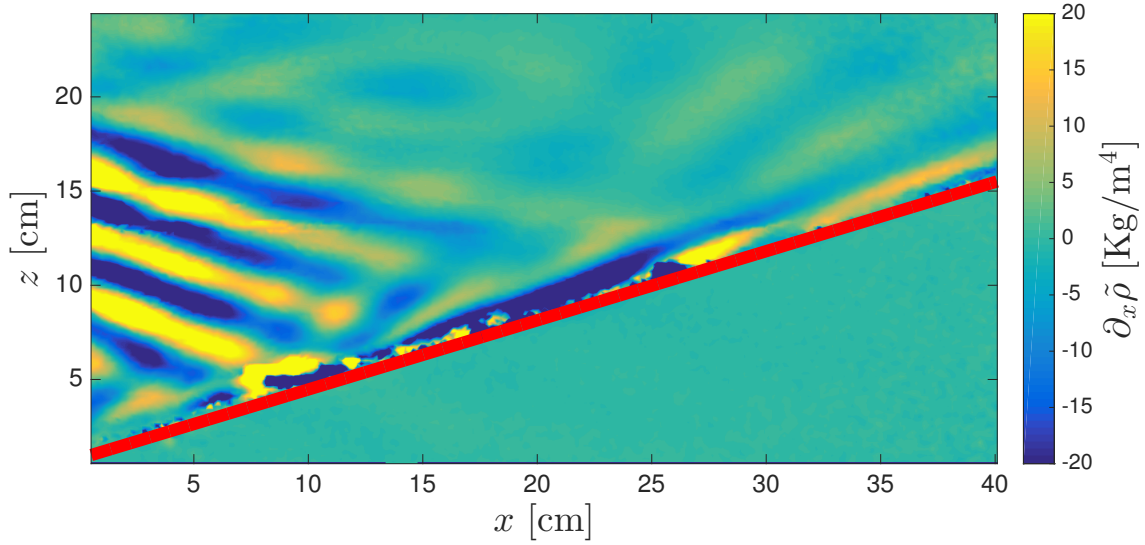


Figure 3.19: Snapshot of the wavefield of a plane wave propagating from left and reflecting over an oblique slope (indicated with a red line).

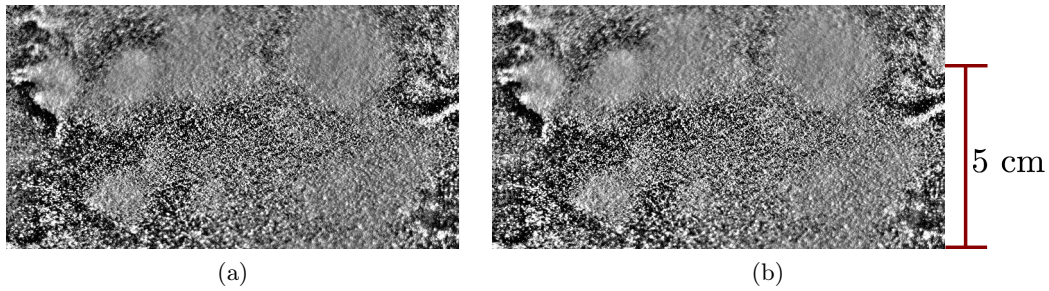


Figure 3.20: Image taken from above of a bed of particles located in an oblique slope, before internal waves are generated (a), and for $t/T = 400$ (b). No movements of grains is observed between these two moments.

to the lower-right corner and is reflected on the sloped boundary (indicated with a red line in figure 3.19). After reflecting, the waves propagate up along the slope in a narrow section which evidences focusing of the wave. This effect is produced by forcing the waves to propagate at an angle $\beta = 20^\circ$ equal to the angle of the slope γ .

Again, the particle bed was observed by images taken from above the position of the bed. No perceptible particle motion has been observed after the reflection of internal plane waves over the bed of particles in a near critical reflection during 400 periods. The lack of grain movement can be appreciated in figure 3.20(a) and (b), which shows no differences in the initial and final state of the bed of particles.

Finally we proceeded to force internal waves in a sloped experimental configuration with a vertical mode profile. Despite the fact that mixing can be generated and the wavefield can become complex and non-linear, larger shear stress are produced at the boundary where the bed of particles is located, when a near critical reflection occurs. As in previously described experiments, no particle motion was detected.

3.5 Conclusions of bed load transport

We have performed several explorative experiments in order to study the behavior of settled particles, when motion is induced by internal waves. In order to produce a large shear stress over settled grains, we started using a vertical mode profile to generate internal waves, which is the profile that creates the most intense velocity field. We observed a change in the shape of a mountain of particles located at the bottom boundary in a linearly stratified fluid after the passage of a vertical mode wave, in particular, when the non-linearities in the wavefield increased. The change of the shape of the mountain is very sensible to the initial conditions of the construction of the mountain, and we did not find any evidence of bed load transport. Nevertheless, we inferred that the change of shape and size of the mountain is consequence of avalanches in the slope of the mountain and compaction in the interior of the mountain.

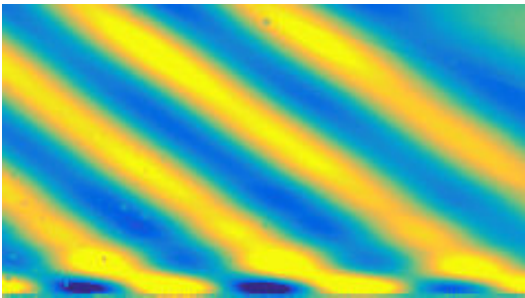
The complexity of the wavefield when mixing occurs, inhibits the capability to quantify the relation between the change in the shape of the mountain and the wavefield. For this reason we pursued our investigation by generating internal plane waves which are less likely to generate mixing.

The first experiment with plane waves reflecting on the bottom boundary at the position where the bed of particles was located did not induce any perceptible grain movement. In order to generate a larger shear stress over the bed of particles, and still use plane waves, we used the focusing property of internal waves when reflecting over an oblique slope in critical and near-critical configurations. Again no bed load transport has been observed in this case. Finally, critical and near critical reflections of internal waves have been produced with a vertical mode profile, to generate the largest possible velocity field and therefore a large shear stress σ . No grain motion was observed in the bed for this configuration.

We have observed an increase of the intensity of the wave field near the boundary when an internal wave reflects at an oblique slope with the same angle as the direction of propagation of the wave. The particular property of internal waves reflection produces, in the critical and near-critical cases, an increase of the intensity of the along-slope component of the velocity field in a thin layer near the boundary. This behavior permits to increase significantly the shear stress, and therefore enables to approach the threshold that allows particles to move. In the next chapter we will study in detail the velocity field near the boundary for critical and near critical reflections for a wide range of experimental parameters. This will be performed thanks to PIV visualization technique described in section 2.1.4, which allows to capture the velocity field even if non linearities are present in the wavefield.

The main interest of the work presented in this chapter was to produce bed load transport of settle particles by inducing motion through internal gravity waves, which was not achieved. Nevertheless, we have observed that internal waves can generate motion of particles in a mountain-shaped pile, through either avalanches, compaction or both. We have not aim our experiments to observe these processes, however it can be interesting to study them. From the conclusions of our work, we propose to perform this experiment by performing improvements to our setup. First, a well controlled mountain builder should be developed, in order to perform multiple experiments with the same mountain. Second, the wavefield can be measured by performing PIV visualization technique (described in section 2.1.4), this technique allows to measure the velocity of a turbulent wavefield. However, this technique may require some adjustment to the visualization of the grain motion respect to our technique.

Internal waves reflection



Wavefield of a focalization produced by an internal wave near-critical reflection over a sloped boundary.

In this Chapter we will present the characteristics of internal gravity waves reflection in the critical and near critical cases. The detailed study of this process is principally motivated by some peculiar characteristics of internal waves reflection that can enhance the shear stress developed near boundaries.

The separation of incident and reflected wave in the reflection process is crucial to the understanding of the velocity field in the proximity of the boundary. Two methods are presented in order to achieve this goal: the Hilbert transform method used previously

and, an innovating variational method (developed in collaboration with researchers from the signal processing community [61]), which takes into account the particular characteristics of internal waves reflection.

We will compare high resolution measurements of the velocity field close to the boundary with a theory for critical wave reflection developed by Dauxois & Young. In addition this measurements will allow us to estimate the shear stress σ near the boundary for experiments ranging an interval in the Reynolds number $Re \sim 5$ to $Re \sim 600$. The agreement between experimental results and theory allows to predict through the Shields approach, if erosion of particles in a bed will be achieved for a particular experimental configuration and particles characteristics.

4.1 Critical reflection: Singularity and localization of the reflected wave

As shown in section 1.1.4 in the linear theory of internal waves reflection, it is expected for a critical reflection, the reflected wave to present some singularities:

- The wavelength is equal to zero, $\lambda^{refl} = 0$,
- The amplitude is equal to infinity,
- The group velocity is equal to zero.

The reflected wave will focus at a boundary on a layer with zero width. As the energy of the incident wave is conserved during the reflection, the energy density is expected to be infinite at the boundary. In consequence, the along slope velocity at the boundary and apart from it will present a jump. This is equivalent to an infinite shear stress σ at the boundary.

The particular characteristics present in the linear theory developed by Phillips indicates that this theory does not solve the problem of an internal wave reflection in the critical case. The presence of the singularity suggests the existence of a mechanism, not taken into account in the theory that prevents the singularity from developing. The existence of a mechanism that heals the singularity is supported by our measurements as well as other previous observations [12], [37] and [20].

Many efforts have been done in order to heal the singularity present in the linear theory. The advances done in this field rely on the belief that the absence of this singularity is due to viscosity and/or non-linearities ([72], [43], and [63]).

In the theory developed by Dauxois & Young [19] it is shown that the singularity present in a critical reflection of a weakly nonlinear internal gravity wave can be healed, by using a matched asymptotic expansion, either through dissipation or transience.

4.2 Experimental setup and system description

4.2.1 Schematic configuration and coordinate systems

Many possible configurations exist in order to generate an internal wave reflection over an oblique slope. The reflection process can generate focusing or defocusing of the reflected wave. Given that the main interest is to describe critical and near-critical reflections, we will present in this work only results in which focusing occurs.

The configuration used to study the reflection process is schematized in figure 4.1. Imposed by the frequency of the wave generator ω_0 , the incoming wave propagates from up-left to down-right at an angle β with respect to the horizontal. It reflects on an oblique slope tilted at an angle γ with respect to the horizontal and propagates away from the slope.

Higher order frequencies are generated through non linear interactions between the incident and reflected waves. This process is thus decomposed in several waves: the incident wave, which propagates before touching the boundary, the reflected wave which conserves the temporal frequency ω_0 , and the higher order waves that are product of the non-linearities and propagate at frequencies $2\omega_0$, $3\omega_0$, etc., where the highest harmonic will be bounded by N through the dispersion relation, that is, $\omega/N \leq 1$. We are interested in the waves that propagate near the boundary for near critical-reflection, that is, the

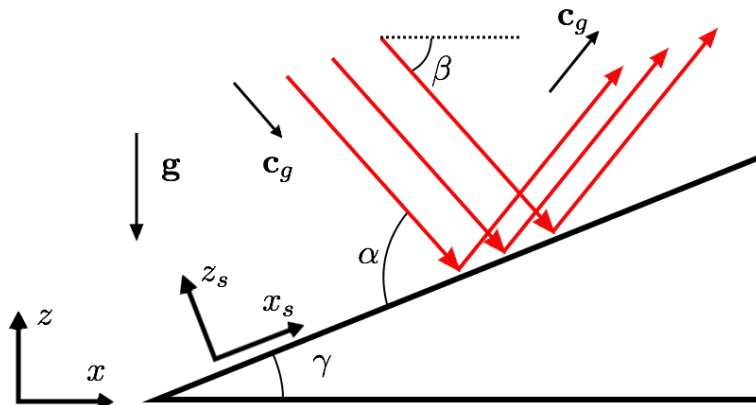


Figure 4.1: Schematic view of the incident wave reflection. The angle between the bottom slope and the horizontal is γ ; the angle between the incident group velocity and the horizontal is β , and $\alpha = \gamma + \beta$. \mathbf{c}_g indicates the group velocity and \mathbf{g} indicates gravity. The horizontal and vertical axis, as well as the axis attached to the slope, are indicated. Same illustration shown in figure 1.2.

reflected wave with frequency ω_0 , given that the waves associated with higher harmonics will propagate away from the slope.

The direction of propagation of the incident wave is defined through the angle between the group velocity \mathbf{c}_g and the horizontal; the angle between the incident group velocity and the slope is defined as $\alpha = \beta + \gamma$. Two coordinate systems will be used, as indicated in figure 4.1; x and z are the coordinates respectively perpendicular and parallel to the gravity, and x_s and z_s are the coordinates along and normal to the slope. The reflected wave will be studied for different departures from criticality and will be described as a function of the control parameters $\beta - \gamma$.

4.2.2 Experimental setup

Experiments are done in a tank 160 cm long, 17 cm wide and 42 cm deep, filled with 36 cm of salt water. Using the two-bucket method described in section 2.1.1, the fluid is linearly stratified in density in order to produce a constant buoyancy frequency N . Vertical density measurements are performed with a conductivity probe along the tank. An example of an experimental measurement of the density as a function of the height is plotted at the right side of figure 4.2.

The generation of internal waves is performed by a moving boundary generator described in detail in section 2.1.3. The wave generator is located vertically so that the displacement profile is:

$$X(z, t) = A \sin(\omega_0 t - k_z^g z), \quad (4.1)$$

where ω_0 is the forcing frequency, k_z^g the vertical wavenumber of the generator and A the amplitude. For the experiments presented in this work the amplitude of the plane wave generator varies between 0.25 and 1.5 cm, and the vertical wavelength $\lambda^g = 2\pi/k_z^g$ between 4 and 8 cm. The wave generator is located at the side of the tank as illustrated in figure 4.2.

In order to achieve critical and near critical reflections, a transparent acrylic slope with variable inclination is placed in the tank before the filling. There is no perceptible difference in the stratification density profile because of the presence of the slope. The angle of the slope γ can vary between 0° and 35° , and is 16 cm wide. The velocity of the fluid is

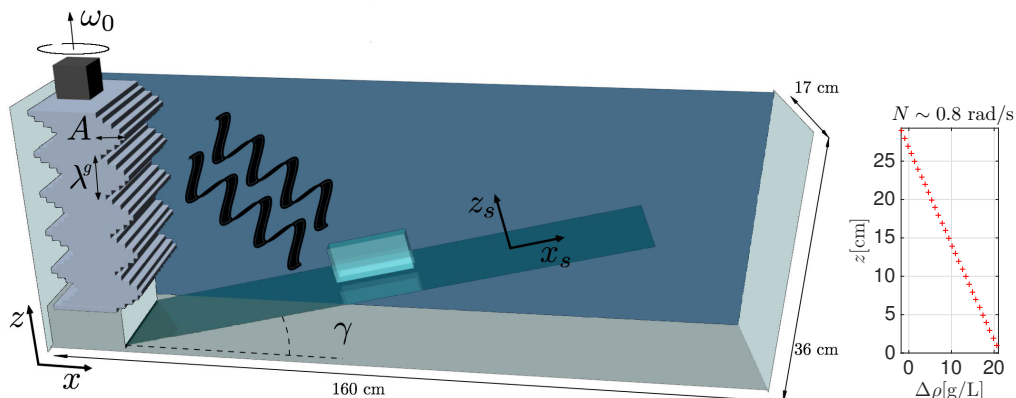


Figure 4.2: Sketch of the experimental setup. On the left of the tank is the wave generator (plane waves). A slope is introduced in the tank. Coming from the generator, the internal waves propagate from up-left to down-right as illustrated. The field of view is represented with a tilted rectangle over the slope. The control parameters are indicated in the sketch: A , λ^g and ω_0 of the plane waves generator, and the angle of the slope γ . The two systems of coordinates are indicated: x , z and x_s , z_s . On the right is plotted an experimental measurement of the density (crosses) as a function of the water depth.

Table 4.1: Control parameters for experiments. N is the buoyancy frequency, γ the angle of the slope, A and $\lambda^g = 2\pi/k_z^g$ the amplitude and vertical wavelength of the wave generator, β the angle of propagation of the incident wave, given by the dispersion relation $\omega_0 = N \sin \beta$, where ω_0 is the forcing frequency of the generator. $Re = \lambda U/\nu$ is the Reynolds number, and $Fr = U/(\omega_0 \lambda)$ the Froude number, where λ and U are the wavelength and the maximum velocity in the direction of the incident wave, and the Re and Fr number are calculated for experiments corresponding to the smallest value of $|\beta - \gamma|$ in each case. The experiments were done with planes waves, except the experiments of the two last lines, which correspond to a mode generated with a vertical profile.

Case	N [rad/s]	γ [$^\circ$]	A [cm]	λ^g [cm]	Re	β [$^\circ$]	Fr
exp1	1.15	16.5	0.25	4	5	12 - 25	0.01
exp2	1.14	15	0.25	8	17	12 - 26	0.01
exp3	1.22	15	1	4	18	8 - 22	0.04
exp4	1.1	16	1	4	16	7 - 33	0.043
exp5	1.1	16	1.5	4	23	7 - 34	0.059
exp6	1.13	16	0.5	8	32	7 - 32	0.02
exp7	1.02	17	1	8	98	11 - 40	0.05
exp8	1.02	16	0.5	30	400	8 - 28	0.016
exp9	0.82	16	1	30	620	8 - 38	0.03

measured in a vertical plane using particle image velocimetry (PIV) (see section 2.1.4 for more details). The parameters that are modified for different experiments are expressed in table 4.1.

4.3 Observations and post-processing

From the set of near-critical reflection experiments realized in this work, we will make use of the experiment with smallest value of $|\beta - \gamma|$ to describe the critical reflection behavior.

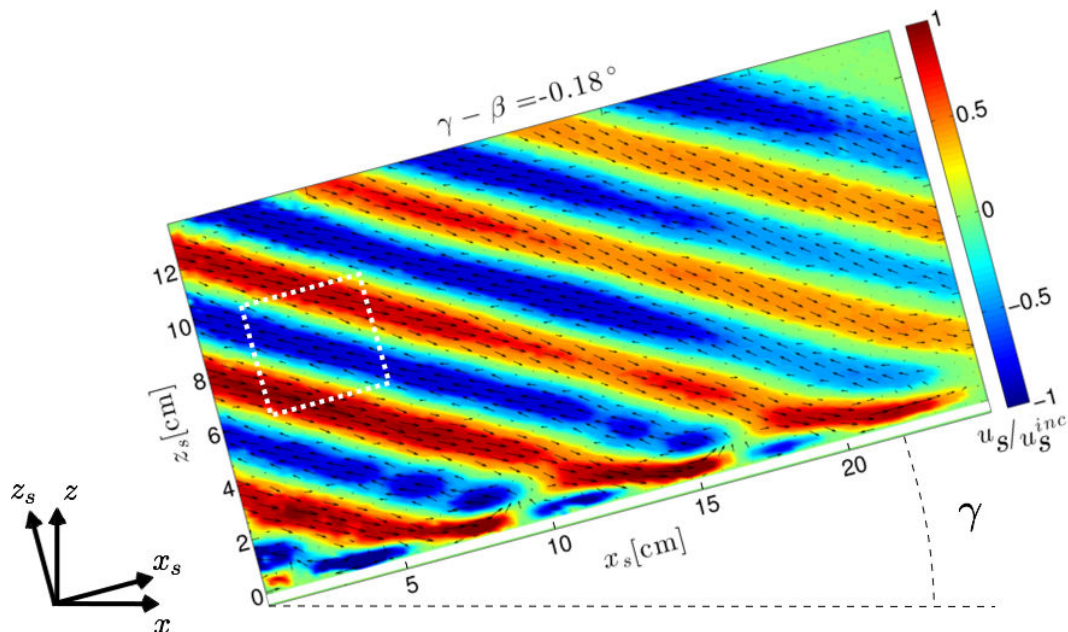


Figure 4.3: Snapshot of the normalized velocity field at $t/T = 15$. The plot is tilted similarly to the experiment in order to illustrate the inclination of the slope $\gamma = 16^\circ$. x , z and x_s , z_s coordinates are indicated. The slope boundary is located at $z_s = 0$. The background color indicates the u_s velocity component normalized by the along-slope component of the incident velocity $u_s^{inc} = 0.1$ cm/s, and arrows represent the velocity field. The incident wave is coming from left to right, and the generator is located 30 cm from the center of the image. This experiment corresponds to the case "exp3" indicated in table 4.1.

A snapshot of the velocity field of experiment "exp3", for which $\gamma - \beta = -0.18^\circ$, is shown in figure 4.3, obtained 15 periods after the wave generator was started. The incoming plane wave is reflected on the sloped boundary (at $z_s = 0$ in figure 4.3) and propagates along the slope in a narrow region producing an increase in the intensity of the velocity field, as a consequence of focusing. After a transient regime (~ 10 periods), the reflection process reaches a stationary regime. Due to viscous dissipation the intensity of the incident wave decays as the waves propagate away from the wave generator. The color indicates the intensity of the along-slope component of the velocity field, which is normalized by the amplitude of the incident wave velocity.

In order to study the reflection process it is necessary to distinguish the different waves involved in the process. The higher harmonics waves with frequencies ($2\omega_0$, $3\omega_0$, etc.) can be isolated through temporal filtering. The reflected wave will stay closer to the slope for near-critical reflections since it conserves the frequency ω_0 . This wave cannot be separated from the incident wave with temporal filtering techniques. For this, the procedure of separation of the waves will be based on the fact that the spatial wavenumber is not conserved in the reflection process.

We will now introduce temporal and spatial filtering applied to our experiments.

4.3.1 Temporal filtering

As mentioned in section 2.2, we can obtain the velocity field of an internal wave associated to each specific frequency through the following routine: a Fourier transform is performed

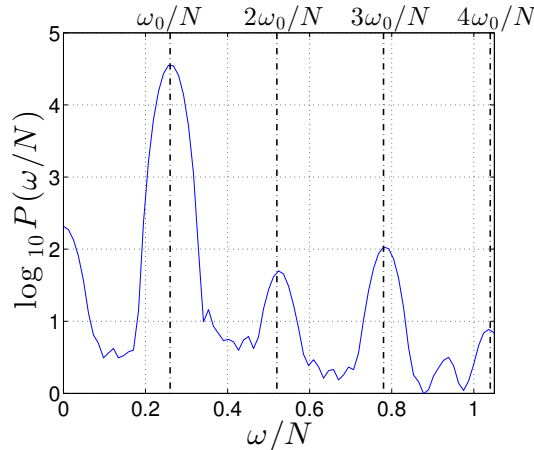


Figure 4.4: Power spectrum density $P(\omega/N)$ of u_s for a critical reflection of the experiment corresponding to figure 4.3. The spectrum is taken from a set of points located in the left side of the field of view at approximately 8 cm from the slope (indicated with a white square in figure 4.3). This experiment corresponds to the case "exp3" indicated in table 4.1, in which $\omega_0/N = 0.26$.

for the time evolution of the velocity field, then a band-pass filtering around a selected frequency is performed, and finally an inverse Fourier transform is accomplished.

Figure 4.4 shows the frequency power spectrum for the experiment corresponding to the snapshots presented in figure 4.3, taken from the region illustrated by a white dotted line square. The largest contribution is associated to the frequency $\omega_0/N = 0.26$, which comes from two waves: the wave produced by the generator forcing (incident wave), and the reflected wave with frequency ω_0 that will stay near the slope. The harmonics $2\omega_0/N = 0.52$, $3\omega_0/N = 0.78$ and $4\omega_0/N = 1.03$ are also present, with lower magnitude. One other frequency $\omega/N = 0$ has non vanishing contributions to the signal. It corresponds to the mean flow generated as a result of the non-linear interaction between incident and reflected waves.

When the temporal filter is performed over the frequency $\omega_0/N = 0.26$, the components related to the higher harmonics are removed, and the velocity field obtained will be solely associated to the incident and the reflected wave with frequency ω_0 .

Through temporal filtering the incident and reflected wave cannot be separated. A way to resolve this problem and distinguish the two waves is through spatial filtering techniques.

4.3.2 Spatial selection and Hilbert transform

In section 1.1.4 we showed that when an internal wave reflection occurs, the temporal frequency of the wave is conserved. This leads to the impossibility to distinguish these two waves through temporal filtering. On the other hand, the wavenumber of a wave is not conserved in the reflection process: to be more precise the absolute value of the along-slope component of the wavenumber is conserved, $|k_{x_s}^{refl}| = |k_{x_s}^{inc}|$, while $|k_{z_s}|$ is not.

The separation of the incident and reflected wave through the spatial spectrum is based on differentiating the wave associated to $(k_{x_s}^{inc}, k_{z_s}^{inc})$ and $(k_{x_s}^{refl}, k_{z_s}^{refl})$, which comes to discriminate between $k_{z_s}^{inc}$ and $k_{z_s}^{refl}$. Figure 4.5(a) and (b) show respectively the power spatial spectrum as a function of k_{x_s} and k_{z_s} , for the experiment corresponding to the snapshot presented in figure 4.3, after filtering around the temporal frequency $\omega_0/N = 0.26$.

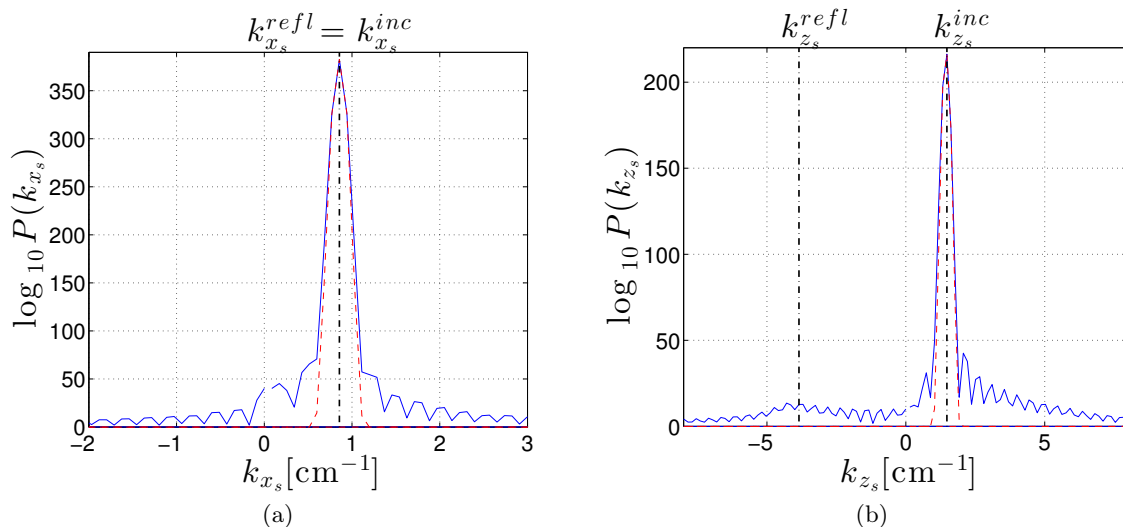


Figure 4.5: (a) Spatial spectrum (solid curve) for k_{x_s} . (b) Spatial spectrum (solid curve) for k_{z_s} ; the dashed line represents the spectrum filtered around the forced wavenumber \mathbf{k}^{inc} . With a dashed-dotted vertical line is indicated the experimental value of \mathbf{k}^{inc} and \mathbf{k}^{refl} . These spectra correspond to experiment "exp3" and $\omega_0/N = 0.26$.

For the component k_{z_s} the wavenumber of both waves can be separated in the spatial spectrum, whereas both wavenumber components overlap in the spectrum $P(k_{x_s})$.

The largest peak of these two power spectra corresponds to the wavenumber components of the incident wave. The spatial power spectrum after the spatial filtering is performed around the values $k_{x_s}^{inc} \pm \Delta k_{x_s}^{inc}$ and $k_{z_s}^{inc} \pm \Delta k_{z_s}^{inc}$ are respectively plotted as red dashed lines in figure 4.5(a) and (b), where $\Delta k_{x_s}^{inc} = k_{x_s}^{inc}/4$ and $\Delta k_{z_s}^{inc} = k_{z_s}^{inc}/4$.

The Hilbert transform method (detailed in section 2.2.2) recovers the outcome velocity field corresponding to the spatial filtering process. This spatial filtering centered in $k_{x_s}^{inc}$ and $k_{z_s}^{inc}$ permits to isolate the velocity field corresponding to the incident wave. We will call this velocity field $\text{HT}(\omega, k_{x_s}^{inc}, k_{z_s}^{inc})$, where HT denotes Hilbert transform (shown in figure 4.6(b)). Obtaining the reflected wave is less direct: in a first step, the velocity field is filtered around $k_{x_s}^{inc}$, which is a quantity conserved in the reflection. This field is named $\text{HT}(\omega, k_{x_s}^{inc})$ and is shown in figure 4.6(a); the second step consists in subtracting to this field $\text{HT}(\omega, k_{x_s}^{inc})$ the velocity field corresponding to the incident wave $\text{HT}(\omega, k_{x_s}^{inc}, k_{z_s}^{inc})$:

$$U_{HT}^{refl} = \text{HT}(\omega, k_{x_s}^{inc}) - \text{HT}(\omega, k_{x_s}^{inc}, k_{z_s}^{inc}), \quad (4.2)$$

where U_{HT}^{refl} is the velocity field associated to the reflected wave.

The filtering operation allows to extract the reflected wave U_{HT}^{refl} (figure 4.6(c)), which propagates from left to right in the neighborhood of the slope, in contrast with the incident wave, which propagates from up-left to down-right.

The Hilbert transform method can present some disadvantages to separate the incident and reflected wave. The outcome velocity field of the incident wave can present distortion of the amplitude on the sides of the image caused by boundary effects. This effect is produced by the fact that there is a finite number of wavelengths of the wave in the field of view. The artifact will be more pronounced when the ratio between wavelength and image size increases.

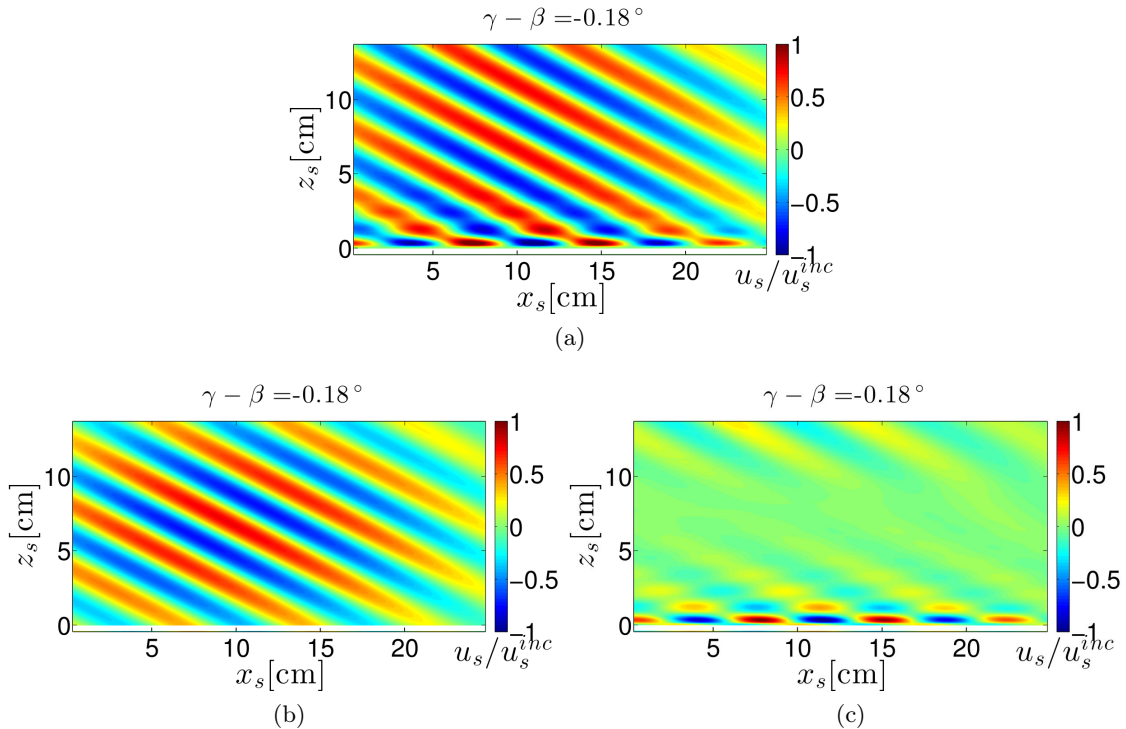


Figure 4.6: Snapshot of u_s/u_s^{inc} resulting from a filtering through Hilbert transform around: ω_0 and $k_{x_s}^{inc}$ (a); and around ω_0 , $k_{x_s}^{inc}$ and $k_{z_s}^{inc}$ (b). (c) Result of the subtraction between velocity field u_s of (a) and (b). Note that the slope boundary is located at $z_s = 0$.

It is intrinsic to the procedure of obtaining the reflected wave, that if the incident wave presents artifacts, the reflected wave will also do. We will now present a variational method that permits a more accurate separation between incident and reflected wave.

4.3.3 Variational mode decomposition method (VMD)

Another way that wave selection can be performed is through 2-D Variational Mode Decomposition [22]. This method consists in decomposing an image into different modes of separated spectral bands, which are unknown beforehand.

The 2-D Variational Mode Decomposition allows, instead of searching for a specific wave, to perform a selection that can be formulated as an inverse problem which consists in extracting J oscillating components (modes), denoted $(\mathbf{u}_j)_{1 \leq j \leq J}$ with $\mathbf{u}_j \in \mathbb{R}^{N_1 \times N_2}$, from the observed data \mathbf{u} , where $N_1 \times N_2$ is the spatial region of the field of view, say $\mathbf{u} \in \mathbb{R}^{N_1 \times N_2}$ such that

$$\mathbf{u} = \sum_{j=1}^J \mathbf{u}_j + \varepsilon \quad (4.3)$$

where ε models an additive noise which represents in our case how close the addition of the modes are to the input data. The study of internal wave reflection corresponds to the specific case $J = 2$ (in some specific cases we will use $J = 3$), where \mathbf{u} models the velocity field, and each component is centered around an unknown spatial frequency $\mathbf{k}_j = (k_{j,1}, k_{j,2})$ so that, for every location $(x_s, z_s) \in \{1, \dots, N_1\} \times \{1, \dots, N_2\}$,

$$u_{j,(x_s, z_s)} = a_{j,(x_s, z_s)} \cos(v_{j,1,(x_s, z_s)} x_s + v_{j,2,(x_s, z_s)} z_s + \varphi) \quad (4.4)$$

where $\mathbf{a}_j \in \mathbb{R}^{N_1 \times N_2}$ models the amplitude changes in space and, for $i \in \{1, 2\}$, the mean value over space of the spectral content $\mathbf{v}_{j,i} \in \mathbb{R}^{N_1 \times N_2}$ is close to the central value $\mathbf{k}_{j,i}$, and φ is a phase term.

The 2-D Variational Mode Decomposition aims at estimating jointly $(\mathbf{u}_j)_{1 \leq j \leq J}$ and $(\mathbf{k}_j)_{1 \leq j \leq J}$ by solving

$$\min_{(\mathbf{u}_j, \mathbf{k}_j)_{1 \leq j \leq J}} \left\{ \left\| \mathbf{u} - \sum_{j=1}^J \mathbf{u}_j \right\|^2 + \alpha^V \sum_{j=1}^J \left\| D \left(u_{j,(x_s, z_s)}^{AS} e^{-i(k_{j,1}x_s + k_{j,2}z_s)} \right)_{(x_s, z_s)} \right\|^2 \right\} \quad (4.5)$$

where the 2D analytic signal \mathbf{u}_j^{AS} is defined in the Fourier domain, for every spatial frequency $(\nu_1, \nu_2) \in \mathcal{V}$, as

$$\hat{u}_{j,(\nu_1, \nu_2)}^{AS} = (1 + \text{sign}(k_{j,1}\nu_1 + k_{j,2}\nu_2)) \hat{u}_{j,(\nu_1, \nu_2)}. \quad (4.6)$$

D models the gradient operator and the coefficient $\alpha^V > 0$ denotes a regularization parameter allowing to adjust the bandwidth size of the filter.

We have improved this algorithm considering the specific properties of internal wave reflections:

- first, incident and reflected wave have different spectral behaviors. In particular, the spectrum of the reflected wave is very compact horizontally but not vertically. Parameters α^V depending on the mode j and the coordinate $i \in \{1, 2\}$ have been introduced, in order to separately adjust the horizontal and vertical spectral compacity of each mode.
- Second, for the critical and near critical reflections, the reflected wave will stay in the proximity of the boundary. For this case we expect that the mode associated to the reflected wave will vanish far away from the slope. This information can be introduced through a penalty term $f_j(\mathbf{u}_j)$, which acts as an indicator function $i_C(\mathbf{u}_j)$ whose value is 0 if $\mathbf{u}_j \in C = \{\mathbf{u} \in \mathbb{R}^N | (\forall (x_s, z_s) \in \mathbb{S}) \quad u_{(x_s, z_s)} = 0\}$ and $+\infty$ otherwise. For such a choice of the penalty f_j , we impose the component \mathbf{u}_j to be zero in the set of indexes \mathbb{S} .

According to these remarks, the criteria derived to minimize is the following:

$$\min_{(\mathbf{u}_j, \mathbf{k}_j)_{1 \leq j \leq J}} \left\{ \sum_{j=1}^J f_j(\mathbf{u}_j) + \lambda^V \left\| \sum_{j=1}^J \mathbf{u}_j - \mathbf{u} \right\|^2 \right\} \quad (4.7)$$

$$+ \alpha_{j,1}^V \sum_{j=1}^J \left\| D_1 \left(u_{j,(x_s, z_s)}^{AS} e^{-ik_{j,1}x_s} \right)_{(x_s, z_s)} \right\|^2 \quad (4.8)$$

$$+ \alpha_{j,2}^V \sum_{j=1}^J \left\| D_2 \left(u_{j,(x_s, z_s)}^{AS} e^{-ik_{j,2}z_s} \right)_{(x_s, z_s)} \right\|^2 \quad (4.9)$$

where D_1 and D_2 denote respectively the gradient operator along the x_s and z_s component. The parameters $\alpha_{j,1}^V$ and $\alpha_{j,2}^V$ which allow to adjust the selectivity for each mode and component are chosen positive. The parameter λ^V permits to adjust the attachment of the decomposition to the data \mathbf{u}

A more extensive and detailed presentation of the 2-D Variational Mode Decomposition method improved for internal wave reflection has been published in Schmitt *et al* [61].

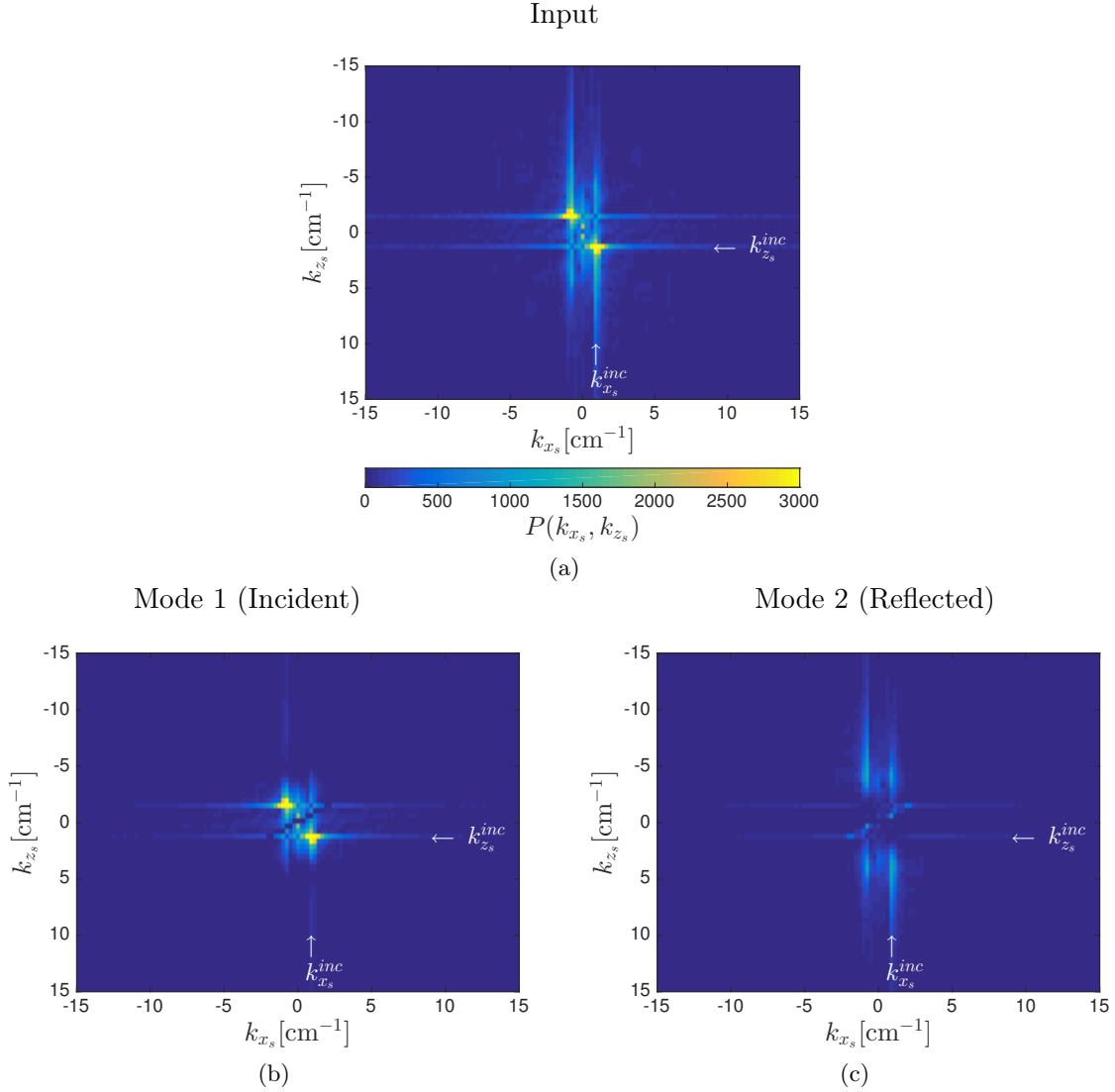


Figure 4.7: 2D spatial power spectrum $P(k_{x_s}, k_{z_s})$ of the velocity field corresponding to the experiment presented in figure 4.3. (a) Spectrum of a velocity field of incident and reflected wave together. (b) and (c) are Mode 1 and 2 obtained through 2D-VMD separation method associated to the velocity field of the incident and reflected wave respectively. $k_{x_s}^{inc}$ and $k_{z_s}^{inc}$ are indicated in the lower and right margin of each figure.

4.3.4 VMD spectral analysis

The particular behavior of an internal wave critical reflection distribution in space can be analogously described through the respective spatial spectrum of its components. First, the along-slope component of the wavenumber will be conserved, $k_{x_s}^{refl} = k_{x_s}^{inc}$. Second, it is expected that $k_{z_s}^{refl} > k_{z_s}^{inc}$. Finally, the reflected wave will be confined to a small section close to the slope, in consequence, $k_{z_s}^{refl}$ will be highly spread in the spatial spectrum.

Figure 4.7 shows the spatial spectrum of the incident and reflected wave after filtering in time around ω_0 (which we named Input), as well as the spatial spectrum corresponding to the incident (named Mode 1) and reflected wave (named Mode 2), separated through 2D-VMD method. The spectra corresponds to the experiment presented in figure 4.3.

The spatial spectrum for the velocity fields corresponding to both the incident and

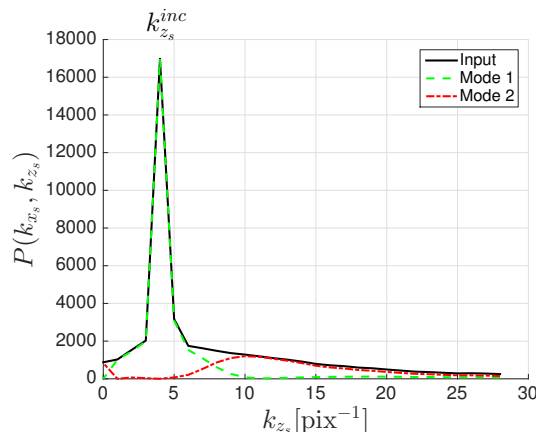


Figure 4.8: Profile along the k_{z_s} coordinate for $k_{x_s} = k_{x_s}^{inc}$ of the three spatial spectrum plotted in figure 4.7.

reflected waves (4.7(a)), and to the incident wave alone (4.7(b)) present their maximum value for the wavenumber matching the incident wave \mathbf{k}^{inc} . For the spectrum corresponding to the reflected wave (figure 4.7(c)) the maximum in the k_{x_s} coordinate is equal to $k_{x_s}^{inc}$; in contrast, the maximum corresponding to the k_{z_s} coordinate has a larger value and is not as well defined along the k_{z_s} coordinate. We can see that there is conservation of k_{x_s} in the reflection process.

By taking a vertical profile along the coordinate k_{z_s} of the spectra presented in 4.7, for the along-slope wavenumber $k_{x_s} = k_{x_s}^{inc}$, one can see the relative contributions that the Mode 1 and the Mode 2 have over the Input spectrum profile. This is shown in figure 4.8, the Mode 1 associated to the incident wave is well localized around $k_{x_s}^{inc}$ and has a larger magnitude $P(k_{x_s}^{inc}, k_{z_s})$ than the Mode 2 (reflected wave) which is located around a larger value of k_{z_s} and is more spread out.

The spectral shape of internal waves in a reflection process is fundamental at the moment of choosing the correct parameters for the spatial separation through the improved VMD method described in section 4.3.3. That is, as the reflected wave is more compact in the k_{x_s} coordinate than in the k_{z_s} , the parameters $\alpha_{j,2}^V$ that adjust the selectivity of the filter of the VMD method (equation (4.9)) in order to better perform the separation between incident and reflected wave, will not have the same value in both directions j .

4.3.5 HT vs VMD and improved VMD

In order to select the best method for the separation of the incident and reflected wave in a reflection process, the Hilbert transform and Variational Mode Decomposition methods are compared.

For the Hilbert transform the time evolution of the velocity field is needed in order to obtain the phase of the wave and correctly describe the wavenumber before the spatial filtering is done. In the case of the VMD methods only one image is required to perform the spatial decomposition operation, in this case, the velocity field is previously filtered in time at the forcing frequency ω_0 (figure 4.9(a)).

The VMD method will be used with various stages of refinement considering the improvements developed for the algorithm presented in section 4.3.3, that is, control the bandwidth selectivity for each mode, and perform a penalization in a particular spatial region. We will then consider the following stages:

- VMD: the separation method has the same bandwidth selectivity for the spatial frequency of each mode, as well as for the different coordinates, k_{x_s} and k_{z_s} , and no penalization is done to any values of the velocity field in the real space. This is, $\alpha_{j,\{1,2\}}^V = \alpha^V$ for $j = \{x_s, z_s\}$ and $f_j = 0$ in equation (4.9), which in this case becomes equation (4.5).
- VMD non-iso: the bandwidth selectivity for the spatial frequency $\alpha_{j,\{1,2\}}^V$ can be chosen independently for each mode and coordinate. No penalization is done, $f_j = 0$.
- VMD non-iso projection: the bandwidth selectivity for the spatial frequency $\alpha_{j,\{1,2\}}^V$ can be chosen independently for each mode and coordinate. A penalization to the reflected wave (Mode 2) is performed in order to have a null velocity field for a selected region of the real space (the upper half of the image).

The selection criteria to determine which method will be used is based on assuming that some physical properties should be satisfied in the reflection process. These physical properties are:

1. The amplitude of the incident wave barely changes in the region of the image.
2. The amplitude of the reflected wave is negligible far from the slope.
3. The complete velocity field is composed of the addition of the incident and reflected wave.

Following these remarks, the methods are compared. Figure 4.9 shows the velocity field decomposition of the incident and reflected wave for the experiment corresponding to the snapshot presented in 4.3 through the Hilbert transform and the VMD methods.

As expected for the Input image (figure 4.9(a)), the intensity of u_s decreases from left to right due to viscous dissipation. Nevertheless, in figure 4.9(b), the velocity field related to the incident wave obtained by the Hilbert transform method presents the largest intensity of u_s in the center of the image and not on the left side of the image. This is a hint that some boundary effects are present in the outcome of the filtering process through the Hilbert transform that are not present in the VMD methods (figure 4.9(d), (f), (h)). The VMD methods are able to capture the variation of the intensity of the wave given by dissipation, that is, the wave loses intensity as it moves away from the source. For the Hilbert transform method one notices that in the separation process, the incident wave is partially mixed up in the velocity field associated to the reflected wave (figure 4.9(c)). Less pronounced, in the VMD methods, the opposite happens: the reflected wave modifies the velocity field related to the incident wave (Mode 1) near the boundary. In the Mode 2 for VMD and VMD non-iso methods an artifact appears in the upper part of the image, which is not present in the VMD non-iso projection method.

In order to compare the different separation methods, it is also useful to take the absolute value of the velocity field $u_s(x_s, z_s)$ spatially averaged in the coordinate x_s as a function of z_s , that is, $\langle |u_s| \rangle_{x_s}$. These profiles are shown in figure 4.10 for all the separation methods presented here. From these profiles one can observe the dependence of the amplitude with z_s for the incident or reflected wave obtained through different methods. For the incident wave (Mode 1) the amplitude varies by almost 30% between the center and the boundaries of the image for the Hilbert transform method, whereas in VMD method this variation decreases to a 15%. For the reflected wave (Mode 2), the amplitude at the boundary seems to be overestimated for the Hilbert transform method.

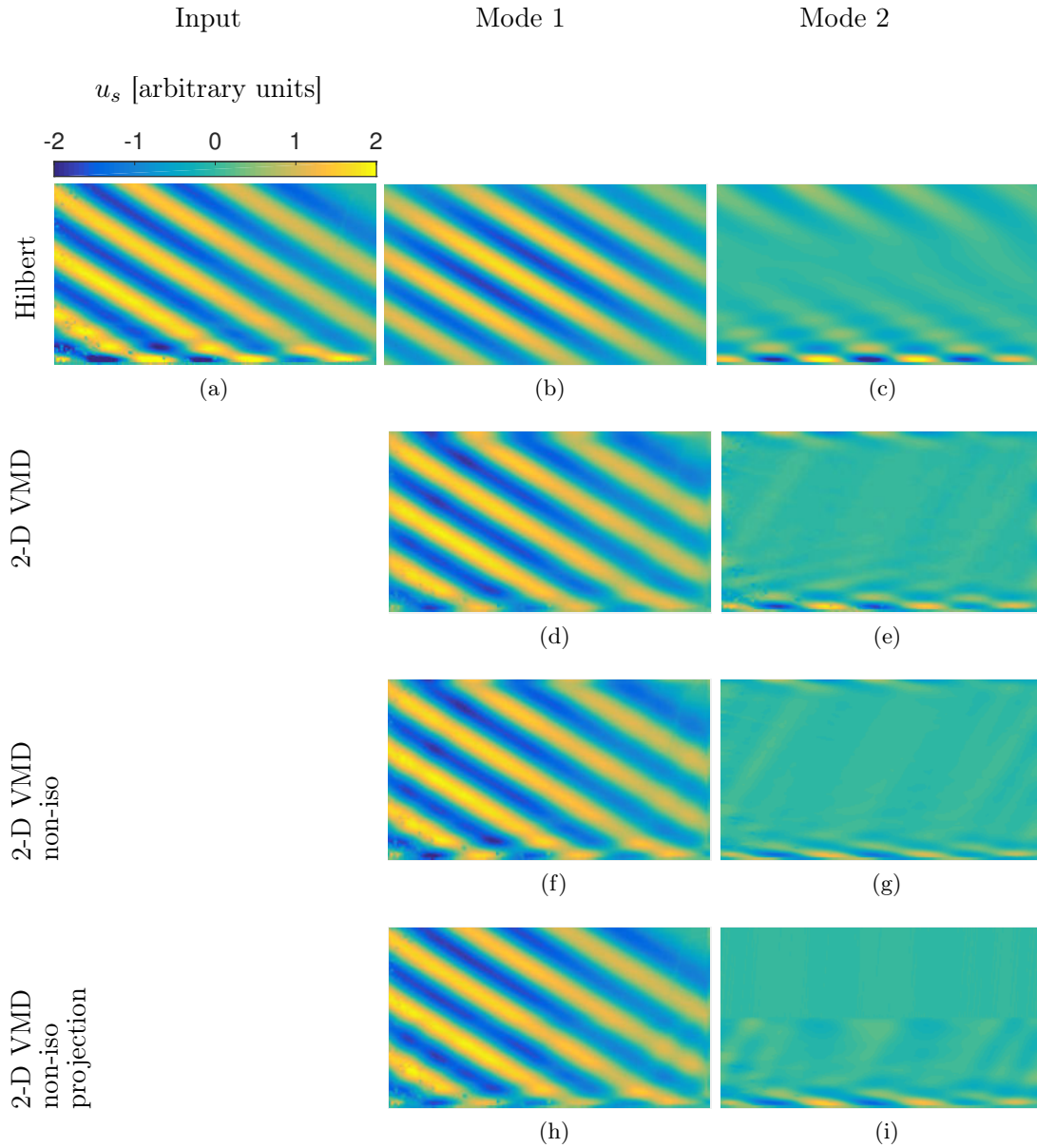


Figure 4.9: 2D images of the field of view for the experiment presented in figure 4.3. Abscissa and ordinate correspond respectively to the x_s and the z_s coordinates. Color scale indicates a scale proportional to u_s . (a) Velocity field filtered temporally at $\omega_0/N = 0.26$ that will be used as the input of the spatial separation methods. Figures (b), (d), (f) and (h) represent the Mode 1 (incident wave) obtained through respectively the Hilbert transform, VMD, VMD non-iso and VMD non-iso projection methods; whereas figures (c), (e), (g) and (i) represent the corresponding field for Mode 2 (reflected wave).

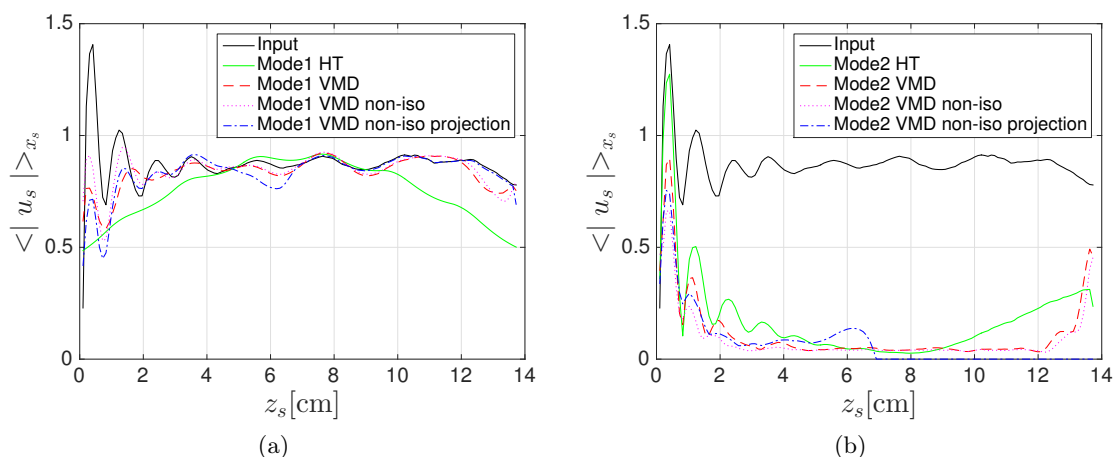


Figure 4.10: $\langle |u_s(z_s)| \rangle_{x_s}$ for different spatial separation methods. (a) velocity field related to the incident wave (Mode 1). (b) velocity field related to the reflected wave (Mode 2). In both figures is plotted the profile of the Input. $z_s = 0$ represents the position of the slope.

In the reflected wave for the VMD and VMD non-iso methods the artifact found in the upper part of the figures 4.9(e) and (g), can be observed for large values of z_s . While in the VMD non-iso projection method this artifact will not be present.

Taking into account the requirements that are expected for the separation methods, one can summarize the comparison by the following remarks:

- The mode decomposition in the HT method is completely attached to the input, that is intrinsic to the separation process of the modes. In consequence, the Mode 2 will present boundary effects, because the Mode 1 presents boundary effects.
- The VMD methods allows to reduce the oscillations of the Mode 1 on the first 30 pixels near the slope.
- Adding the directionality constraint allows to be less sensitive to the choices of the optimal method parameters.
- The zero-constraint on the Mode 2 for the pixels that are far from the slope enables to cancel the undesired oscillations of the incident wave and the boundary effects in the reflected wave.

The attachment to data is fairly similar in all methods (the value of ε of equation 4.3). It has been taken into account in the optimal selection of the parameters of each method.

In view of the physical remarks pointed out for the separation of incident and reflected wave in the reflection process, the method that highlights best these features is the VMD method. In further analysis we shall use the VMD non-iso projection to separate the incident and reflected wave. For non-critical reflections the VMD non-iso method will be also used, given that the reflected wave will not remain close to the slope.

4.3.6 Extraction of the incident velocity

In order to study the enhancement of the shear stress when focusing occurs, we will relate the intensity of the reflected wave to the intensity of the incident wave. To measure this

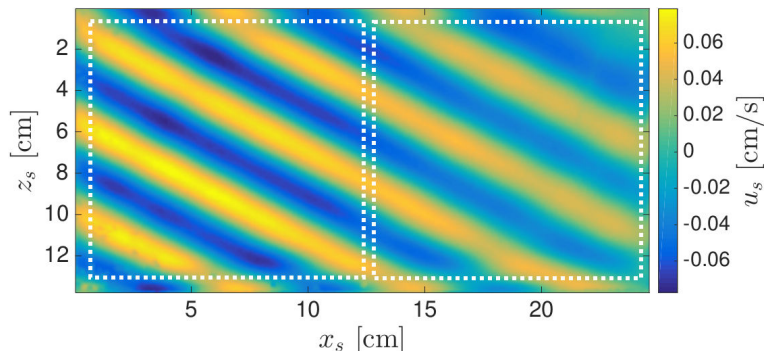


Figure 4.11: Wavefield associated to the incident velocity obtained through VMD decomposition of "exp3". With a white square is marked the regions in which the incident velocity is averaged.

relation it is useful to extract a value for the intensity of the incident wavefield velocity. This is performed by using the mode associated to the incident wave.

The method used to obtain a value which represents the intensity of the incident velocity is based on considering that the wavefield has the form of a sinusoidal along both x_s and z_s coordinates, that is, $u_s = u_s^{inc} \sin(k_{x_s} x_s + k_{z_s} z_s + \phi)$, for example for the along-slope component of the velocity (this is not completely true given that the wave is dissipated, however, we estimated the systematic error related to this effect). Now, taking $|u_s(x_s, z_s)|$ and averaging this quantity in space, over a region of size $\lambda_{x_s} \times \lambda_{z_s}$, which are the wavelengths associated to the wavenumbers k_{x_s} and k_{z_s} , one can see that $\langle |u_s| \rangle_{\lambda_{x_s} \times \lambda_{z_s}} = \frac{2}{\pi} u_s^{inc}$, from where we can obtain u_s^{inc} .

This technique has been implemented by averaging $|u_s(x_s, z_s)|$ in the region of the left side of the field of view of the mode associated to the incident velocity (marked with a white square on the left side of the wavefield of figure 4.11). Only the wavefield of the left side of the field of view is used, so that the variations in the intensity because of dissipation are small enough to be neglected. It is important to mention that when averaging over a region $L_{x_s} \times L_{z_s}$, where $L_{x_s} > \lambda_{x_s}$ and $L_{z_s} > \lambda_{z_s}$ (which is our case), the difference in calculating $\langle |u_s| \rangle_{\lambda_{x_s} \times \lambda_{z_s}}$ and $\langle |u_s| \rangle_{L_{x_s} \times L_{z_s}}$ is smaller than 2%.

The reflected wave will propagate upward and/or downward depending on the value of $\beta - \gamma$. For this reason, the intensity of the reflected wave will sometimes be associated to the intensity of the incident wave in the region on the left of the field of view and sometimes to the region on the right. For a given experiment we will consider that the error in estimating the incident velocity, Δu_s^{inc} , will be associated to the difference between obtaining u_s^{inc} by averaging the right side of the field of view, $u_R^{inc} = \langle |u_s| \rangle_{Right}$, and the left side, $u_L^{inc} = \langle |u_s| \rangle_{Left}$ (the Left and Right regions of the field of view are shown in figure 4.11 with a white square at the left and at the right respectively). The systematic error associated to the dissipation of the incident wave in the region of the field of view will then be $\Delta u_s^{inc} = |u_R^{inc} - u_L^{inc}|$.

The separation of the waves involved in a near-critical reflection process, obtained through high resolution measurements, allows us to compare these results with Dauxois-Young theory for near-critical reflections. This theory emphasizes the fact that weak nonlinearities and viscosity will be determinant in the reflection process.

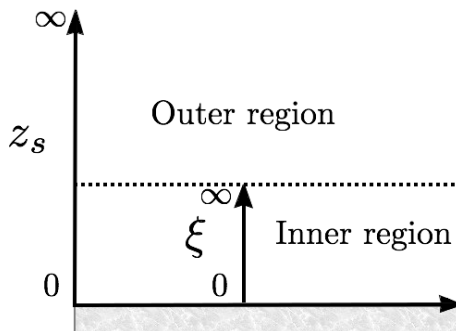


Figure 4.12: Schematics showing the definition of the two regions in the direction normal to the slope. The inner region near the slope is described by the coordinate ξ ; and the outer region described by z_s .

4.4 Weakly non-linear near critical reflection: Dauxois Young model

The model for internal wave reflections proposed by Phillips [57] presents fundamental problems to describe a critical reflection. A more accurate representation of the near-critical reflection has been developed by Dauxois & Young [19]. The theory is based on separating in two regions the space where the reflection occurs. The incident wave is in the outer region and the reflected disturbance is largely confined to an inner region, which is essentially a boundary layer close to the slope. Both regions are connected by an asymptotic matching condition. This separation is shown in the schematics of figure 4.12. The solution in the inner region is obtained by regular perturbation expansion.

In the following we will expose the key ingredients of this theoretical approach.

4.4.1 Dimensional analysis

We consider a two-dimensional, non-rotating, incompressible Boussinesq fluid, with constant Brunt-Väisälä frequency N . Taking an incident wave train, for which the streamfunction has the form:

$$\psi = A \cos(K \sin \alpha x + K \cos \alpha z - N \sin \beta t), \quad (4.10)$$

where the wavenumber K has been introduced. Considering this incident wave, we introduce the following dimensionless variables,

$$[\hat{x}_s, \hat{z}_s] = K[\sin \alpha x_s, \cos \alpha z_s], \quad (4.11)$$

$$\hat{t} = N \sin \beta t, \quad (4.12)$$

$$[\psi, u_s, w_s, b, p] = \psi_{max}[\hat{\psi}, K \cos \alpha \hat{u}_s, K \sin \alpha \hat{w}_s, KN \hat{b}_s, N \hat{p}]. \quad (4.13)$$

where $A = \psi_{max} \hat{A}$, and ψ_{max} is defined as the maximum amplitude of the streamfunction, so that $\max(\hat{A}) = 1$, $b(x, z, t)$ is the buoyancy perturbation of the stratification at rest and p the pressure.

The equations of motion for the dimensionless variables in the coordinate system attached to the slope are

$$\frac{D\hat{u}_s}{D\hat{t}} + \frac{\tan(\alpha)}{\sin \beta} \hat{p}_{\hat{x}_s} - \frac{\sin(\gamma)}{\sin \beta \cos \alpha} \hat{b}_s = \frac{1}{Re} \nabla^2 \hat{u}_s, \quad (4.14)$$

$$\frac{D\hat{w}_s}{D\hat{t}} + \frac{\cot(\alpha)}{\sin\beta}\hat{p}_{\hat{z}_s} - \frac{\cos(\gamma)}{\sin\beta\sin\alpha}\hat{b}_s = \frac{1}{Re}\nabla^2\hat{w}_s, \quad (4.15)$$

$$\frac{D\hat{b}_s}{D\hat{t}} + \frac{\cos(\alpha)\sin\gamma}{\sin\beta}\hat{u}_s - \frac{\cos(\gamma)\sin\alpha}{\sin\beta}\hat{w}_s = \frac{1}{Pe}\nabla^2\hat{b}_s, \quad (4.16)$$

$$\partial_{\hat{x}_s}\hat{u}_s + \partial_{\hat{z}_s}\hat{w}_s = 0. \quad (4.17)$$

And the boundary conditions at the slope will be,

$$N^2\cos\gamma + \partial_{\hat{z}_s}\hat{b} \quad \text{no-diffusive flux of buoyancy condition,} \quad (4.18)$$

$$\hat{u}_s = 0 \quad \text{no-slip condition,} \quad (4.19)$$

$$\hat{w}_s = 0 \quad \text{no-flux condition.} \quad (4.20)$$

Where the laplacian and time derivative operators are written as

$$\nabla^2 = \sin^2(\alpha)\partial_{\hat{x}_s}^2 + \cos^2(\alpha)\partial_{\hat{z}_s}^2, \quad (4.21)$$

$$\frac{D}{D\hat{t}} = \partial_{\hat{t}} + a(\hat{u}_s\partial_{\hat{x}_s} + \hat{w}_s\partial_{\hat{z}_s}). \quad (4.22)$$

The Reynolds and Peclet numbers are defined as:

$$Re = \frac{N\sin\beta}{\nu K^2}, \quad Pe = \frac{N\sin\beta}{\kappa K^2}. \quad (4.23)$$

A measure of the nonlinearities of the wave is defined by the parameter a :

$$a = \frac{K^2\sin 2\alpha}{2N\sin\beta}\psi_{max}. \quad (4.24)$$

In this non-dimensional and slope oriented coordinate system, the dispersion relation for an inviscid internal plane wave is,

$$\omega = \pm \frac{k_{\hat{x}_s}\sin\alpha\cos\gamma - k_{\hat{z}_s}\cos\alpha\sin\gamma}{\sin\beta\sqrt{(k_{\hat{x}_s}\sin\alpha)^2 + (k_{\hat{z}_s}\cos\alpha)^2}}, \quad (4.25)$$

and the wave solution that satisfies the dispersion relation is:

$$[\hat{\psi}, \hat{b}] = [1, 1]\frac{A}{2}e^{i(\hat{x}_s + \hat{z}_s - t)} + c.c. \quad (4.26)$$

Where the streamfunction is defined by the convention

$$\hat{u}_s = -\hat{\psi}_{\hat{z}_s}, \quad \hat{w}_s = \hat{\psi}_{\hat{x}_s}. \quad (4.27)$$

In what follows, the hats in the dimensionless variables will be dropped for simplicity.

4.4.2 Near critical approximation

The streamfunction solution (4.26) is of the same type of solution presented in section 1.1.4. In order to heal the singularity that this solution presents, a reductive approximation is developed based on taking a particular limit in which a , $\beta - \gamma$, Re^{-1} and Pe^{-1} are all small.

In terms of non-dimensional variables, the vertical wavenumber of the reflected wave is:

$$k_{z_s}^{refl} = \frac{\tan(\gamma + \beta)}{\tan(\gamma - \beta)}. \quad (4.28)$$

When the reflection is critical ($\gamma = \beta$) one can observe that $k_{z_s}^{refl} \rightarrow \infty$. The parameter ϵ is defined,

$$\epsilon = (a \tan \alpha)^{1/3}, \quad (4.29)$$

which is related, through a , to the relative weight of the non linearities. The reduction is based on the assumption that ϵ is small. We introduce δ :

$$\delta = \frac{\beta - \gamma}{\epsilon^2}, \quad (4.30)$$

so that

$$\gamma = \alpha/2 - \delta\epsilon^2/2, \quad \beta = \alpha/2 + \delta\epsilon^2/2. \quad (4.31)$$

And for $\epsilon \ll 1$, we have

$$k_{z_s}^{refl} \approx \frac{\tan(\alpha)}{\delta\epsilon^2}, \quad (4.32)$$

and

$$c_g \approx \frac{\tan(2\beta)}{(k_{z_s}^{refl})^2 \tan \beta} [-k_{z_s}^{refl}, 1]. \quad (4.33)$$

4.4.3 Inner region

The theory resolves the velocity field of an internal wave near-critical reflection by separating the space in two regions in the direction normal to the slope as shown in figure 4.12: the *outer region* where the incident wave is located; and the *inner region* where the reflected wave is confined.

In order to describe the reflected disturbance in the inner region a stretched coordinate ξ and a slow timescale t_2 are used, these scales are:

$$\xi \equiv \epsilon^{-2} \tan \alpha z_s, \quad t_2 \equiv \chi \epsilon^2 t, \quad (4.34)$$

where $\chi \equiv \cot(\alpha/2)$. We also define:

$$u_s \equiv \epsilon^{-2} \tan \alpha U, \quad w_s \equiv W, \quad \psi \equiv \Psi, \quad (4.35)$$

so that we have

$$U = -\Psi_\xi, \quad W = \Psi_{x_s}. \quad (4.36)$$

By solving the equations of motion for these stretched coordinates, Dauxois et Young derived a solution in terms of a regular perturbation expansion in ϵ (for more details see [19]). The leading-order solution for the streamfunction is

$$\Psi_0 = \frac{1}{2} e^{i(t-x_s)} \mathcal{S}(\xi, t_2) + c.c., \quad (4.37)$$

where \mathcal{S} will depend on the physical case considered (viscous/non viscous, critical/non critical, transient/steady).

Many cases are considered in this model, we will be interested in the stationary solution. For the viscous case, the steady solution for the reflected wave in a critical reflection $\delta = 0$ is:

$$\mathcal{S} = -\frac{2}{\sqrt{3}} \sin\left(\frac{\sqrt{3}\xi}{2\rho^{2/3}} + \pi/3\right) e^{-\xi/2\rho^{2/3}}, \quad (4.38)$$

where

$$\rho^2 = \frac{K^2 \sin^2 \alpha}{\epsilon^6 2\chi N \sin \beta} (\nu + \kappa). \quad (4.39)$$

By using equations (4.36), (4.37) and (4.38), we can obtain the along-slope velocity in the stretched coordinates of the reflected wave:

$$U = -\frac{e^{-\xi/2\rho^{2/3}}}{\sqrt{3}\rho^{2/3}} \left(\sin\left(\frac{\sqrt{3}\xi}{2\rho^{2/3}} + \pi/3\right) - \sqrt{3} \cos\left(\frac{\sqrt{3}\xi}{2\rho^{2/3}} + \pi/3\right) \right) \cos(x_s - t). \quad (4.40)$$

This solution will be compared with our high resolution measurements of the velocity field close to the slope, in section 4.5.

4.5 Results

4.5.1 Critical reflection: upward wave, downward wave or both?

As mentioned in section 4.3.5, the separation of the modes associated to the incident and reflected waves is done with the VMD method. This method allows to perform a mode decomposition in as many modes as one wants.

When $|\beta - \gamma|$ is large, the reflected wave reflects away from the boundary allowing the observation of the wave in a large region of the field of view, which permits an easy identification of this wave. On the other hand, when the reflection is near-critical, the wave focuses in a thin layer close to the boundary. As mentioned in section 1.1.4, when $\beta - \gamma \lesssim 0$ the direction of propagation of the reflected wave will be downward along the slope, whereas, it will be upward when $\beta - \gamma \gtrsim 0$. When $\beta - \gamma \approx 0$, both waves occur, upward and downward. For a near critical reflection, when decomposing the wavefield in three modes through VMD method we can observe that, in addition to the incident wave, the upward and downward reflected waves come into view (an example of these two waves is shown in figure 4.13). This decomposition is possible given that the propagation of these waves are in different directions, and therefore, have different associated wavenumber. In the cases where upward and downward reflected waves exist, we will consider that the full reflected wave is formed by the superposition of upward and downward waves.

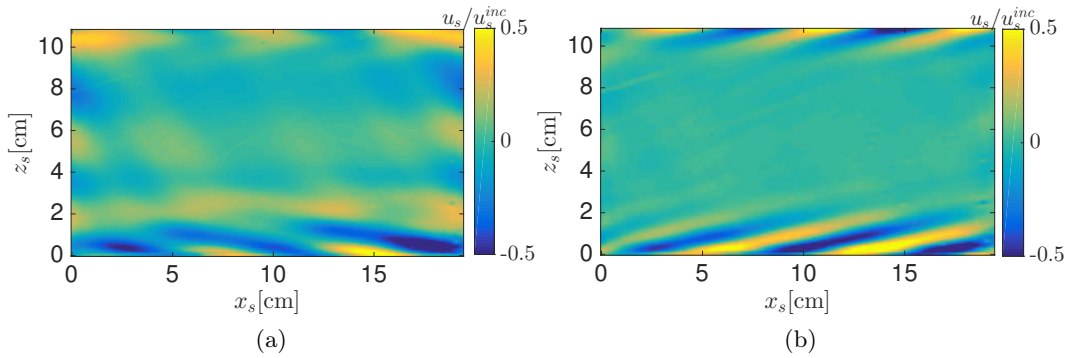


Figure 4.13: Normalized velocity field of experiment "exp4" corresponding to the downward (a) and the upward mode (b) of the reflected wave obtained through three-mode VMD decomposition. For this experiment $\beta - \gamma = -0.7^\circ$.

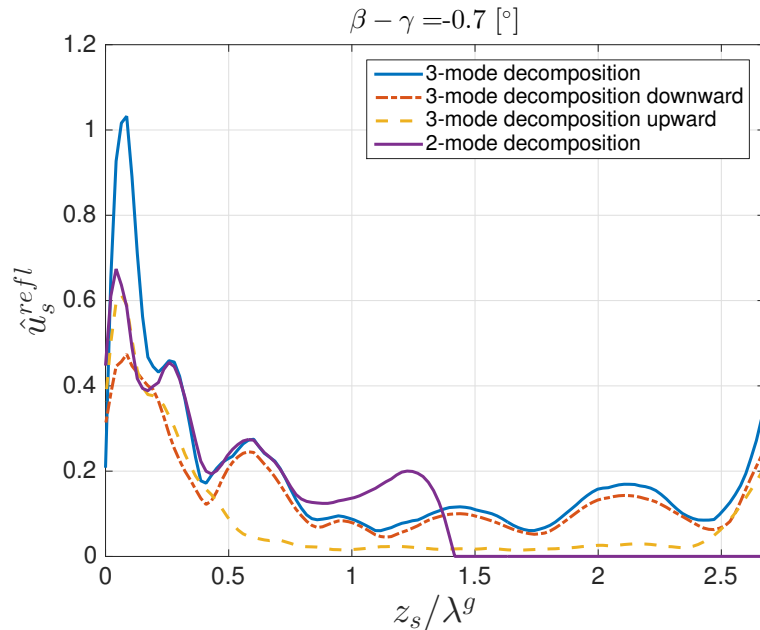


Figure 4.14: \hat{u}_s^{refl} as a function of z_s/λ^g estimated by two- and three-mode VMD decomposition, corresponding to experiment "exp4" and $\beta - \gamma = -0.7^\circ$. The upward and downward components of the three-mode VMD decomposition are also indicated.

The convergence time of the VMD method towards a steady solution will depend, between other things, on the number of modes employed in the decomposition. The convergence to a solution by using three-mode decomposition will not only take longer, but in some cases will not be possible. In particular, if we make use of the improved algorithm property which forces a mode to have a null velocity field in a particular spatial region (detailed in section 4.3.3), it is rare to converge to a solution when performing the decomposition with three modes.

We are interested in the dependency of the along-slope component of the velocity with respect to the coordinate normal to the slope, that is, u_s^{refl} as a function of z_s . Depending on the experimental parameters, the intensity of the incident wave will vary. In order to compare results from different experiments, we will measure the amplification of the reflected wave. For this, we introduce the useful quantity

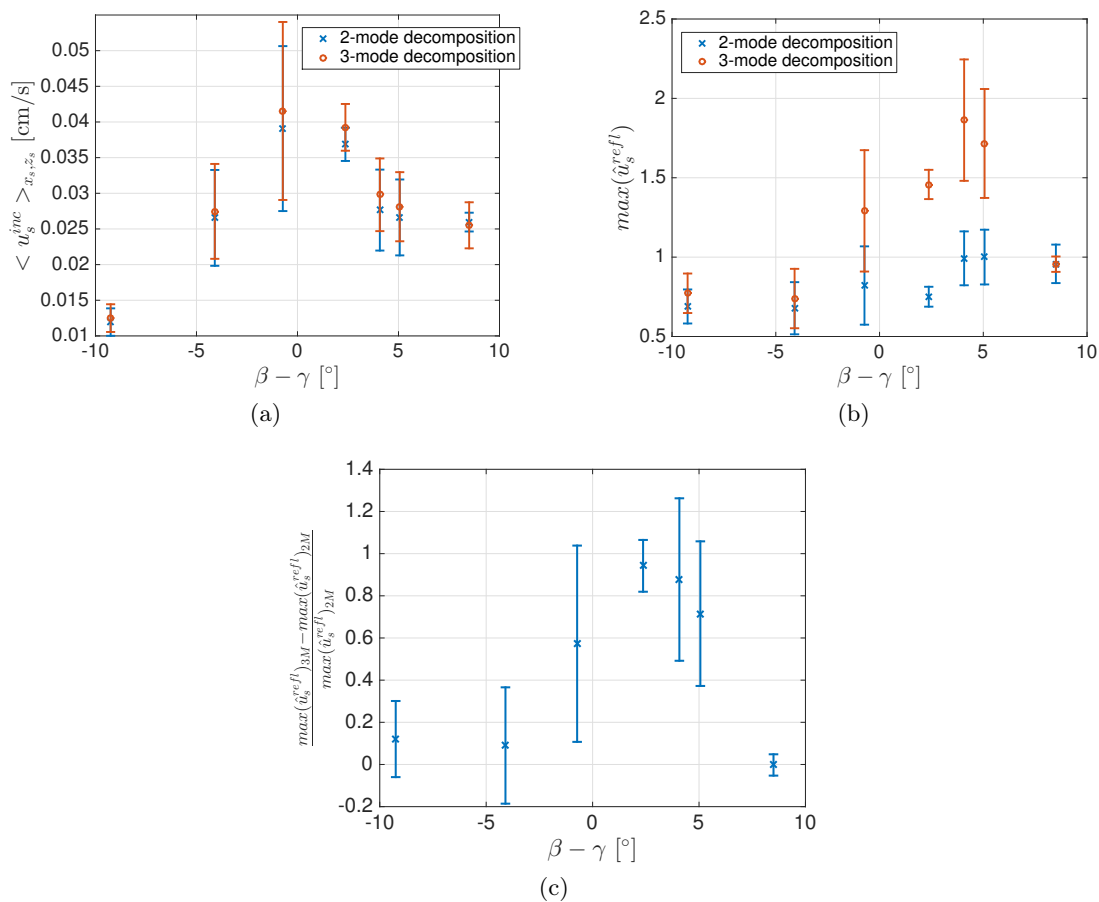


Figure 4.15: (a) u_s^{inc} as a function of $\beta - \gamma$ for two- and three-mode decomposition (b) $\max(\hat{u}_s^{refl})$ as a function of $\beta - \gamma$ for two- and three-mode VMD decomposition. (c) Normalized difference for $\max(\hat{u}_s^{refl})$ between two- and three-mode decomposition.

$$\hat{u}_s = \frac{\langle |u_s| \rangle_{x_s}}{u_s^{inc}}, \quad (4.41)$$

where u_s^{inc} is the value which represents the intensity of the incident wave velocity (the procedure to obtain this value is described in detailed in section 4.3.6). In order to extract the dependency in the z_s coordinate, we perform the average in the x_s coordinate over the same length as used for obtaining u_s^{inc} . The quantity \hat{u}_s allows to observe how the along-slope velocity varies with respect to the distance from the slope where the reflection occurs. In particular, we will study this quantity related to the reflected wave alone, named \hat{u}_s^{refl} .

In figure 4.14 is shown the profile \hat{u}_s^{refl} as a function of z_s/λ^g corresponding to the most critical reflection of "exp4", where λ^g is the vertical wavelength of the generator. The various profiles correspond to the reflected wave obtained by two- and three-mode VMD decomposition, and in the case of two-mode decomposition the mode associated to the reflected wave is forced to be null far from the slope. In dotted-dashed and dashed lines are indicated the profiles corresponding to the downward and upward components of the reflected wave obtained through three-mode VMD decomposition. One can observe that the intensity near the boundary ($z_s = 0$) of the reflected wave obtained through two modes

is comparable to the upward and downward components. This is an indicator that when both upward and downward components are present, it is necessary to use three modes to describe properly the reflected wave. This result can be explained by the fact that the two-mode decomposition selects the upward or downward components of the reflected wave only. The differences between two- and three-mode decompositions is amplified for the largest values of \hat{u}_s^{refl} . Figure 4.14 shows the difference of the largest value of \hat{u}_s^{refl} , between two- and three-mode decompositions for a particular value $\beta - \gamma$. In order to better compare two- and three-mode decompositions for different values of $\beta - \gamma$, we use the maximum value of the profile $\hat{u}_s^{refl}(z_s)$ as an indicator of how well the reflected wave is extracted from the full wavefield. The incident velocity obtained through two- and three-mode decompositions present differences not larger than 5% as can be observed in figure 4.15(a) for experiment "exp4", where u_s^{inc} is plotted as a function of $\beta - \gamma$. In figure 4.15(b) is shown $\max(\hat{u}_s^{refl})$ as a function of $\beta - \gamma$ for the experiment "exp4". One can observe that the value of $\max(\hat{u}_s^{refl})$ for the two-mode decomposition does not change much for different values of $\beta - \gamma$. On the other hand, the three-mode decomposition presents larger values of $\max(\hat{u}_s^{refl})$ for $0^\circ \lesssim \beta - \gamma \lesssim 5^\circ$. The normalized difference of $\max(\hat{u}_s^{refl})$ obtained through the two- and three-mode decomposition as a function of $\beta - \gamma$ can be observed in figure 4.15(c). Even though the error bars are large, one can see that for large values of $|\beta - \gamma|$ the difference in obtaining $\max(\hat{u}_s^{refl})$ through two- and three-mode decompositions is small. On the other hand, these differences increase for $0^\circ \lesssim \beta - \gamma \lesssim 5^\circ$.

The difference in using two- or three-mode decompositions is increased for values of $\beta - \gamma$ for which the reflection is near-critical and upward and downward components of the reflected wave exist simultaneously. This effect can be understood through the solution for critical reflections presented in equation (4.40). The oscillation term of this solution presents the form, $\cos(z_s) \cos(x_s - t)$, that can be decomposed in the form, $\frac{1}{2}(\cos(x_s - t + z_s) + \cos(x_s - t - z_s))$, which are two waves propagating upward and downward.

In summary, the three-mode decomposition resolves more accurately the wavefield of the reflected wave near the sloped boundary than the two-mode decomposition when three waves are present, yet introduces boundary effects for large values of z_s , since the algorithm cannot be used to penalized (in our case the penalization will be to force the mode to have a null velocity field) the wavefield of a mode in a region of the field of view for the three-mode decomposition. We will then make use of the three-mode decomposition when three waves are present in the reflection (for reflections in the interval $0^\circ \lesssim \beta - \gamma \lesssim 5^\circ$ for "exp4"), and the two-mode decomposition when two waves are present in the reflection with the possibility of applying the property of the improved algorithm to penalize the velocity field in a region of space.

4.5.2 Intensity of the reflected wave

As already remarked we are interested in the intensity of the velocity field of the reflected wave near the slope for reflections that are near critical, that is, reflections for which $\beta - \gamma \approx 0$. Nevertheless, in order to understand the behavior of near-critical reflections, we have explored a wider range of values centered on $\beta - \gamma = 0$, from -15° to 15° .

In figure 4.16 is shown $\max(\hat{u}_s^{refl})$ as a function of $\beta - \gamma$ for experiments with different sets of the experimental parameters, A and λ^g , the amplitude and vertical wavelength of the wave generator respectively. One can see that the value of $\max(\hat{u}_s^{refl})$ presents variations in the range of angles $-10^\circ \lesssim \beta - \gamma \lesssim 15^\circ$, of not more than 50% within each experiment, which in some cases, represents the same magnitude as the uncertainty. The uncertainty of $\max(\hat{u}_s^{refl})$ for each experiment will depend on the uncertainty in estimating

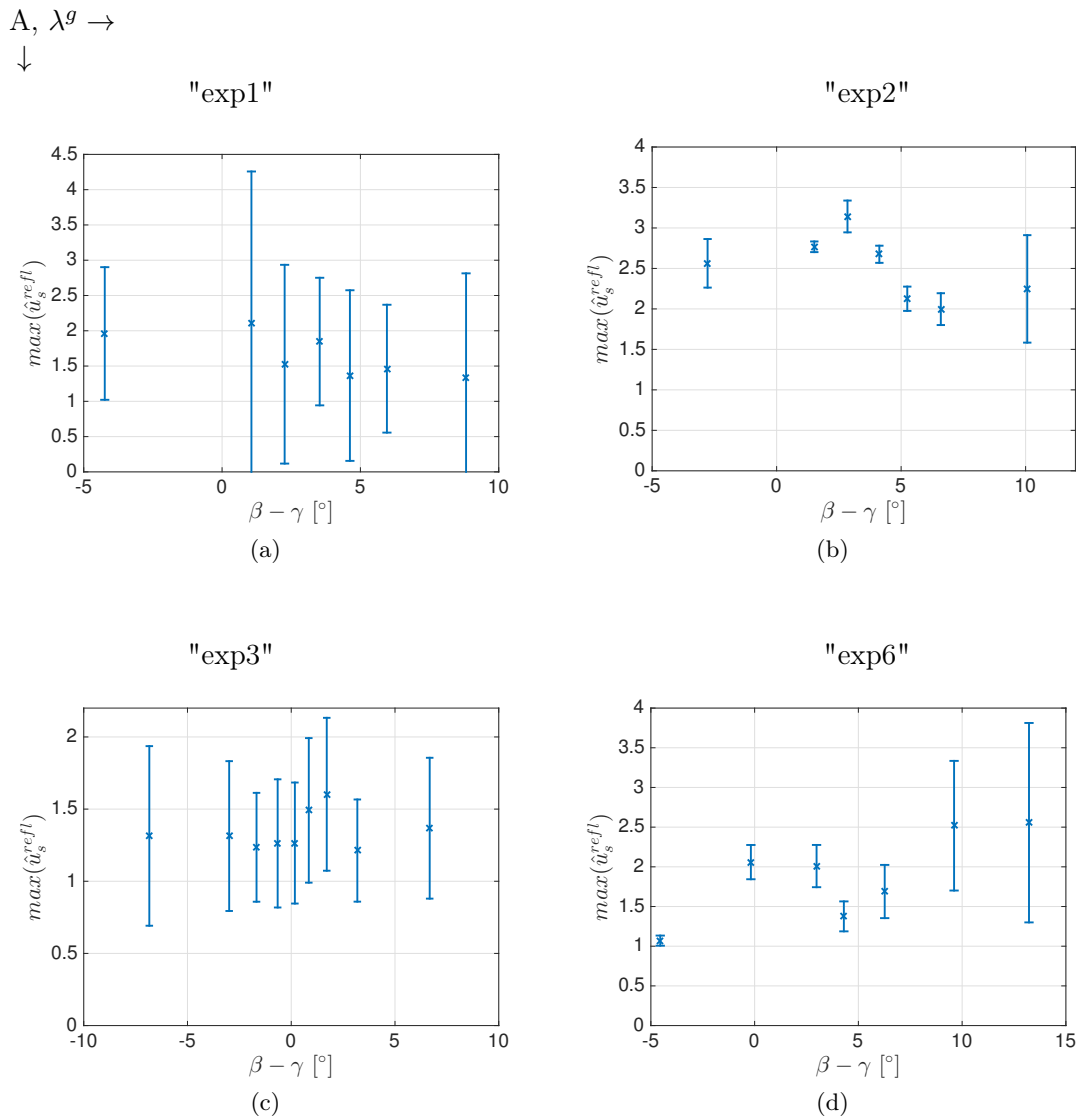


Figure 4.16: $\max(\hat{u}_s^{refl})$ as a function of $\beta - \gamma$ for experiments (ordered by increasing Re number): (a) "exp1", (b) "exp2", (c) "exp3" and (d) "exp6". The experiments present different sets of parameters A and λ^g , and at the top left is indicated in which direction these two parameters increase.

u_s^{inc} . And the uncertainty in u_s^{inc} will depend on how dissipation affects the incident wave in the field of view (as described in detail in section 4.3.6). The uncertainty in $\max(\hat{u}_s^{refl})$ will be usually smaller for experiments in which the wavelength λ^g is large, as dissipation will have a larger effect over waves with small wavenumber. The higher amplification of the reflected wave is found in experiment "exp2", which corresponds to the experiment with smaller amplitude $A = 0.25$ cm, and larger wavelength $\lambda^g = 8$ cm, for the wave generator. For this experiment, the largest value of $\max(\hat{u}_s^{refl})$ is slightly above 3 and it corresponds to a value of $\beta - \gamma \approx 3^\circ$ which is not the most critical value explored in this experiment.

An increase of $\max(\hat{u}_s^{refl})$ for small and positive values of $\beta - \gamma$ (as for example "exp2" and "exp4" in figures 4.16(b) and 4.15(a) respectively) has been observed in several experiments. However, in other experiments the uncertainty in estimating $\max(\hat{u}_s^{refl})$ does not allow to interpret an increase of this value in an interval of $\beta - \gamma$ (as for example "exp1"

and "exp3" in figures 4.16(a) and 4.16(c) respectively).

In contrast with what is observed in our experiments, in the linear theory of internal waves reflection, the maximum amplification of the reflected wave is expected to occur at the critical angle $\beta - \gamma = 0$. Dauxois & Young proposed solutions for critical and non critical reflections, in the non viscous case, as well as in the viscous case but only for critical angle. For this reason, we cannot compare the evolution of $\max(\hat{u}_s^{refl})$ as a function of $\beta - \gamma$ which for our experiment is both non critical and viscous. Nevertheless, we will compare the Dauxois & Young solution for critical-viscous reflections (smallest $|\beta - \gamma|$) with our most critical reflections of the experiments performed.

4.5.3 Dauxois & Young model: comparison with experiments

In order to compare the solution developed by Dauxois & Young for critical and viscous reflections, with our measurements we will again use \hat{u}_s^{refl} . This quantity allows to see how the reflected wave varies as a function of z_s/λ^g , and will be compared with the average in t and in x_s of the solution presented in equation (4.40). By performing these averages, the dependency on t and x_s disappears, and in return a $2/\pi$ multiplicative factor is taken into account.

Figure 4.17 shows the profile of \hat{u}_s^{refl} as a function of z_s/λ^g for the most critical reflections performed in experiments "exp1", "exp2", "exp3" and "exp6". In addition, is plotted the profile of \hat{u}_s^{refl} expected by Dauxois & Young theory. For the range of experimental parameters explored in this work, the theory predicts a profile that presents several peaks with decreasing amplitude away from the boundary, and practically vanishing after the third peak. In the case of the profile obtained through experiments, these peaks can also be found. Starting from the slope boundary ($z_s/\lambda^g = 0$), the first two peaks are well identified, and the third is usually lost. For higher values of z_s/λ^g the experimental profile decreases to lower amplitude values, and in the farther region of the field of view the profile amplitude increases because of boundary effects. The effect at the boundary of the field of view far from the slope is a consequence of the impossibility of using the three-mode VMD method and force a particular mode to have a null wavefield in a determined section of space (described in section 4.5.1). The amplitude of the first peak that the theory predicts is of the same magnitude (as for example, "exp1" and "exp2" in figures 4.17(a) and (b) respectively) or larger ("exp3" and "exp6" in figures 4.17(c) and (d) respectively) than the amplitude of the peak obtained experimentally. Nevertheless, the width of the first peak, in z_s/λ^g coordinates, is usually well predicted by the theory. On the other hand, the amplitude of the second peak is always underestimated by the theory with respect to the experimental measurements. Even though the difference is not very large, the width of the second peak is also underestimated by the theory.

The theory developed by Dauxois & Young predicts qualitatively well the velocity profile \hat{u}_s^{refl} as a function of z_s/λ^g for the reflected wave in a critical reflection. The theory manifests the two peaks observed in the experiments near the slope, with a similar width for each of these peaks. The amplitude of the first peak is usually overestimated by the theory (up to a 50% larger than the experimental value), this effect may be due to the fact that experimentally we have incertitude in the angles $\beta(N, \omega)$ and γ , that does not allow us to be sure of being in the case $\beta - \gamma = 0$, as expected for the solution predicted by the theory.

The implementation of these experiments required the control of many sensible experimental parameters. These measurements allowed for the first time to perform a comparison of the velocity field close to the slope in an internal near-critical wave reflection with the theory proposed by Dauxois & Young. In particular, we obtained a precise profile in the

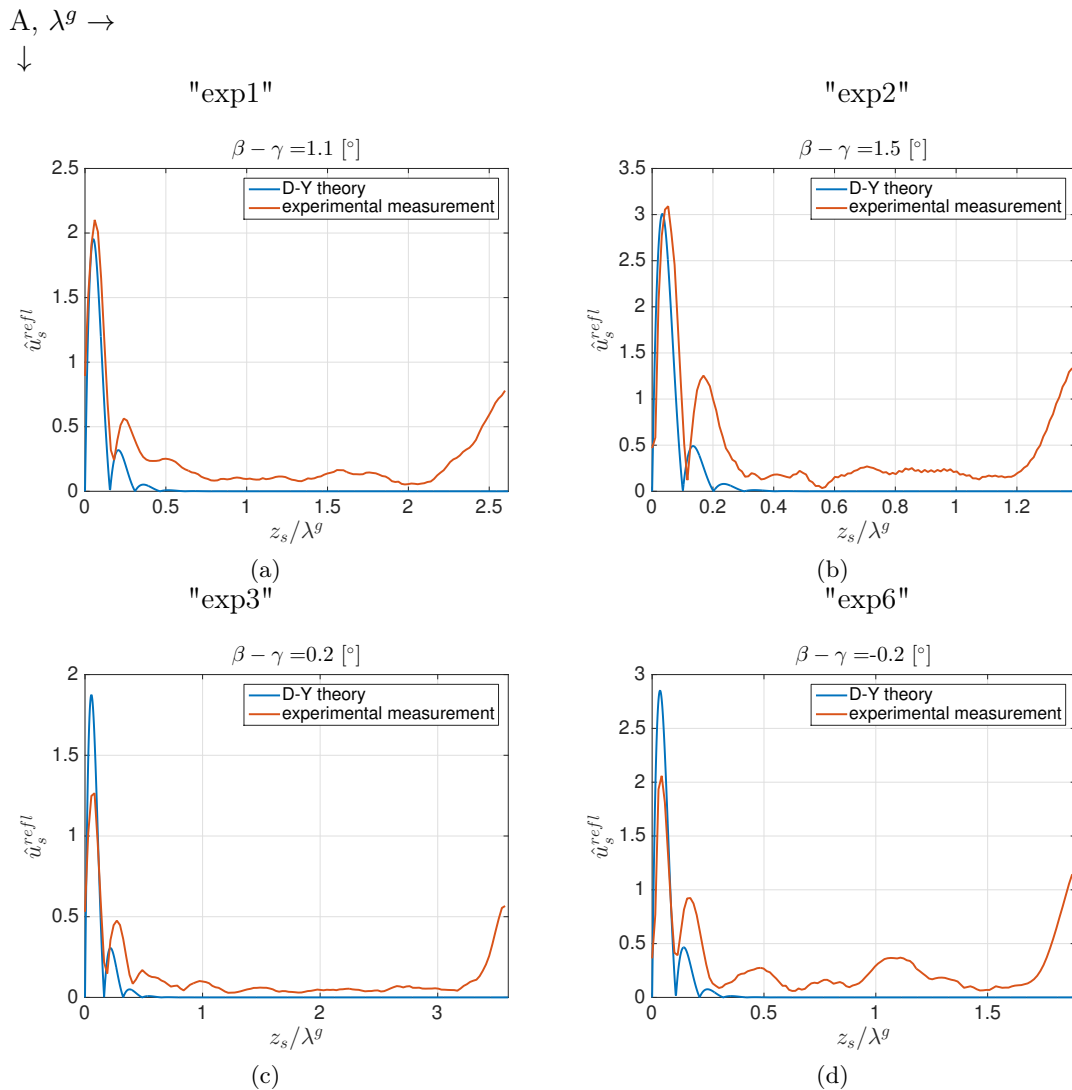


Figure 4.17: \hat{u}_s^{refl} as a function of z_s/λ^g for experiments (order in increasing Re number): (a) "exp1", (b) "exp2", (c) "exp3" and (d) "exp6". The experiments present different set of parameters A and λ^g , and at the top left it is indicated in which sense these two parameters increases.

direction normal to the slope of the along-slope component of the velocity thanks to high resolution velocity fields. In the near critical cases we observed that the velocity profile proposed by Dauxois & Young successfully predicted the main features of the profile obtained experimentally.

4.5.4 Shear stress and Shields number

Let us come back to our initial question: can we generate grain transport with internal waves? in particular, can we generate grain transport by internal waves reflection? We will investigate this question through the Shields number presented in section 3.2.2.

Through the velocity profile of the along-slope component we can now estimate the shear stress, σ , exerted by the fluid at the boundary. It is important to mention that the shear stress that will be exerted at the boundary slope is a consequence of the superposition

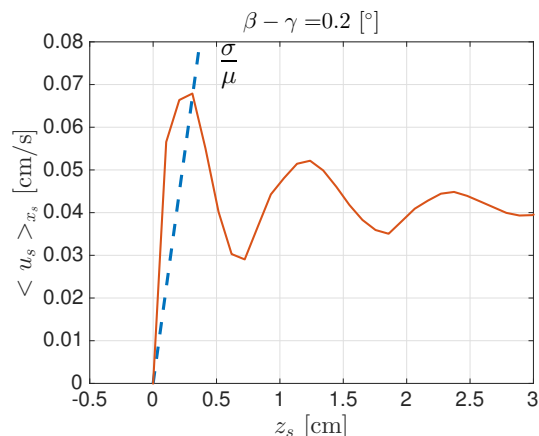


Figure 4.18: $\langle u_s \rangle_{x_s}$ as a function of z_s for positions close to the boundary slope (located at $z_s = 0$). With a dashed blue line is indicated the slope of the first peak from which the shear stress σ is estimated. The experiment used here to illustrate how σ is obtained is "exp3".

of both the incident and reflected wave. We will then use the profile of the complete velocity field in order to extract $\sigma(z_s = 0)$. We will make use of the peak in the amplitude of the profile $\langle u_s \rangle_{x_s}$ closest to the sloped boundary. The maximum of $\langle u_s \rangle_{x_s}$ will indicate how much the velocity changed in a distance close from the sloped boundary, $z_s = 0$, where the velocity is null. Naming these variations in velocity and position respectively Δu_s and Δz_s , we can estimate the shear stress at the boundary, $\sigma = \mu \partial u_s / \partial z_s$, by using the approximation $\sigma = \mu \Delta u_s / \Delta z_s$. An example of the estimation of $\sigma(z_s = 0)$ is represented in figure 4.18, where the velocity profile $\langle u_s \rangle_{x_s}$ of the complete velocity field is plotted as a function of z_s , for positions near the slope. Is indicated with a dashed straight line the slope of the first peak from which σ is estimated.

Figure 4.19 shows the shear stress divided by the dynamic viscosity of the fluid (same constant coefficient for all experiments), σ/μ , as a function of $\beta - \gamma$, for experiments "exp1", "exp2", "exp3" and "exp6". One can observe that the smallest values of σ corresponds to large values of $|\beta - \gamma|$, in particular, the values of σ are smaller for $\beta - \gamma$ negative. For each experiment, the largest values of σ are found in the interval $0 \lesssim \beta - \gamma \lesssim 5^\circ$. In particular, in figure 4.19(c), one can evidence the increase of σ as approaching the angle $\beta - \gamma \approx 2^\circ$. The largest values of σ can be found, as expected, in "exp6", which corresponds to the experiment with largest Re number.

From the values estimated for σ , shown in figure 4.19, one can compute the Shields number by using equation (3.1). In figure 4.20 is plotted the Shields number Θ as a function of $\beta - \gamma$, for hollow glass (a) and Polystyrene (b) particles. Both plots show values of Θ corresponding to experiments "exp1", "exp2", "exp3" and "exp6". For calculating Θ , we considered that the particles are surrounded by a fluid with density $\rho = 1.030 \text{ g/cm}^3$. We can observe that the values of Θ as a function of $\beta - \gamma$ increases with the Reynolds number of the experiment. This is what we expected, given that a strong flow will generate transport of grains more easily than a weak flow. Nevertheless, the Shields threshold number $\Theta_{th} = 0.12 \pm 0.2$, is larger than the Shields number obtained through experimental measurements. For the hollow glass type of particles, the maximum value reached for the Shields number is smaller than half of Θ_{th} (figure 4.20 (a)). This difference is even more evident for the Polystyrene particles, for which the maximum value of the Shields number is ~ 0.01 (figure 4.20 (b)).

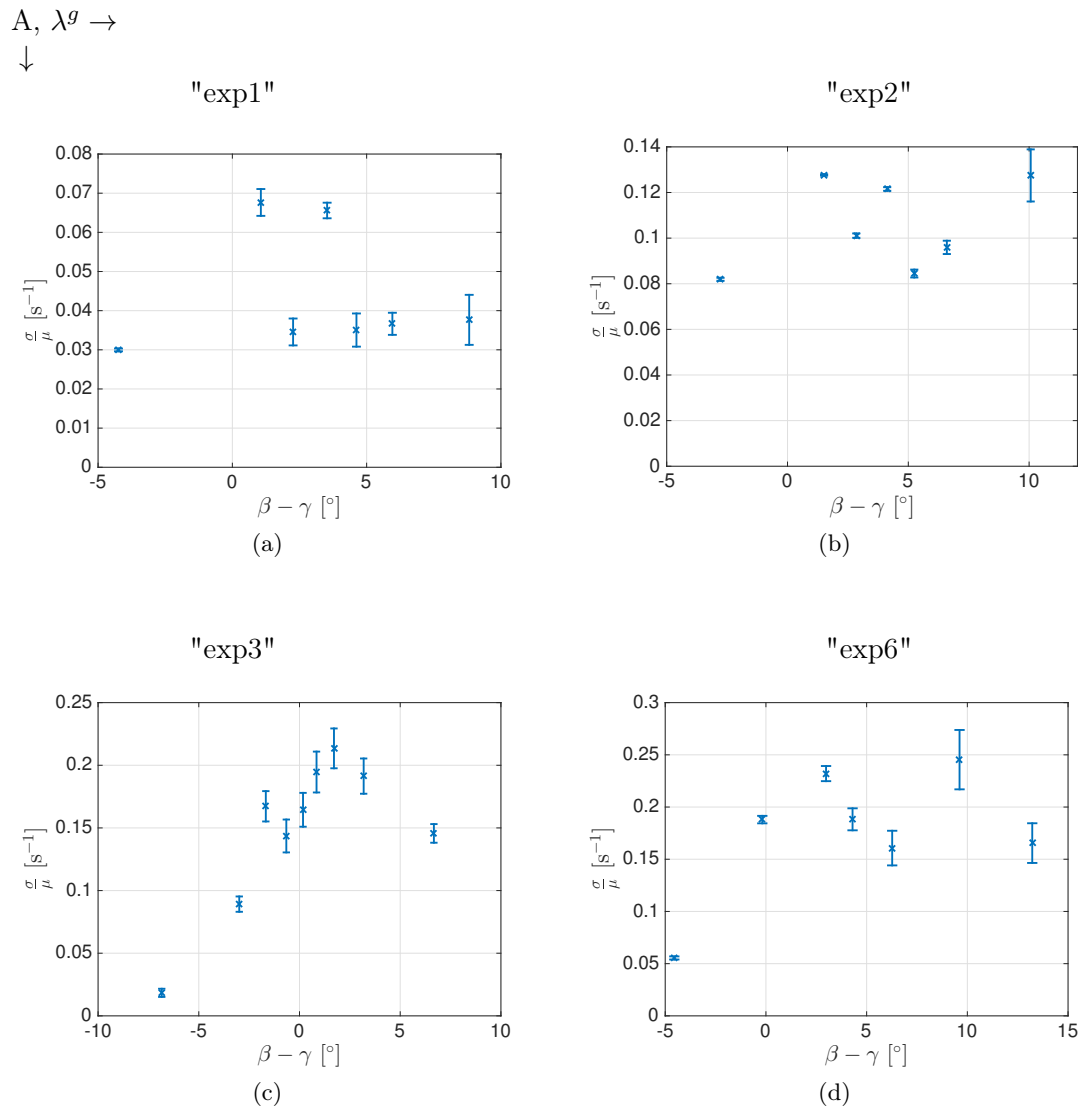


Figure 4.19: σ/μ as a function of $\beta - \gamma$ for experiments "exp1" (a), "exp2" (b), "exp3" (c) and "exp6" (d).

The estimation of the Shields number for the internal plane waves reflection experiments, indicates that it is very unlikely to generate grains transport, even with the very small hollow glass particles.

4.5.5 Vertical mode reflections

In the experiments in which the internal waves are generated with a vertical mode profile wave generator, the reflection process is different with respect to the case of plane waves. The wavefield involved in the reflection is not localized in a beam as in the case of the plane waves, instead, the complete vertical profile generates an increase of the velocity field near the boundary when the reflection occurs. The wavelength associated to this vertical mode is of the size of the tank, in consequence it is possible to observe one or less wavelengths in a field of view smaller in size that the complete tank. Therefore, the decomposition of the incident and reflected wave cannot be done through VMD method, as several wavelengths within the field of view are necessary to identify the wavenumber associated to the wave.

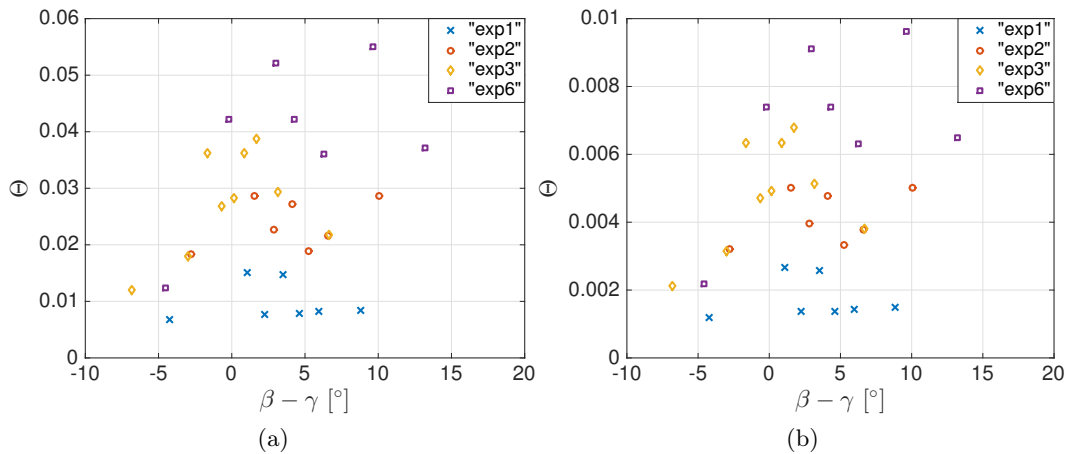


Figure 4.20: Shields dimensionless number as a function of $\beta - \gamma$ for experiments "exp1", "exp2", "exp3" and "exp6". The Shields number is estimated for hollow glass particles (a), and for Polystyrene particles (b).

In consequence the velocity profile will not be compared with the solution presented by Dauxois & Young, given that the reflected wave cannot be isolated. Nevertheless, the shear stress σ at the boundary can be estimated, given that it is a result of both incident and reflected wave together (as described in section 4.5.4).

In figure 4.21 is shown the velocity field u_s for a reflection of an internal wave generated by the vertical mode over a slope, corresponding to experiment "exp9". When $\beta - \gamma \approx 0$ (figure 4.21(a)), the reflected wave is confined near the boundary as expected and focusing of the wave beam occurs. When $\beta - \gamma > 0$ the reflected wave detaches from the boundary and propagates upward (figure 4.21(b)), contrary to what happens when $\beta - \gamma < 0$ in which the wave propagates downward (figure 4.21(c)).

The shear stress σ near the boundary has been estimated by using once again the quantity $\max(\hat{u}_s)$ involving the complete wavefield generated by the incident and reflected wave. The shear stress σ is obtained and the Shields dimensionless number can be estimated for a given particle. Figure 4.22 shows the Shields number Θ as a function of $\beta - \gamma$ for experiments "exp8" and "exp9" by using the hollow glass particles (a) and the Polystyrene particles (b) (we considered that the particles are located around the isopycnal $\rho = 1.03 \text{ g/cm}^3$). One can observe that the maximum value of Θ is reached for the most critical reflection for experiment "exp8", whereas the maximum is reached at $\beta - \gamma \approx 5^\circ$ for experiment "exp9". For the hollow glass particles in the angle interval $0^\circ \leq \beta - \gamma \leq 10^\circ$ the Shields number is slightly larger than the threshold Shields number $\Theta_{th} = 0.12$, indicated with a dashed horizontal line in figure 4.22(a). This indicates that the Shields model predicts the possibility of particles erosion for these configurations. Nevertheless, the largest value obtained for the Shields number slightly overpasses the threshold value. As described in chapter 3, no bed load transport has been observed.

4.5.6 Shields and Reynolds numbers

In order to observe how the focusing and the absolute intensity of the reflected wave in a critical reflection change for different experimental parameters, we plotted in figure 4.23(a) the value $\max(\hat{u}_s^{refl})$ as a function of the Reynolds number Re for the experiments presented in table 4.1. The value $\max(\hat{u}_s^{refl})$ is taken for the most critical reflection of each experiment

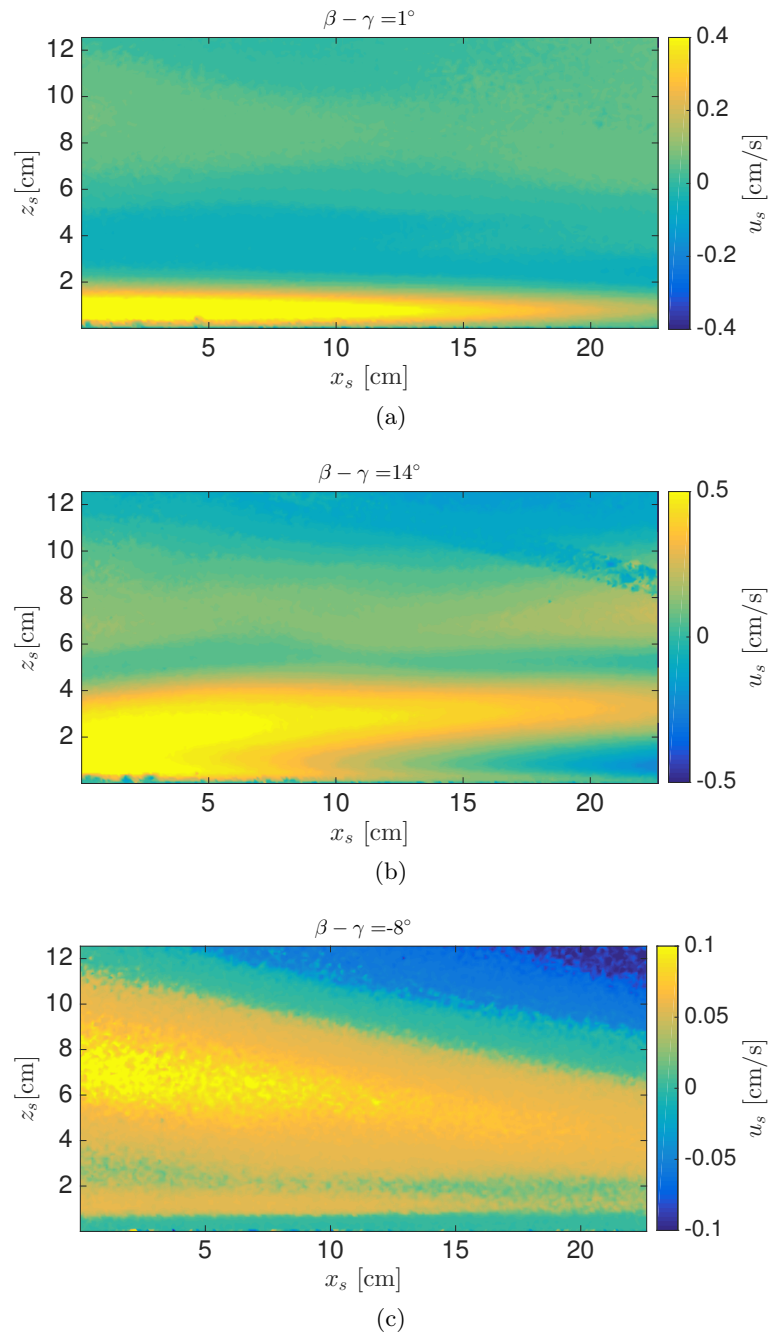


Figure 4.21: Snapshot of the velocity field u_s for an internal wave reflection generated with a vertical mode corresponding to experiment "exp9". Different frequencies (propagation angle β) have been explored, $\beta - \gamma = 1^\circ$ (a), $\beta - \gamma = 14^\circ$ (b) and $\beta - \gamma = -8^\circ$ (c).

(smallest $|\beta - \gamma|$). We can observe that the value $\max(\hat{u}_s^{refl})$ increases as expected with the Reynolds number.

In the case of the experiments performed with the vertical profile wave generator, as the incident and reflected wave cannot be separated through VMD decomposition method, we will approximate the value representing the intensity of the incident wavefield as $u_s^{inc} = A\omega_0 \cos \beta$, where A and ω_0 are the amplitude and the forcing frequency of the wave generator respectively, and the factor $\cos \beta$ models a transfer term of the wave

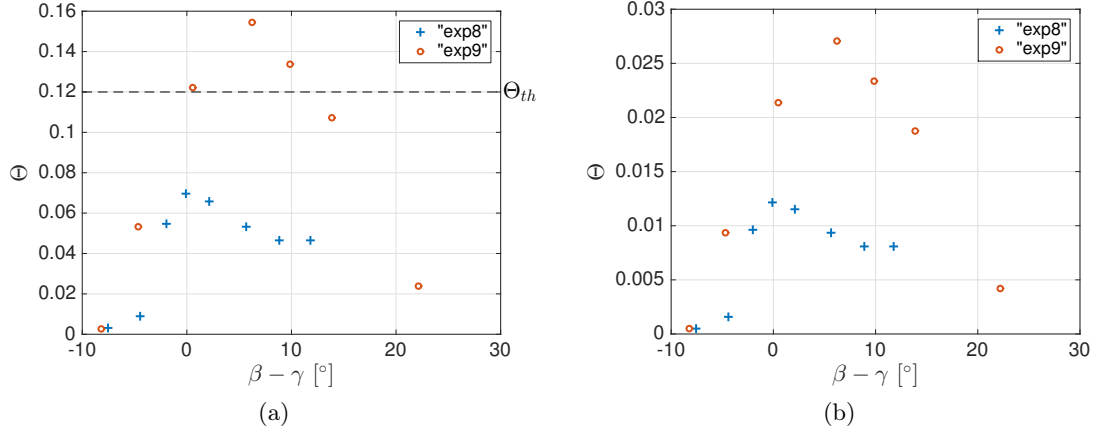


Figure 4.22: Shields dimensionless number Θ as a function of $\beta - \gamma$ for experiments "exp8" and "exp9". The Shields number is estimated for hollow glass particles (a), and for Polystyrene particles (b)

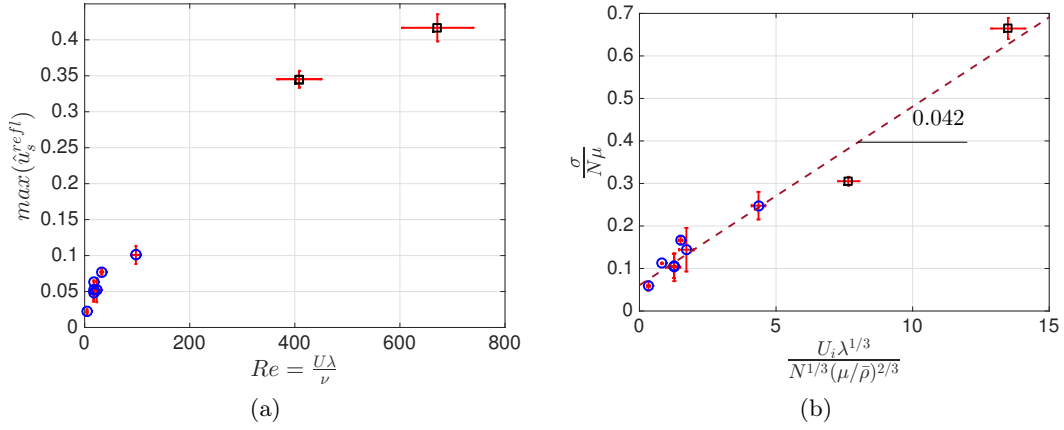


Figure 4.23: $\max(\hat{u}_s^{refl})$ obtained for the most critical reflection of each experiment (smallest $|\beta - \gamma|$), as a function of the Re number (a). Dimensionless shear stress $\frac{\sigma}{N\mu}$ for the most critical reflection as a function of $\frac{u_s^{inc} \lambda^{1/3}}{\nu^{2/3} N^{1/3}}$ (b), with a dashed line is plotted the linear regression performed to the experimental results. The experiments for which the forcing is performed with plane waves are indicated with circles (o), whereas the squares (□) indicate the experiments performed with vertical mode.

generator. As the distance between the source and the location where the reflection occurs is of the order of one wavelength λ^g of the vertical profile generator, the effect of dissipation over the intensity of the wave has been neglected.

The intensity and focusing of the reflected wave are both contained in the quantity σ . By using the solution developed by Dauxois & Young for critical and viscous reflections expressed in equation (4.40), one can estimate the value and position where the profile $\langle |u_s^{refl}| \rangle_{x_s}$ is maximum, that is, the value of the first peak used to estimate the shear stress σ in section 4.5.4. Making the approximation that the shear stress σ in the boundary is equal to the maximum value of $\langle |u_s^{refl}| \rangle_{x_s}$ divided by the distance between the maximum and the boundary, one can predict the dependence of σ with u_s^{inc} and λ :

$$\sigma^{DY} \propto \frac{u_s^{inc} \lambda^{2/3}}{\lambda^{1/3}} = u_s^{inc} \lambda^{1/3}, \quad (4.42)$$

where we omit a multiplicative term that depends on the geometric configuration of the slope. We plotted in figure 4.23(b) $\frac{\sigma}{N\mu}$ estimated from the experimental results, as a function of the dimensionless quantity $\frac{u_s^{inc} \lambda^{1/3}}{\nu^{2/3} N^{1/3}}$, where ν , the kinematic viscosity, is the same for all the experiments. With a dashed line is plotted the linear regression made over the experimental values of $\frac{\sigma}{N\mu}$. One can observe, that in effect, the increase of σ with $u_s^{inc} \lambda^{1/3}$ is quite linear within the values explored in this work. The slope of the linear regression is equal to 0.042 as illustrated in figure 4.23(b). This shows that the solution for critical and viscous reflections (equation (4.40)) predicts successfully the shear stress σ for near critical reflections.

As explained previously, by considering a given particle size and density, the Shields number can be estimated from the shear stress σ . In figure 4.24 is shown the Shields number Θ as a function of $\frac{u_s^{inc} \lambda^{1/3}}{\nu^{2/3} N^{1/3}}$ for hollow glass particles (a) and Polystyrene particles (b). Again we observe a linear dependency of Θ with $\frac{u_s^{inc} \lambda^{1/3}}{\nu^{2/3} N^{1/3}}$. For the hollow glass particles, as we observed before, the largest value reached for the Shields number slightly exceeds the threshold value $\Theta_{th} = 0.12$. Whereas for the Polystyrene particles, all the Shields number computed by using the experimental results are below the threshold value.

The linear dependency of σ with $u_s^{inc} \lambda^{1/3}$ allows us to establish the experimental limits in laboratory experiments for generating transport or erosion of a bed formed by a given particle. For example, if we want to achieve a Shield number $\Theta = 2 \cdot \Theta_{th} \approx 0.24$ for the Polystyrene particles, the solution of equation (4.40) predicts that we would need $\frac{u_s^{inc} \lambda^{1/3}}{\nu^{2/3} N^{1/3}} = 220$, which corresponds to velocities of u_s^{inc} larger than 2 cm/s, for a wavelength of 90 cm (considering the same viscosity and buoyancy frequency).

If we project the linear dependence of the shear stress σ with $\frac{u_s^{inc} \lambda^{1/3}}{\nu^{2/3} N^{1/3}}$ to oceanic conditions, we can estimate the Shields number and examine if the model predicts erosion of the particles bed. If we consider an internal wave with $\lambda = 100$ m, and generating maximum velocities of 0.3 m/s in an ocean with a buoyancy frequency $N = 10^{-3}$ rad/s, the computed Shields number for typical sand particles ($\rho_p = 2.62$ g/cm³, $d = 200$ μ m) will be $\Theta \approx 0.02 < \Theta_{th}$, predicting that no transport of sediments will occur in the ocean for these chosen conditions.

In order to summarize the results found in this section let us rewrite the equations relating the shear stress σ with the Shields number Θ and incorporate the result of linear dependency of the σ with $u_s^{inc} \lambda^{1/3}$,

$$\Theta = \frac{\frac{\sigma}{\mu} \mu}{(\rho_p - \rho)gd} = C_p \frac{\sigma}{\mu} \quad (4.43)$$

where the influence of the parameters involved in the particle characteristics and buoyancy force are comprised in the coefficient C_p . For experiments ranging between $Re = 5$ and $Re = 600$, we obtain:

$$\frac{\sigma}{\mu} = C_\sigma \frac{u_s^{inc} \lambda^{1/3} N^{2/3}}{\nu^{2/3}}, \quad (4.44)$$

where the coefficient of the linear regression is $C_\sigma = 0.042$, so that,

$$\Theta = C_p \frac{\sigma}{\mu} = C_p C_\sigma \frac{u_s^{inc} \lambda^{1/3} N^{2/3}}{\nu^{2/3}} \quad (4.45)$$

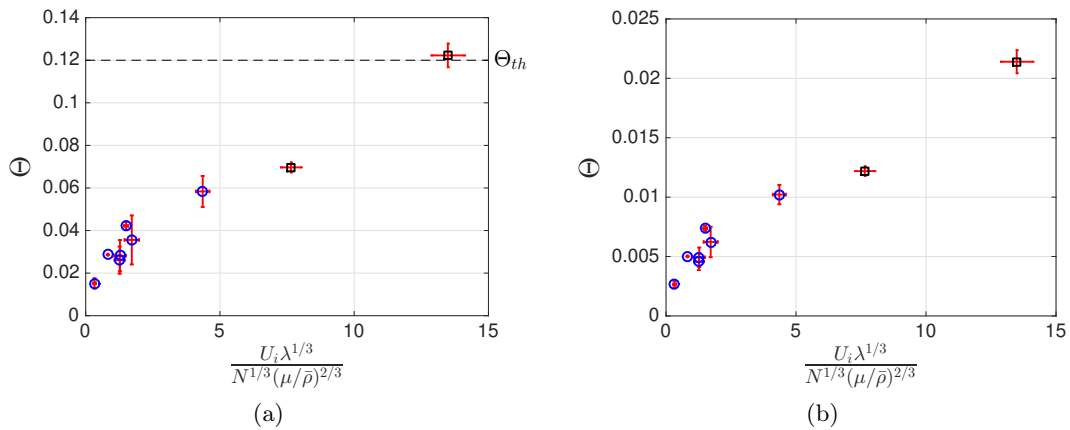


Figure 4.24: Shields number Θ as a function of $\frac{u_s^{inc} \lambda^{1/3}}{\nu^{2/3} N^{1/3}}$ for all experiments presented in table 4.1, computed for hollow glass particles (a) and Polystyrene particles (b). The experiments for which the forcing is performed with plane waves are indicated with circles (\circ), whereas the squares (\square) indicate the experiments performed with vertical mode.

We expect that this result can be used for experimental configurations that go beyond the limits of our experiments.

4.6 Conclusions

The initial motivation of performing experiments of internal waves reflection in the critical and near critical cases was to understand the conditions in which the reflection process will increase the shear stress σ at the boundary to an amplitude large enough to generate erosion of grains in a particle bed. In order to understand the reflection process, we performed experiments in a wide range of parameters and configurations, which allowed us to comprehend the limitations in our systems and to be able to predict under which circumstances erosion is expected by the Shields approach.

We have developed, in a collaborative work, and applied to our experimental measurements, an image processing technique which allows to decompose the wavefield in the various wave components involved in an internal wave reflection by using its particular spectral content. This method minimizes the boundary effects in the field of view and satisfactorily decomposes the waves involved. It allows to decompose the wave in as many modes as desired. This feature has been used in order to identify when a near critical reflection involves two (incident and reflected) or three (incident, reflected upward and reflected downward) wave components. This allows to identify not only the angle interval $\beta - \gamma$ where the linear theory fails in predicting a single reflected wave, but also permits to have a precise identification of the reflected wave in this interval composed by both the upward and downward reflected wave.

The high resolution measurements of the velocity field of an internal wave reflection near the slope, together with the capability of decomposing the wavefield in a incident and reflected wave, allowed to compare for the first time experimental results with a theoretical solution of the velocity field near the boundary in an internal wave critical reflection developed by Dauxois & Young. We observed that the theory manages to represent the main features of the velocity field near the boundary.

In addition, the shear stress σ at the boundary exerted in an internal wave reflection

has been obtained in experiments with different parameters, ranging from $Re = 5$ to $Re = 600$. We observed that for each experiment the shear stress σ is larger for angles $\beta - \gamma$ that are critical or slightly positive. Through the shear stress σ we estimated the Shields dimensionless number for hollow glass and Polystyrene particles, which allowed us to estimate the limits of erosion and transport expected for the Shields approach for our experimental conditions.

The theoretical solution for the velocity field in a critical reflection allowed us to estimate the shear stress σ and the dependency of this quantity in the experimental parameters. The shear stress obtained experimentally is in good agreement with the theory for the experimental parameters explored in this work. This allows to estimate under which condition erosion in a bed of grains is predicted for a given particle and experimental configuration, as well as an oceanic situation.

Particles in suspension



Satellite view of thin clay particles driven from Rio de la Plata estuary towards the south Atlantic ocean. Photo Credit: NASA Visible Earth.

The existence of fluid flows over granular systems can be found in many natural environments, and we have already seen that, for some particular conditions of both the flow and the grains, erosion and resuspension can be generated.

The trajectory of a particle in suspension will respond to a balance between advective, inertial and viscous forces. When many particles are transported in resuspension, the behavior gets more complicated. The dynamics of a many-particles system in a fluid, in some cases, is closer to the behavior of a two-phase flow than to the behavior of an individual grain. One can see that the complexity will increase if we now add that the surrounding fluid in which

the particles are immersed is stratified. Despite the complexity of the system, we will be situated in a configuration close to oceanic and atmospheric conditions. In this configuration we will study experimentally the motion, induced by internal gravity waves, of particles in suspension.

5.1 Suspended particles: nature and experiments

When particles are suspended in a viscous fluid, the trajectory of these particles can reach large distances before settling on a boundary. This process can be found in multiple cases in geophysical processes. For example, a volcanic eruption can send ash high into the atmosphere which can travel thousands of kilometers [31]. In cases where a combination of small ash particles, which take a long time to fall on the ground, and high winds of the jet stream can result in this ash plume being carried around the globe [14]. Other typical case of particle resuspension can be found in rivers. The sediments transported by rivers into estuaries modify the turbidity and concentration of particles in the ocean in vast regions [51], and can even be remotely carried by ocean currents before settling on the seafloor. In addition, many mechanisms can generate resuspension of sediments directly from the oceanic boundaries.

Many biological systems in the ocean depend on the resuspension and transport of sediments and nutrients. For example the benthic boundary layer, which represents a ~ 10 m layer above the sea floor, plays a vital role in the cycling of matter thanks to the variety of suspended materials [2].

Marine aggregates of biogenic origin, known as marine snow, are considered to play a major role in the ocean particle flux and may represent a concentrated food source for zoo-plankton [49]. These particles in suspension are found to be transported by internal gravity waves. It has been observed for example, that humpback whales aggregate in regions because of the presence of planktivorous fish, which in turn respond to zooplankton concentrated by internal gravity waves transport [58, 50].

Many efforts have been done to understand the behavior of particles in suspension in a stratified fluid. In particular, the study of individual particles settling in stratified fluid has been performed experimentally [13, 75] and numerically [3, 75], in order to understand the complex dynamics of these particles. A many-particle approach has been performed by Bush *et al.*, who studied the dynamics of particle clouds in a stratified fluid [10]. Snow *et al.* [65] studied experimentally the behavior of particle-laden flows down a slope into linearly stratified ambient fluids.

We will study the effect of settling particle in a linearly stratified fluid. In particular, the particles will settle in a columnar shape configuration. The effect of internal gravity waves on the particles in suspension and on the column as a whole will be analyzed, as well as the effect of the particles on the waves.

5.2 Experimental setup and system description

5.2.1 System description

The experimental system used to study the interaction between internal gravity waves and particles in suspension can be observed in figure 5.1. The main experimental parameters controlled during the experiments are given in the figure. In a linearly stratified tank internal gravity plane waves are generated from the left side of the tank and propagate with an angle β through a localized column of particles in suspension before dissipating at the right side of the tank.

5.2.2 Experimental setup

In order to study experimentally the interaction between internal gravity waves and particles in suspension we used a tank of dimensions $80 \times 17 \times 42$ cm³ in the directions x , y and z

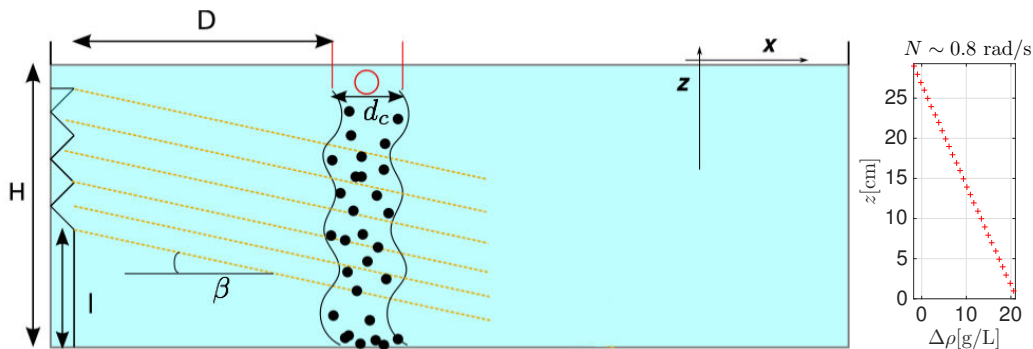


Figure 5.1: Schematic diagram of the experimental system. The plane wave generator is located at the left of the tank. The column of particles of size d_c is created at a distance D from the wave generator, so that the waves pass roughly through the center of the column for the different directions of propagation β used in the experiments. On the right is plotted an experimental measurement of the density (crosses) as a function of the water depth.

respectively. The tank is filled with salt water through the double bucket method described in section 2.1.1 in order to obtain a linear stratification in density and, therefore a constant buoyancy frequency N . Internal plane waves are generated with a moving boundary generator described in section 2.1.3 and section 2.1.3, which is positioned vertically at the side of the tank as sketched in figure 5.1.

A particle injector has been developed (described in detail in section 5.2.3) in order to generate a vertical column of particles in suspension. The size and position of the column in the x direction is variable, and in the y direction the column is fairly homogeneous along the width of the tank.

The visualization of the wavefield is performed thanks to Synthetic Schlieren technique (described in section 2.1.4), where the variation in the density of the fluid is related to the variation in its refractive index. The luminous screen used for the Synthetic Schlieren visualization is also employed to identify the edges of the column of particles in suspension, as well as its relative intensity, related to the particle concentration.

5.2.3 Particle injector

The theory that describes internal gravity waves in section 1.1, refers to a two-dimensional perturbation. The internal waves generated in our experiments are also two-dimensional. This is why we have chosen to conserve this symmetry for the particles in sedimentation. We generated a column of particles of a controlled size, along the x direction of the tank. The particles are injected through a slitted copper tube extended along the y direction. The particles are previously mixed with a fluid in order to avoid their clustering during the immersion in the stratified fluid (see figure 5.2 (a)). This is performed in a small container where a mass m of particles is mixed with a volume V of fresh water (density $\rho = 0.998 \text{ g}\cdot\text{cm}^{-3}$) with some drops of surfactant (to prevent further clustering). The water will act as a dragging fluid for the particles. The fluid carrying the particles is then injected thanks to a peristaltic pump into the tank through the copper tube allowing the particles to settle in the stratified fluid, and then the dragging fluid is sucked out at the other end of the tube with the same flow rate as at the input, so that the level of water in the stratified tank remains constant. The flow rate has been chosen to be the smallest possible that avoids sedimentation of the particles in the tube ($Q = 20 \text{ cm}^3\cdot\text{min}^{-1}$). The interest of

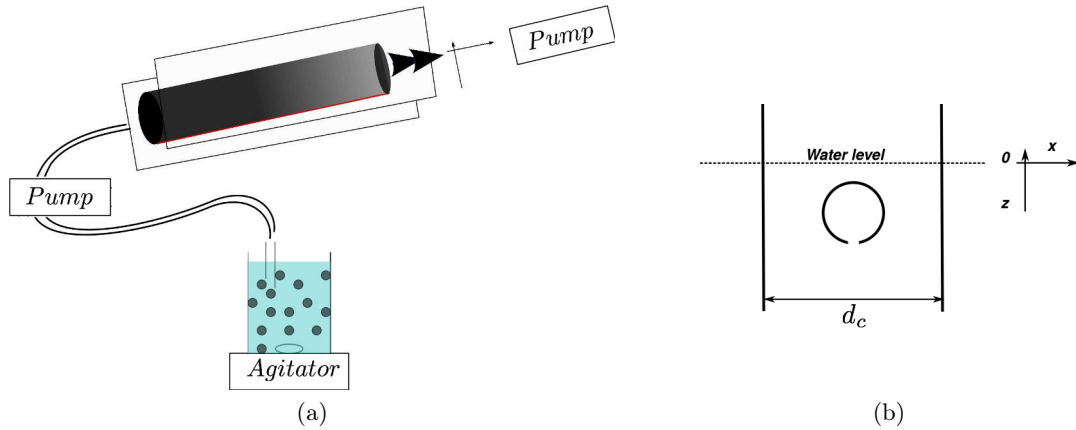


Figure 5.2: Diagram of the particle injector. Figure (a) shows how the particles are mixed prior to the injection, (b) shows a front view of the copper tube immersed in the water and contained between two PVC plates.

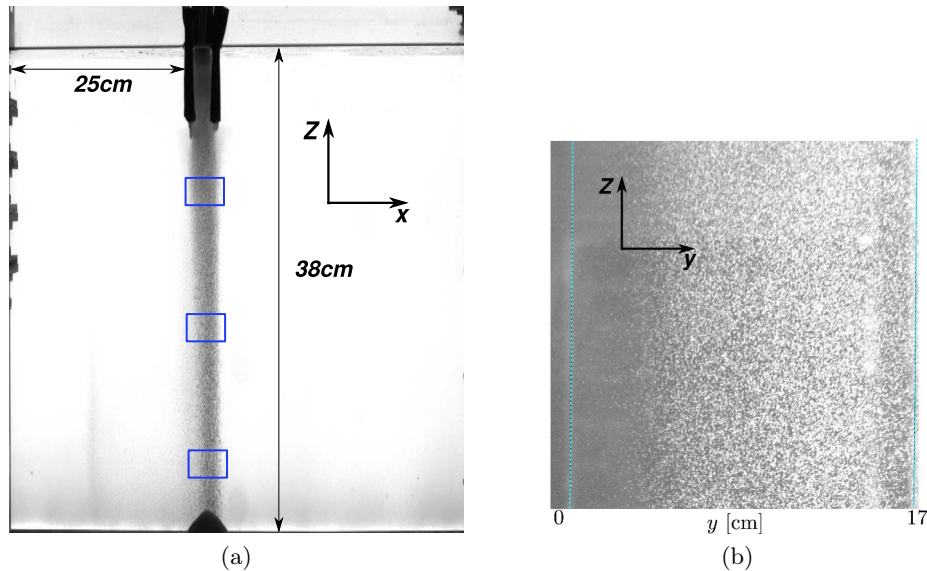


Figure 5.3: View of the column of particles in suspension in the stratified fluid. (a) Front view of the column. (b) Side view of the column. The fluid dragging the particles is injected at constant flow rate ($Q = 20 \text{ cm}^3 \text{ min}^{-1}$). The three blue squares in (a) illustrate where the variations of concentration will be measured.

setting a small flow rate is that the initial velocity of the particles in the stratified tank will be also small, allowing the sedimentation process to be rapidly reached. The copper tube is immersed in the stratified fluid, 2 cm below the free surface, where the surrounding fluid is denser than the dragging fluid. This allows the particles to rain out meanwhile the dragging fluid stays in the copper tube or ascends to the surface. We recall that when particles are introduced from above a stratified fluid, the particles will first form a particle cloud that behaves as a plume, followed by a state in which the particles rain out of the cloud as individuals, as previously mentioned in section 3.2.3. This description is in agreement with what we observe experimentally. In order to contain the cloud in a confined region, we installed two PVC plates at the sides along the copper tube, as illustrated in the diagram of figure 5.2 (b), so that the particles rain down from a predefined region.

The specifications for the creation of the particle column was the realization of a two-dimensional localized homogeneous column. The results obtained by using the experimental setup described, can be observed in figures 5.3(a) and (b). Figure 5.3(a) shows a localized column, one can observe that the size of the column does not change with the vertical location, given that the particles when settling descend vertically without any important horizontal motion. Figure 5.3(b) shows the repartition of particles along the y coordinate of the tank, where, as can be observed, the particles are homogeneously spread at the center of the tank, and the column covers approximately two thirds of the width of the tank. We make the assumption that this column will present the same features as if it was completely two-dimensional.

5.2.4 Generation of the column

The dynamics of particle clouds in a stratified fluid has been extensively described by Bush *et al.* [10], as previously mentioned in section 3.2.3. Nevertheless, our system differs from Bush's system by the fact that we are interested in generating a stationary and localized column of particles, which implies a constant flow rate of particles injected in the system. The particles introduced from above, form a particle cloud that behaves as a plume until it reaches an equilibrium vertical location, after which, the particles rain out of the cloud as individuals. Given the fact that in our experiments the particles are carried by a dragging fluid which is lighter ($\rho = 0.998 \text{ g cm}^{-3}$) than the surrounding fluid at the vertical location where the copper tube is located, the equilibrium vertical location of the plume is near the free surface of the fluid, allowing to confine the particle cloud thanks to the PVC plates, so that the particles rain out from a localized region.

The confinement of the particle cloud will depend among other things, on the depth where the PVC plates are located, on the initial velocity of the particle injection, on the concentration of particles in the dragging fluid and on the depth where the copper tube is immersed. We have performed exhaustive experiments in order to find the correct experimental parameters of our system, which permits the control of the region where the particles rain from.

5.2.5 Particles distribution and concentration

The PVC particles injected in the tank have an average diameter of $250 \mu\text{m}$, however, these particles are strongly hydrophobic and can cluster in the injection process. In addition, using an optical microscope we observed that the particles are widely distributed in size and not spherical.

The settling particles are enlightened with a uniform LED screen located behind the tank. A front view camera takes images of the column at 4 fps. The luminosity detected by the camera will decrease in the positions where the concentration of settling particles is not null. We have selected three square regions (50×50 pixel) of the column located at different vertical locations, illustrated in figure 5.3 (a) with three blue squares, where the average intensity in the squares is measured for each image. We have assumed a Beer Lambert law, which states that the luminous intensity I depends exponentially on the concentration of particles c in the fluid, that is,

$$I = I_0 e^{-\Gamma c} \quad (5.1)$$

where I_0 is the detected intensity when no particles are in the fluid and $\Gamma > 0$. In other words, the logarithm of the average intensity is proportional to the concentration of particles within the fluid. We then have access to the change in concentration through

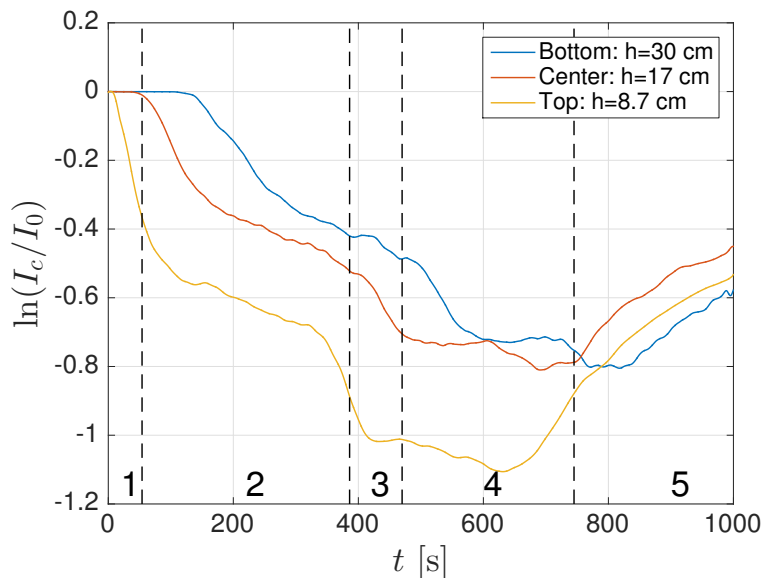


Figure 5.4: $\ln(I_c/I_0)$ as a function of time showing the different stages of the formation of a column of particles. The black dashed vertical lines indicate the division of the formation stages for the intensity of the center square. The intensity I_c is taken from the regions illustrated by the three squares in figure 5.3(a).

the quantity $\ln(I_c/I_0)$ as a function of time, where I_c is the average intensity in a selected region of the column, of particles concentration c and, I_0 is the average intensity of the background screen.

5.3 Dynamics of the column

As we can intuit, the sedimentation of the particles in a stratified fluid is more complicated than just a vertical drop. The particles will pass through different stages before reaching the bottom boundary. In order to control the localization, homogeneity and stationarity of the column, we will set the experimental parameters in a particular configuration by using the particle cloud sedimentation described in section 3.2.3.

5.3.1 Formation of the column

In the first place, we studied the behavior of the column without any wave perturbation. We focused on the evolution of the column formation, from the moment the first particles start to sediment until the source of particle injection is stopped. The evolution of the column is followed by measuring the particle concentration in the column.

5.3.2 Evolution of the concentration in the column

The variation of the concentration of particles in the column is measured for the three regions illustrated with squares in figure 5.3(a). In figure 5.4 is plotted $\ln(I_c/I_0)$ as a function of time for these three different vertical positions. The three curves follow the same dynamics shifted by a time interval Δt . This time is equal to the time it takes the particle to descend to the following point where the measurement is performed, from which we can estimate the sedimentation velocity.

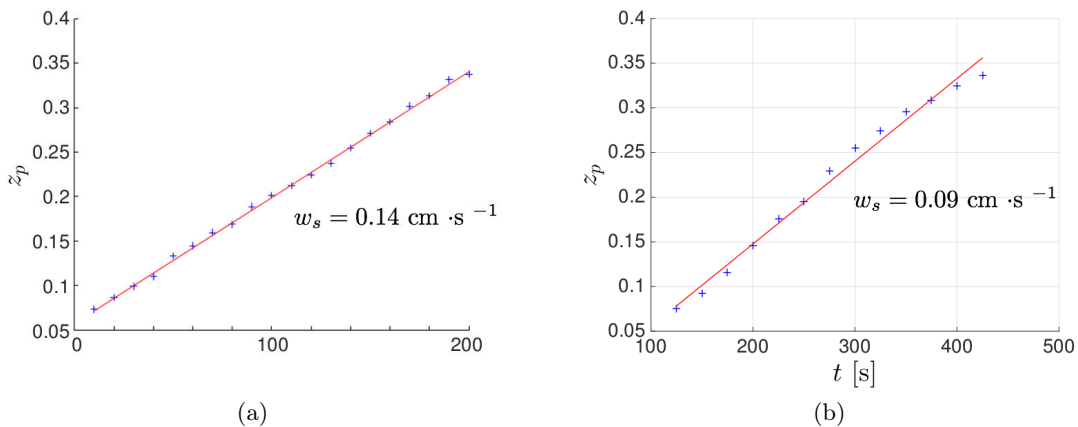


Figure 5.5: Depth of the particles front z_p as a function of time, for (a) a stratification with buoyancy frequency $N = 0.8 \text{ rad}\cdot\text{s}^{-1}$ and (b) for $N = 1.1 \text{ rad}\cdot\text{s}^{-1}$. The line shows the result of a linear regression.

In the evolution of the formation of the column one can distinguish different stages. Taking the intensity evolution for the intermediate vertical location (17 cm) we associate the stages to:

1. No particles: The first stage is when no particles are present in the area where the intensity is averaged, so that, $\ln(I_c/I_0) = \ln(I_0/I_0) = 0$. This stage is related to the initiation of the injection of particles.
2. Increasing amount of particles: This stage is associated to the fact that the particles form a cloud before dropping down. The first injected particles mix with the surrounding fluid and eventually rain down. The injector keeps introducing particles in the volume where the mixing occurs, and the rate of particles that rain down increases. Given the fact that the mixing occurs in a confined volume (thanks to the PVC plates illustrated in figure 5.2(b)), after the transient the rate of particles that rain down will equal the rate of particles introduced by the injector.
3. Cloud saturation: Before reaching a stationary stage there is a sudden increase of the concentration of particles in the column. This effect is consequence of a saturation of particles that can be stored in the cloud, which is followed by the collapse of the cloud and the ejection of a large amount of particles.
4. Stationary: Once the rate of particles injected and particles raining down are equal, a stationary phase is reached.
5. Decreasing amount of particles: When the injection of particles is stopped, the concentration of particles will slowly decrease.

We have chosen to work in the stationary stage, given that the concentration of particles is practically constant, allowing to reduce the number of parameters. This concentration is controlled by the rate of injected particles, which we have kept equal for all experiments.

Sedimentation velocity

We have performed the measurement of the sedimentation velocity by using the time where the front of the column arrives at points located at different vertical locations. This is done

thanks to the easy identification of the instant where a region passes from having no particles to observing the first particles. This procedure has been repeated for two stratifications with different buoyancy frequency N . The results can be observed in figure 5.5. A linear regression to the experimental values allows to estimate the sedimentation velocity, that is, $w_s = 0.14 \text{ cm}\cdot\text{s}^{-1}$ for the stratification with $N = 0.8 \text{ rad}\cdot\text{s}^{-1}$ (see figure 5.5(a)), and $w_s = 0.09 \text{ cm}\cdot\text{s}^{-1}$ for $N = 1.1 \text{ rad}\cdot\text{s}^{-1}$ (see figure 5.5(b)). One can notice that a variation of 25% in the value of N generates a change of 43% in the sedimentation velocity, for the PVC particles. In addition, the linear adjustment is less accurate over the experimental values in the experiment with $N = 1.1 \text{ rad}\cdot\text{s}^{-1}$ than for $N = 0.8 \text{ rad}\cdot\text{s}^{-1}$.

A theoretical approach can be performed in order to estimate the sedimentation velocity of a particle in a homogenous fluid. We will use this result as an estimation of the order of magnitude. For a particle of size d in a fluid with dynamic viscosity μ , the Reynolds particle number is:

$$Re_p = \frac{\rho w_s d}{\mu}, \quad (5.2)$$

where ρ is the density of the fluid (for a stratified fluid we consider, at the first order, the averaged density), and w_s the sedimentation velocity. For our experiments, $Re_p = 0.4$, therefore we are in the Stokes regime, for which the flow generated by the settling spherical particles is laminar. In this regime, the dragging force exerted over the spherical particle will be:

$$\mathbf{F}_{drag} = -3\pi\mu d\mathbf{u}. \quad (5.3)$$

Furthermore, the gravity force over the particle is $\mathbf{F}_g = (\rho_p - \rho)d^3\mathbf{g}\pi/6$, where ρ_p is the density of the particle. The sedimentation velocity will be reached when these two forces balance. The Stokes sedimentation velocity, w_s^S will be,

$$w_s^S = \frac{d^2 g (\rho_p - \rho)}{18\mu}. \quad (5.4)$$

The sedimentation velocity in the Stokes regime approximation in a homogenous fluid, for our experimental conditions is $w_s^S = 0.17 \text{ cm}\cdot\text{s}^{-1}$. The Stokes model estimates a value of the sedimentation velocity which is closer with the results of the experiment performed with $N = 0.8 \text{ rad}\cdot\text{s}^{-1}$, that in the case of the experiment performed with a steeper stratification ($N = 1.1 \text{ rad}\cdot\text{s}^{-1}$). For the latest, the experimental result for w_s presents less agreement with the linear fit. This can be evidenced in figure 5.5(b), where the sedimentation velocity decreases for increasing depth as a consequence of the increase of the surrounding fluid density ρ . As the buoyancy frequency N increases, the approximation that the fluid is homogenous is not as good. As can be expected, we observed that an increase of the buoyancy frequency N implies a decrease of the sedimentation velocity w_s .

We recall that we estimated w_s for the front of the column of particles. The velocity of the particles inside the column, where group effects may affect the sedimentation velocity of a particle has not been measured.

5.4 Effect of the column over waves

We will first study the effect of the column of particles over internal gravity waves. We will perform this study by generating a beam of internal plane waves that propagate through the column of particles as described in the sketch of figure 5.1.

If the column of particles would be solid or have a very large concentration of heavy and large particles, then we expect the waves to bounce off the column and propagate

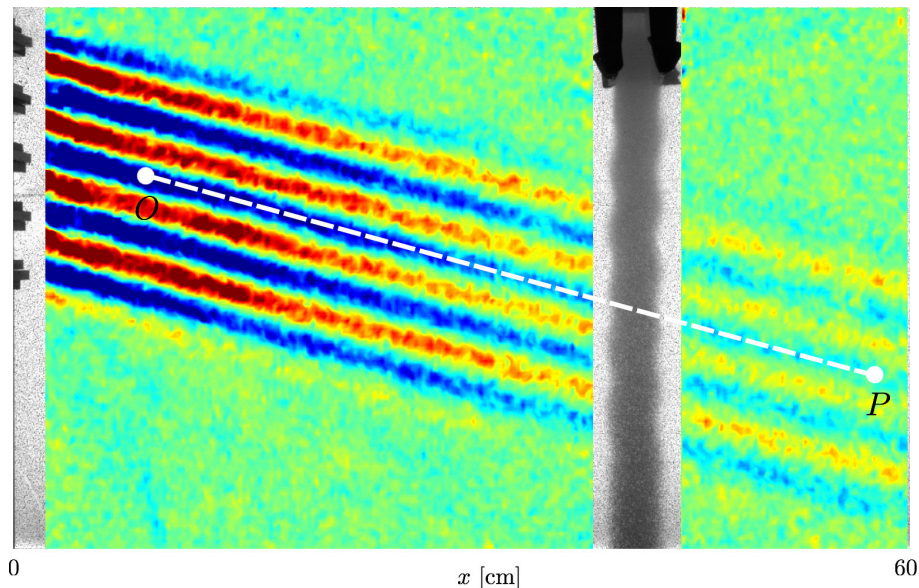


Figure 5.6: Internal wave beam passing through a column of sedimentation particles. The waves are generated in the upper-left corner and propagate to the right.

backwards, as if it would be a wall. On the other hand, if the column contains few small and light particles, we expect the wave to pass through the column without noticing it. If the concentration of particles in the column is such that it is between these two limit cases, then we expect a fraction of the wave energy to be transmitted through the column, and a fraction to be reflected on the column. In this case, there will be a loss in the intensity of the transmitted wave.

In a linearly stratified fluid with constant buoyancy frequency $N = 0.85 \text{ rad}\cdot\text{s}^{-1}$, we have generated internal waves with a generator with fixed amplitude, A , and vertical wavelength, λ^g . The same experiment is reproduced for several concentrations of the particle column: $c = 3 \text{ g}\cdot\text{L}^{-1}$, $c = 6 \text{ g}\cdot\text{L}^{-1}$, $c = 12 \text{ g}\cdot\text{L}^{-1}$, $c = 20 \text{ g}\cdot\text{L}^{-1}$.

In figure 5.6 is shown the wavefield of an internal wave beam passing through a column of sedimentation particles. We can notice that the wave passes through the column without reflecting. This is true also for the column with largest possible concentration of particles c . To be sure that no reflected wave is present, we applied the Hilbert transform to the wavefield (not shown) in order to filter only the waves propagating to the left (direction of a possible reflected wave) and we did not observe any perturbation in the wavefield.

In addition, the wave does not present any phase variation in the direction of propagation of the wave after passing through the column of particles. This result is an indicator that the buoyancy frequency N remains the same inside the column and outside of the column.

In order to observe if there is an effect of dissipation of the waves when passing through the column, we measured the decay of the amplitude of the wave in the direction of propagation of the wave, η , through all the segment OP (indicated in figure 5.6). In figure 5.7 is shown the evolution of the amplitude of the wavefield for three points selected on the segment OP . One can observe that the three signals have the same phase, and that the amplitude decreases for the points farther from the source. In order to measure the decay of the intensity of the wave, the amplitude evolution of the wave is extracted for each point in the segment OP . Then a temporal average is performed to the absolute value of this signal, from where we can extract the intensity of the wave in each point.

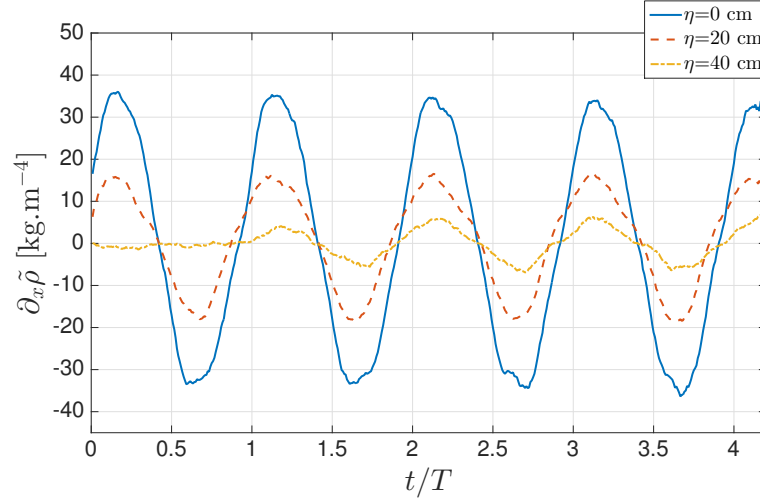


Figure 5.7: $\partial_x \tilde{\rho}$ as a function of time of the internal plane waves for three points of the segment OP , illustrated in figure 5.6. The distance from O is indicated in the legend. The signal with smallest amplitude corresponds to the wavefield at the right side of the column.

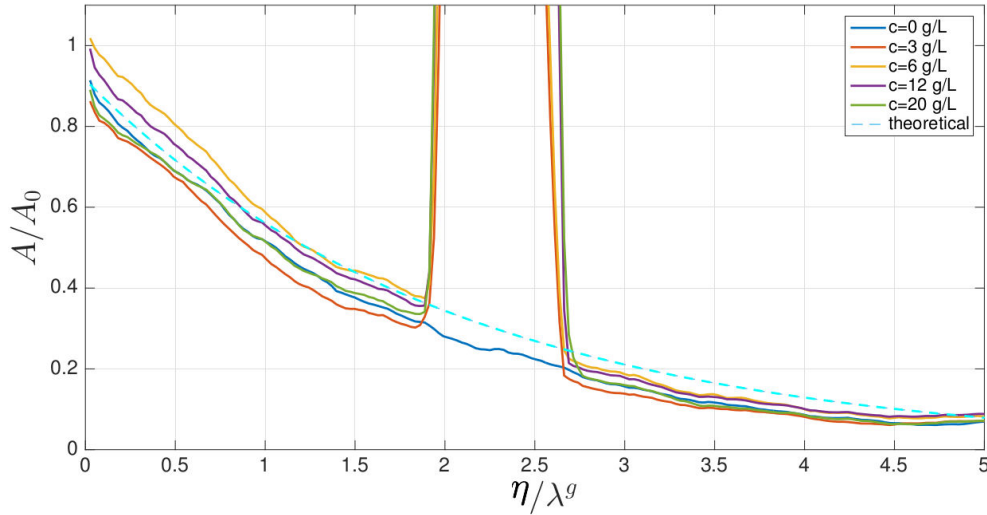


Figure 5.8: Normalized amplitude of the internal waves as a function of the position in the segment OP (indicated with a white dashed line in figure 5.6) for several concentrations c . In addition, the theoretical decay of the amplitude of the wave because of the viscosity is plotted.

In figure 5.8 is shown the normalized intensity of the wave, A/A_0 as a function of the normalized position, η/λ^g , within the segment OP , where A_0 is the intensity of the wave in O . We can confirm from figure 5.8 that the intensity of the wave decays as moving away from the source. The column is marked by a jump in the intensity for the experiments performed with a concentration c not null. We can observe that there is no difference in the waves amplitude for experiments performed with different concentrations. In fact, there is no perceptible difference with the experiment in which no column is present. In addition, is plotted the theoretical decay of the amplitude of the wave because of the viscosity of the fluid, of the form $\exp(-\Lambda\eta)$ where $\Lambda = \frac{|\mathbf{k}|^3}{2\sqrt{N^2 - \omega^2}}$.

In conclusion, for the experimental parameters used in this work, we have not seen any

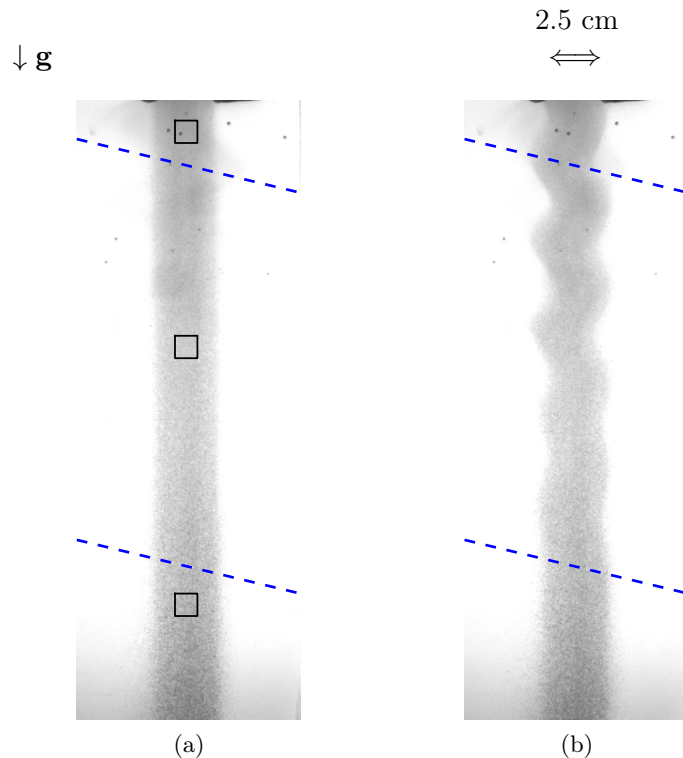


Figure 5.9: Front view of the column of sedimentation particles. (a) Snapshot at $t/T = 0$, where no wave perturbations are present. (b) Snapshot of the column during the pass of internal plane waves through the column, after 100 periods. The wave beam is located between the two blue dashed lines. Three squares in (a) indicate the regions where the intensity evolution is measured.

effect of the column over the internal waves. The direction of propagation of the wave remains equal after passing through the column of particles. No reflected wave has been observed. The column does not add any dissipation that can be perceptible in the intensity of the wave. The width and concentration of the column of sedimentation particles are increased to their maximum values acceptable for the experimental setup. For further work, we suggest to develop a system which allows a larger column and a wider range of particles concentrations that can be injected.

5.5 Effect of the waves over the column

When studying the effect of internal gravity waves over a column of sedimentation particles, we founded two main effects over the motion of the column:

1. The boundaries of the column oscillate around the initial position of the column.
2. The column is displaced from its original position, indicating a net transport of the particles in the column.

Even though these two processes can occur simultaneously, we will described them separately.

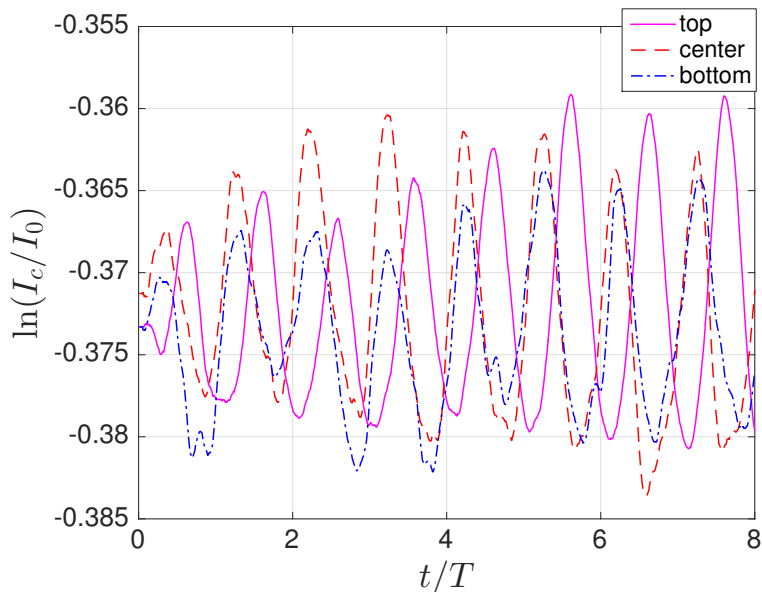


Figure 5.10: Oscillation of the concentration of particles in the column. $\ln(I_c/I_0)$ as a function of time, measured for the regions indicated with three squares in figure 5.9(a).

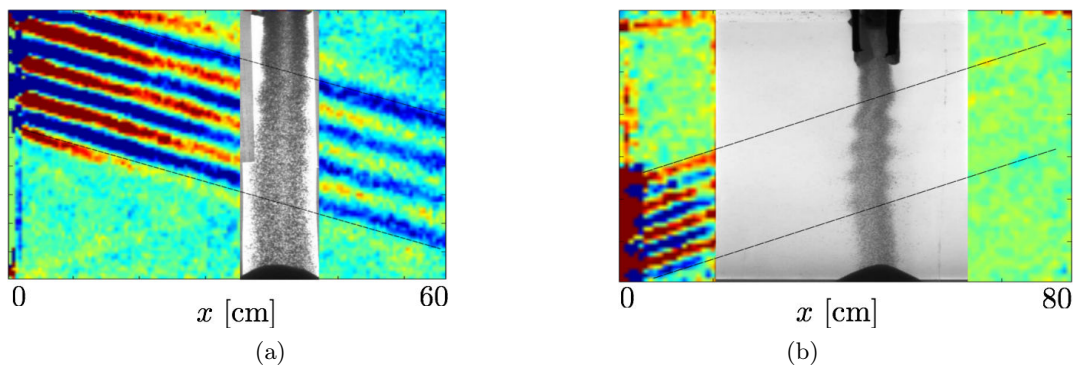


Figure 5.11: View of the wavefield and column of sedimentation particles for two configurations of the wave beam. (a) The wave beam is generated in the upper-left corner and propagates downwards. (b) The wave beam is generated in the lower-left corner and propagates upwards.

5.5.1 Oscillation of the column

In figure 5.9 is shown the column of sediment particles when no internal waves are generated (a), and during the passage of internal waves (b). With blue dashed lines is marked where the wave beam traverses the column. We can observe that the contour of the column changes its shape, in fact, the boundaries oscillate with time. This oscillation is induced by fluid particle motion attached to the wave, and one can see the projection of the wavelength manifested at the boundaries of the column.

The motion of the particles can be also perceived inside the column. In order to study the oscillation of the column of particles, we measured the concentration c of particles for different regions of the column. This is performed by selecting a square region of 50×50 pixels, within the column. Then, a spatial average of the intensity in the square is performed for each time. This measurement is performed in three regions of the column, which

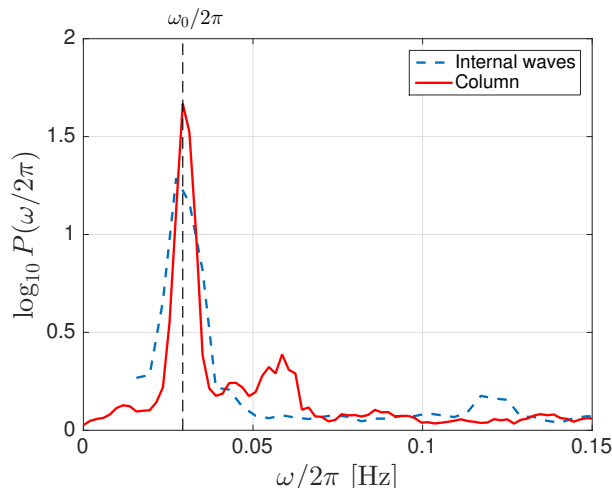


Figure 5.12: Blue dashed line: temporal spectrum of the evolution of $\ln(I_c/I_0)$, for the experiment shown in figure 5.10. The signal corresponds to the intensity taken in the center square. In addition, the red line shows the internal wave spectral content.

we name, top, center and bottom, indicated with three squares at the top, center and at the bottom respectively in figure 5.9(b). Figure 5.10 shows the evolution of $\ln(I_c/I_0)$ for these three regions. The evolution of the concentrations is sinusoidal, and, in a rather counter-intuitive way, the oscillations are present in the three regions of the column, including the regions outside the wave beam. That is, the perturbation propagates inside the column beyond the limits of the wave beam. This effect, we believe, is related to the wake generated by the particles: each particle is slightly entrained by the wake of the particle below, so that the motion of a particle is perceived by the particle above, and the dynamics can be transmitted upwards in the column.

It is important to mention, that the same experiment has been performed by generating a wave beam propagating from the lower-left corner to the upper-right corner as shown in figure 5.11(b). These two configurations have been used to generate a vertical component of the group velocity with the same and opposite direction with respect to the sedimentation velocity. We observe the same oscillatory effect over the column for these two configurations. The column presents oscillations on top of the wave beam even when the phase velocity is upwards. This effect is in agreement with the interpretation that the particle wake is the responsible of causing the upwards motion beyond the limits of the beam.

Spectral analysis

In order to obtain the frequencies related to the oscillations of the concentration of particles in the column, we computed the time spectrum of these signals. In figure 5.12 is shown an example of the spectrum of the evolution of the concentration of particles measured in the center square of the column. In addition, the wave spectrum computed from the Schlieren signal is plotted in the same graph. We can observe that the column oscillates at the wave frequency ω_0 , that is, the particles act as a passive scalar in the stratified medium where the waves propagate. Nevertheless, the wave frequency ω_0 is not the only frequency present in the column spectrum, another frequency always appears which we will call natural frequency ω_c of the column, in indication that this frequency is related to the group behavior of the particles in the column. This frequency is present in the top, center

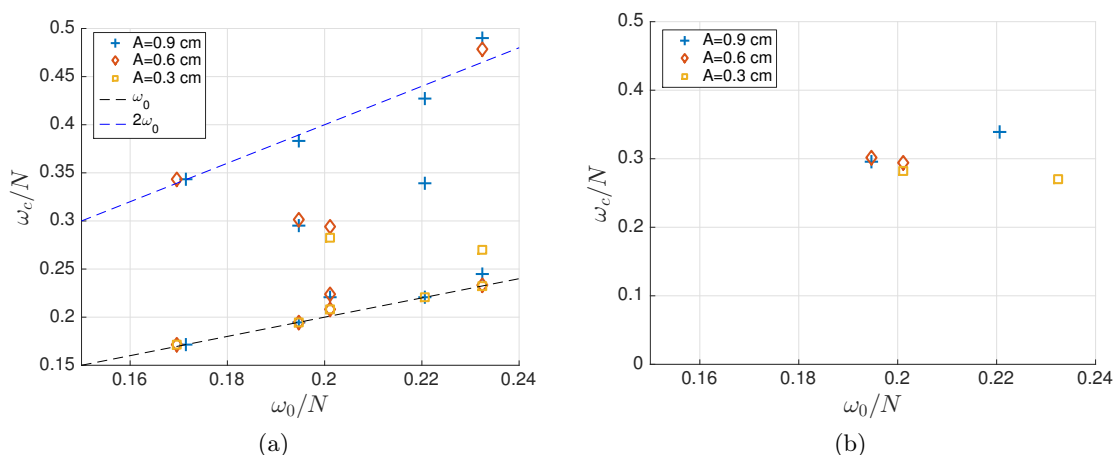


Figure 5.13: Main frequencies present in the spectral content of the column oscillation as a function of ω/N , where $N = 0.85 \text{ rad}\cdot\text{s}^{-1}$. The experiment is repeated for different amplitudes of the generator, that is, $A = 0.3 \text{ cm}$, $A = 0.6 \text{ cm}$ and $A = 0.9 \text{ cm}$. (a) Shows all the main frequencies found in the spectrum. (b) shows only the frequencies that are not present in the wave spectrum.

and bottom regions of the column.

This experiment has been performed for different experimental parameters. In particular, we changed the amplitude A and the forcing frequency of the generator ω_0 for different experiments. These experiments have been performed with the GOAL generator described in section 2.1.3. The buoyancy frequency was kept constant, $N = 0.85 \text{ rad}\cdot\text{s}^{-1}$, as well as the characteristics of the column. Each pair (A, ω_0) represents a different experiment. In figure 5.13(a) are shown the frequencies present in the column for each experiment (A, ω_0) . We can notice that the forcing frequency is present for all experiments. For the experiments with larger amplitude, $A = 0.9 \text{ cm}$, the first harmonic is always present.

If we suppress the frequencies shown in figure 5.13(a) that are present simultaneously in the column and in the wave spectrum (forcing frequency ω_0 and harmonics), we obtain the graph shown in figure 5.13(b). We observe the appearance of a natural frequency ω_c independent from the forcing frequency ω_0 . The variations in the value of this natural frequency, is probably related to the difficulty in repeating the exact same column between two experiments. We observe that the natural frequency appears mostly for large amplitudes of the wave, that is, for experimental configurations in which non-linearities are more important.

It is important to mention that when this procedure is applied to the experiments with $N = 1.1 \text{ rad}\cdot\text{s}^{-1}$, the natural frequency of the column is not observed. We have not yet an interpretation of this observation.

5.5.2 Displacement of the column

In addition to the oscillation of the column, we have observed that the column of particles shifts its position with respect to its equilibrium position (position of the column when no waves are present) as shown in figure 5.14. We will denote δx the length of displacement in the horizontal, which is defined as the maximum incursion of the edge of the column out of its equilibrium position. In order to measure δx we used a boundary detection algorithm. The boundaries of the column are defined by a threshold in the gradient of

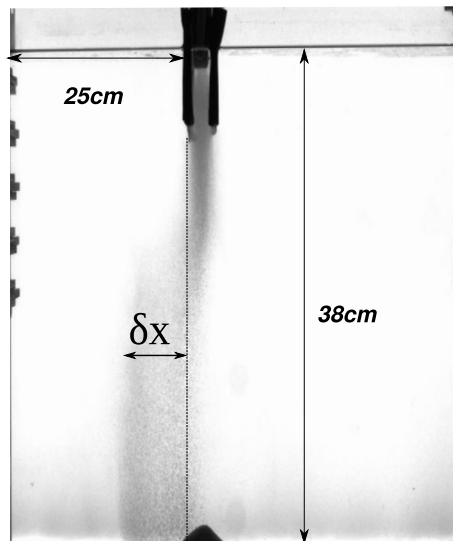


Figure 5.14: Front view of the column when it is displaced. The maximal displacement δx will be defined as the maximal horizontal position where the edge of the column moves away from its equilibrium position.

luminosity between the background screen and the column. The precision of the detection of the boundaries rely on an iterative algorithm which optimizes the boundary detection in each step by imposing a more accurate threshold in the gradient of luminosity, taking into account the position of the boundaries in the previous step. An example of the boundaries detection is shown in figure 5.15. The outcome is a 2D matrix indicating where the column is located.

The detection of the boundaries of the column allows to track the column in time. If we compute the difference between the position of the column at equilibrium at every moment, we can measure how much the position of the edges of the column changes in time for all vertical positions z , that is, $\delta x(z, t)$.

Relation between displacement and forcing frequency

In order to observe the effect of the forcing frequency, ω_0 , on the displacement of the column, we fixed the buoyancy frequency at $N = 1.1 \text{ rad}\cdot\text{s}^{-1}$ and the amplitude of the generator, $A = 0.9 \text{ cm}$. We will use the generator in the configuration so that the waves go downwards. An example of the displacement of the column as a function of time, $\delta x(z, t)$, is shown in figure 5.16. During the first 200 s the column boundary oscillates around the equilibrium position. The oscillations are mostly produced in the region where the wave beam passes through the column, nevertheless, there are also oscillations present above this section of the column. The oscillations are visible and marked by red and black stripes. The slope of these stripes correspond to the group velocity \mathbf{c}_g of the waves. After 200 s the column begins to deform in the region of the wave beam. The displacement rises the column through the oscillations (that are still present after the displacement process begins), and therefore the upper limit of the displacement of the column is located above the upper limit where the wave beam passes through the column. The largest displacement is reached in the region of the wave beam, in this case $\delta x = 3 \text{ cm}$ in the direction of the wave generator. This procedure has been repeated for experiments presenting different forcing frequency ω_0 . The sign of the displacement is measured following the x coordinate direction, positive values of δx indicate that the column deforms away from the wave

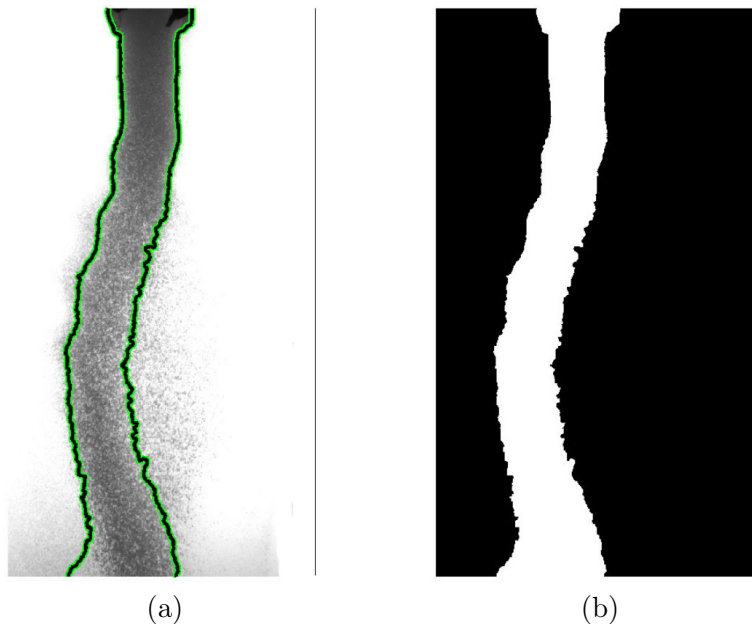


Figure 5.15: Example of the boundary detection algorithm for the column of sedimentation particles. (a) With a green line is indicated the localization of the boundaries. (b) Outcome of 2D matrix indicating where the column is located.

generator, and for negative values, the column deforms toward the wave generator. The displacement is measured 750 s after the wave generator is started (around 25 periods of the wave). In figure 5.17(a) is shown $\delta x/d_c$ as a function of ω_0/N , where d_c is the size of the column. The displacement is always negative, that is, toward the wave generator. For small values of ω_0/N the displacement of the column is small. The displacement increase as the frequency increases, until $\omega_0/N = 0.2$, from where the displacement decreases for larger values of ω_0/N . In order to study the dependency of the displacement of the column with respect to the frequency only, it is important to notice that the amplitude of the waves is not equal between experiments with different forcing frequency, given that the amplitude of the waves depend on the amplitude of the wave generator and on the forcing frequency ω_0 . Therefore, we defined $\delta x'$ as the displacement of the column corrected by a factor $(1 - (\omega_0/N)^2)/\omega_0$. This correction comes from the fact that the amplitude of the internal waves will be $A_{IW} = A \cdot \omega_0 \cdot \cos \beta$, where $\cos \beta = 1 - (\omega_0/N)^2$, is a term related to the transfer of energy of the wave generator for different orientations of the wave beam. In figure 5.17(b) is shown $\delta x'/d_c$ as a function of ω_0/N . The correction does not strongly modify the dependency of δx with ω_0/N , nevertheless the value of ω_0/N where the displacement is maximal slightly increases.

The fact that δx depends of ω , with a maximal value, is reminiscent of a resonance phenomena.

We will now present the displacement results corresponding to a weaker buoyancy frequency, $N = 0.85 \text{ rad}\cdot\text{s}^{-1}$. In figure 5.18 is shown δx as a function of ω_0/N for several values of the amplitude of the wave generator A . Figure 5.18(a) shows this result for the generator configuration in which the wave beam goes downward, whereas figure 5.18(b) shows the result for the wave beam going upwards. We can observe that for the values of ω_0/N explored in this experiment we do not observe a bell shaped dependency of the displacement with the frequency, as observed in the experiment with $N = 1.1 \text{ rad}\cdot\text{s}^{-1}$. Nevertheless, we observe that for the largest amplitude of the wave generator $A = 0.9 \text{ cm}$

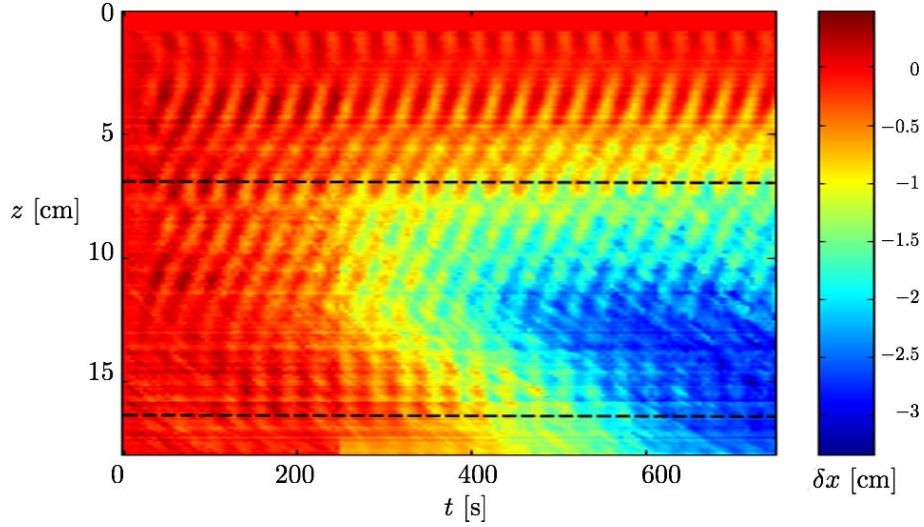


Figure 5.16: Displacement of the left boundary of the column for all vertical locations as a function of time, $\delta x(z, t)$. The colormap indicates the displacement in cm. With two horizontal black dashed line is represent the position where the wave beam passes through the column. For this experiment $A = 0.9$ cm and $N = 1.1$ rad·s⁻¹.

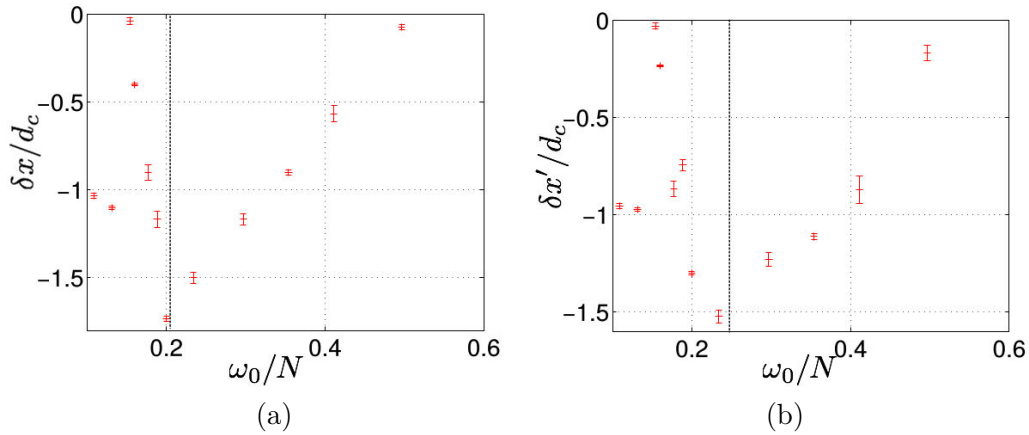


Figure 5.17: (a) Maximal displacement of the column $\delta x/d_c$ as a function of ω_0/N , where d_c is the size of the column. (b) The displacement of the column is corrected by a factor in consequence of the dependency of the internal wave amplitude with the frequency, that is, $\delta x' = \delta x(1 - (\omega_0/N)^2)/\omega_0$. For this experiment $A = 0.9$ cm and $N = 1.1$ rad·s⁻¹.

the displacement increases for large values of ω_0/N . This indicates the possibility of having a resonance effect for higher values of ω_0/N . This values have not been explored because of experimental limitations in the geometrical configuration.

It is useful to study the displacement of the column through its displacement velocity in the horizontal direction, u_c . In order to estimate u_c we measured the displacement of the boundaries of the column as a function of time. In figure 5.19(b) is shown the variation in the horizontal position of the boundaries of the column for several vertical locations of the column (indicated in figure 5.19(a)). One can observe that the slope of the evolution of the displacement changes slightly in time. We can estimate the mean displacement velocity of the boundaries by averaging in time u_c for the different selected vertical locations. From this, we extract the value of the maximal displacement velocity of the column $\max(u_c)$.

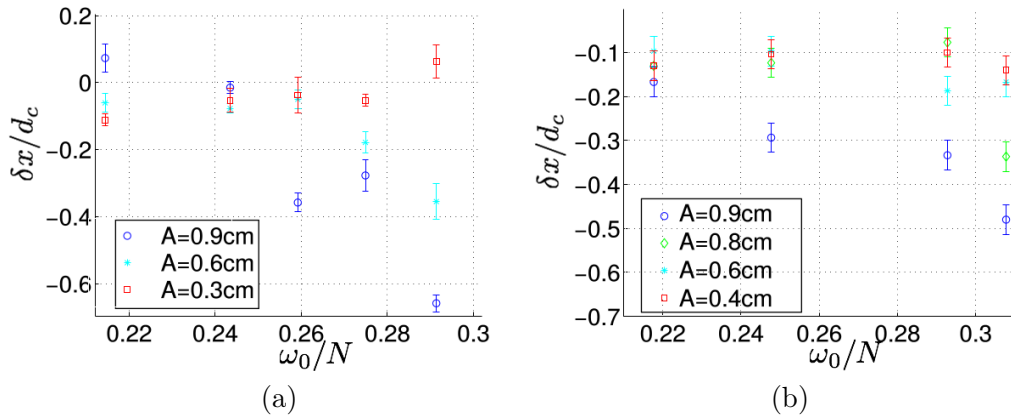


Figure 5.18: Displacement of the column $\delta x/d_c$ as a function of ω_0/N , where d_c is the size of the column. (a) The wave beam propagates downward. (b) The wave beam propagates upward. For this experiment $N = 0.85 \text{ rad}\cdot\text{s}^{-1}$.

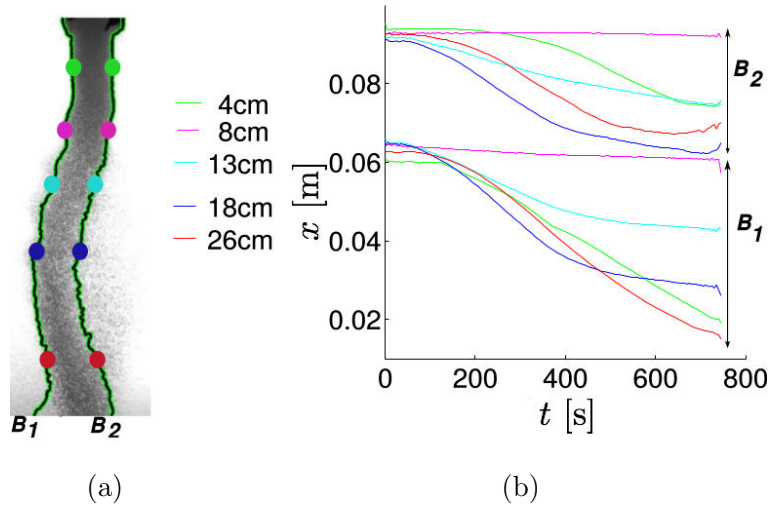


Figure 5.19: Evolution of the horizontal position of the boundaries for several vertical locations. (a) Shows the positions in the boundaries where the horizontal displacement is measured. (b) Evolution of the horizontal displacement of the boundaries for several vertical locations indicated in (a).

This procedure has been repeated for experiments with different forcing frequency ω_0 . In figure 5.20 is shown $\max(u_c)/w_s$ as a function of ω_0/N , where w_s is the sedimentation velocity, and $N = 1.1 \text{ rad}\cdot\text{s}^{-1}$. We observe that the largest displacement velocity, $\max(u_c)$ (which is 10% of w_s), is found at $\omega_0/N = 0.2$, and this value decreases as ω_0/N departs from 0.2. The maximal displacement velocity of the boundaries of the column is found at the same frequency where the horizontal displacement δx is the largest (see figure 5.17(a)).

5.6 Drift generated by internal waves

In order to estimate if net flux exists when an internal wave propagates, we will estimate the Lagrangian drift velocities. The non-dimensional Navier-Stokes equations for a stratified fluid in the Boussinesq approximation allows to expand the streamfunction in terms of

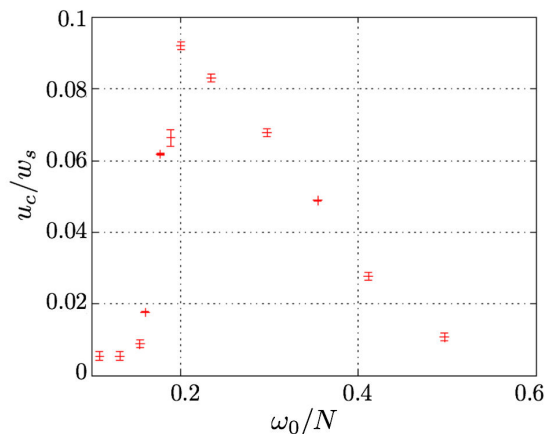


Figure 5.20: Horizontal displacement velocity of the column, u_c/w_s as a function of ω_0/N , where w_s is the velocity of sedimentation of the particles. For this experiment $N = 1.1 \text{ rad}\cdot\text{s}^{-1}$.

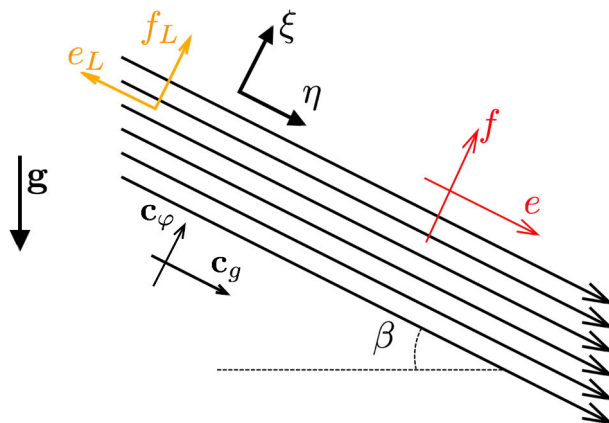


Figure 5.21: System description of a propagating plane wave in the direction of the velocity group, \mathbf{c}_g , with an angle β with respect to the horizontal. The coordinates (η, ξ) attached to the wave are indicated, as well as the velocity components (e, f) in these directions respectively. The direction of the acceleration of the gravity is also indicated.

the Froude number $Fr = U/Nh$, where U is the characteristic velocity, N the buoyancy frequency and h a characteristic vertical length. It has been shown that at first order in an expansion in the Froude number ($Fr \ll 1$ for our experiments), the Lagrangian, \mathbf{u}_L and the Eulerian, \mathbf{u} , velocities are connected through the relationship [73]

$$\mathbf{u}_L(\mathbf{x}, t) = \mathbf{u}(\mathbf{x}, t) + \mathbf{u}_S, \quad (5.5)$$

where the Stokes drift \mathbf{u}_S is defined,

$$\mathbf{u}_S = \nabla \mathbf{u}(\mathbf{x}, t) \cdot \int_0^t \mathbf{u}(\mathbf{x}, t') dt'. \quad (5.6)$$

We will study in particular, the Lagrangian drift generated by a plane wave propagating in a linearly stratified fluid with constant buoyancy frequency, N . In the coordinate system (η, ξ) , a plane wave propagates with group velocity \mathbf{c}_g in the η direction and phase velocity \mathbf{c}_φ in the ξ direction, as shown in the figure 5.21. The wave described by a streamfunction

in this coordinate system will be,

$$\psi = \Psi_0 D_p(\eta) \cos(|\mathbf{k}| \xi - \omega t), \quad (5.7)$$

where $D_p(\eta)$ is a term representing viscous dissipation, that is,

$$D_p(\eta) = e^{-\Lambda \eta}, \quad (5.8)$$

where $\Lambda = \frac{\nu |\mathbf{k}|^3}{2N \cos \beta}$, ν is the kinematic viscosity, and $\omega/N = \sin \beta$. $D_p(\eta)$ preferentially attenuates the higher wavenumbers (or shorter wavelengths).

The Stokes drift velocity defined in equation (5.6), can be rewritten in terms of the streamfunction ψ . In the coordinate system attached to the wave, (η, ξ) , the velocity is, $\mathbf{u} = (-\psi_\xi, \psi_\eta)$. We will name the velocities along the (η, ξ) coordinates, respectively (e, f) . Therefore, the Stokes drift velocity is expressed by the relation,

$$e_S = \psi_{\xi\eta} \int_0^t \psi_\xi dt' - \psi_{\xi\xi} \int_0^t \psi_\eta dt', \quad (5.9)$$

$$f_S = -\psi_{\eta\eta} \int_0^t \psi_\xi dt' + \psi_{\eta\xi} \int_0^t \psi_\eta dt'. \quad (5.10)$$

By performing the time average over a period of the wave, $T = 2\pi/\omega$, to equation (5.5), we obtain that the period-averaged Stokes drift is equal to the period-averaged Lagrangian drift, that is,

$$\langle \mathbf{u}_L \rangle_T = \langle \mathbf{u} \rangle_T + \langle \mathbf{u}_S \rangle_T \quad (5.11)$$

$$= \langle \mathbf{u}_S \rangle_T \equiv \frac{\omega}{2\pi} \int_0^{2\pi/\omega} \mathbf{u}_S dt, \quad (5.12)$$

since the Eulerian velocity is periodic and therefore has zero mean.

The velocity components averaged over a period of the wave, in terms of the streamfunction are,

$$\langle e_S \rangle_T = 0, \quad (5.13)$$

$$\langle f_S \rangle_T = \frac{\Psi_0^2 D_p^2 |\mathbf{k}| \Lambda^2}{\omega}. \quad (5.14)$$

The first order Stokes drift estimation for a dissipating plane waves gives us a zero drift in the direction along the beam, and a non-zero drift in the direction of \mathbf{c}_φ , as previously computed by Hazewinkel [39]. In order to estimate how the Stokes drift evolves within a wave period, we come back to the Lagrangian drift (equation (5.5)). The Lagrangian drift written in terms of the streamfunction is,

$$e_L(\eta, \xi, t) = -\psi_\xi + \psi_{\xi\eta} \int_0^t \psi_\xi dt' - \psi_{\xi\xi} \int_0^t \psi_\eta dt', \quad (5.15)$$

$$f_L(\eta, \xi, t) = \psi_\eta - \psi_{\eta\eta} \int_0^t \psi_\xi dt' + \psi_{\eta\xi} \int_0^t \psi_\eta dt'. \quad (5.16)$$

For the plane wave defined in equation (5.7), the Lagrangian drift is,

$$e_L(\eta, \xi, t) = \Psi_0 D_p |\mathbf{k}| \sin(|\mathbf{k}| \xi - \omega t) - \frac{\Psi_0^2 D_p^2 |\mathbf{k}|^2 \Lambda}{\omega} \sin(\omega t), \quad (5.17)$$

$$f_L(\eta, \xi, t) = -\Psi_0 D_p \Lambda \cos(|\mathbf{k}| \xi - \omega t) + \frac{\Psi_0^2 D_p^2 |\mathbf{k}| \Lambda^2}{\omega} (1 - \cos(\omega t)). \quad (5.18)$$

The results presented in equation (5.13) and (5.14) can be obtained by averaging equations (5.17) and (5.18) over $t = 2\pi/\omega$.

The intensity of the drift generated by the wave will depend on the position (η, ξ) and on time, t . By performing the spatial average over a wavenumber, $\lambda = |\mathbf{k}|/2\pi$ in the direction ξ , that is,

$$\langle e_L \rangle_\lambda = \frac{1}{\lambda} \int_0^\lambda e_L(\eta, \xi', t) d\xi', \quad (5.19)$$

$$\langle f_L \rangle_\lambda = \frac{1}{\lambda} \int_0^\lambda f_L(\eta, \xi', t) d\xi', \quad (5.20)$$

we can estimate the drift generated by the wave in average, at any vertical position.

We will now be interested in estimating the Lagrangian drift produced in average, after an arbitrary time τ ,

$$\langle e_L \rangle_\tau = \frac{1}{\tau} \int_0^\tau e_L(\eta, \xi, t') dt', \quad (5.21)$$

$$\langle f_L \rangle_\tau = \frac{1}{\tau} \int_0^\tau f_L(\eta, \xi, t') dt'. \quad (5.22)$$

$$(5.23)$$

When performing the spatial average over $\lambda = |\mathbf{k}|/2\pi$ in the ξ direction, and the temporal average over τ , together we obtain,

$$\langle e_L \rangle_{\lambda, \tau} = \frac{1}{\tau\lambda} \int_0^\lambda \int_0^\tau e_L(\eta, \xi, t) dt d\xi, \quad (5.24)$$

$$\langle f_L \rangle_{\lambda, \tau} = \frac{1}{\tau\lambda} \int_0^\lambda \int_0^\tau f_L(\eta, \xi, t) dt d\xi. \quad (5.25)$$

For the plane wave these relations become,

$$\langle e_L \rangle_{\lambda, \tau} = \frac{\Psi_0^2 D_p^2 |\mathbf{k}|^2 \Lambda}{\omega^2 \tau} (\cos(\omega\tau) - 1), \quad (5.26)$$

$$\langle f_L \rangle_{\lambda, \tau} = \frac{\Psi_0^2 D_p^2 |\mathbf{k}| \Lambda^2}{\omega} \left(1 - \frac{\sin(\omega\tau)}{\omega\tau} \right). \quad (5.27)$$

The horizontal drift, $\langle e_L(\eta) \rangle_{\lambda, \tau}$, is negative for all $\tau \neq 2\pi n$, and null for $\tau = 2\pi n$. The vertical drift, $\langle f_L(\eta) \rangle_{\lambda, \tau}$, is positive for all $\tau > 0$, where n is an integer number. This result is illustrated in figure 5.21, where two orange arrows indicate the components in the (η, ξ) coordinates, of the Lagrangian drift.

5.6.1 Analysis of the Lagrangian drift

We will study the temporal dependance of the Lagrangian drift within a period of the wave, for which we will despise for the moment the amplitude of the drift. We define a normalized drift averaged in time and space as,

$$\hat{e}_L = \frac{\cos(\omega t) - 1}{\omega t}, \quad (5.28)$$

$$\hat{f}_L = 1 - \frac{\sin(\omega t)}{\omega t}. \quad (5.29)$$

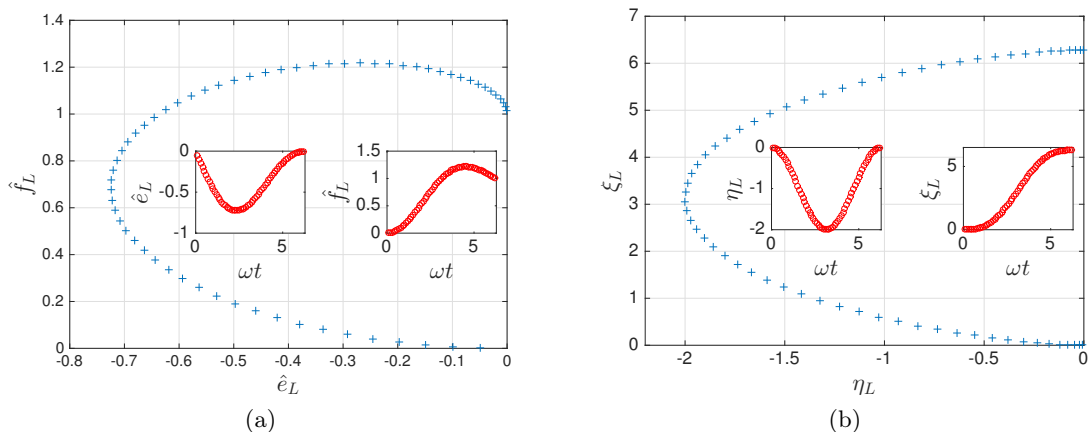


Figure 5.22: (a) Phase portrait of \hat{f}_L as a function of \hat{e}_L . (b) Phase portrait of η as a function of ξ . Where $\omega t \in [0, 2\pi]$, and $\omega t = 0$ corresponds to $(\hat{e}_L, \hat{f}_L) = (0, 0)$ for (a) and, $(\eta_L, \xi_L) = (0, 0)$ for (b). The inset graphics show the evolution in time of all the quantities.

In figure 5.22 is shown the phase portrait of the velocities \hat{e}_L and \hat{f}_L (a), and the phase portrait of the drift positions (b), generated by \hat{e}_L and \hat{f}_L . The initial velocities and positions correspond to $(\hat{e}_L, \hat{f}_L) = (0, 0)$ and $(\eta, \xi) = (0, 0)$ respectively. After a period of the wave is completed, the time averaged drift velocity is null for \hat{e}_L and positive for \hat{f}_L . Similarly, after a period of the wave, the mean position is, $\eta_L = 0$ and $\xi_L > 0$. The displacement ξ_L will be positive for all times. On the other hand η_L will be negative for all times different than a complete period of the wave.

5.6.2 Drift estimation for experiments

In order to estimate the mean motion of a particle when passing through a wave beam. We will make the assumption that the drift of a particle will be related to the intensity of the drift generated by these waves times the time the particle stays in the wave beam before sedimentation.

Order of magnitude of the intensity of the Lagrangian drift for experiments

We first compute an order of magnitude of the Lagrangian drift velocities of the wave (equations (5.26) and (5.27)). In these equations, we can notice that the factor $\Psi_0^2 D_p^2 |\mathbf{k}| \Lambda / \omega$ repeats in both equations. Therefore, neglecting the temporal dependency, the ratio between the Lagrangian drift in the direction η and in the direction ξ is simply k/Λ .

The distance between the wave generator and the column is the same for all the beam in the direction η , given that both, the wave generator and the column are extended in the same direction, z . Therefore the dissipation of the wave, given by $D_p(\eta) = e^{-\Lambda \eta}$, will be equal at all the vertical locations of the column, and so will it be the intensity of the wave. For simplicity, we will assume that D_p is constant within the column, given that the column is thin enough with respect to the dissipation length, that is, $d_c \ll 1/\Lambda$. The velocity of the wave at the position of the column is:

$$e(\eta_c) = \Psi_0 D_p(\eta_c) |\mathbf{k}|, \quad (5.30)$$

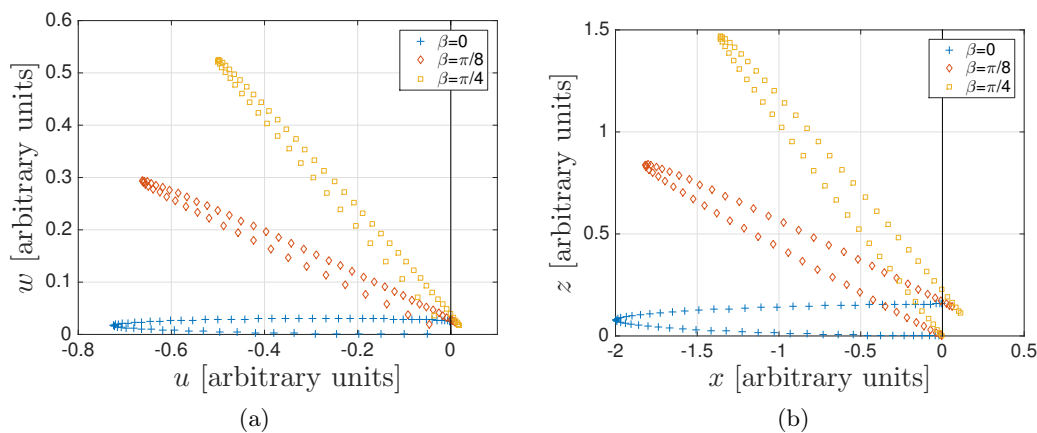


Figure 5.23: Phase portrait of the position (a) and the velocity (b) of the averaged Lagrangian drift in (x, z) coordinates, where the initial position and velocity are respectively $(x, z) = (0, 0)$ and $(u, w) = (0, 0)$. This drifts are plotted for several angle of propagation of the wave, β . The relative intensity between the drift in the directions (x, z) is computed taking into account the experimental parameters (equation (5.32)).

where η_c is the position of the column along the coordinate η . The intensity of the averaged Lagrangian drift $\langle e_L \rangle_{\lambda, t}$ becomes,

$$\frac{\Psi_0^2 D_p^2 |\mathbf{k}|^2 \Lambda}{\omega} = (e(\eta_c))^2 \frac{\Lambda}{\omega}, \quad (5.31)$$

For the characteristic experimental parameters used in the experiments presented in this chapter,

$$\frac{\Psi_0^2 D_p^2 |\mathbf{k}|^2 \Lambda}{\omega} \approx \frac{1}{10} e(\eta_c), \quad \text{and} \quad \frac{\Psi_0^2 D_p^2 |\mathbf{k}| \Lambda^2}{\omega} \approx \frac{1}{400} e(\eta_c), \quad (5.32)$$

that is, the intensity of the Lagrangian drift along the direction η and ξ , is roughly 10% and 0.25% respectively, of the wave velocity intensity, $e(\eta_c)$.

Trajectory of the Lagrangian drift for experiments

Taking into account the relative intensity of the Lagrangian drift velocity in the directions (η, ξ) (equation (5.32)) for our experimental parameters, we will estimate the displacement generated by the drift in the (x, z) coordinate system, by rotating counterclockwise the velocity obtain in equations (5.28) and (5.28) by an angle $\beta = \sin^{-1}(\omega/N)$. The variation in the angle β implies a variation of the frequency ω and therefore a difference in the amplitude of the drift, nevertheless, this variation will represent a small difference, for the angles explored here and will be therefore neglected. In figure 5.23 is shown the phase portrait of the velocities (u, w) (a) and the positions (x, z) (b). The initial velocities and positions correspond to $(u, w) = (0, 0)$ and $(x, z) = (0, 0)$. The Lagrangian drift is estimated for several propagating angles β . We observe that the drift will be positive in the z direction for all times and all angles β . The drift in x will be principally negative, and it will be positive only for a small interval of time, and for small angles β practically never. The behavior for the Lagrangian velocity drift is equivalent to the Lagrangian spatial drift, as shown in figure 5.23(a).

Lagrangian drift for different sedimentation velocity

As mentioned we will estimate the particle drift as proportional to the fluid drift intensity times the interval of time that the particle spends in the wave beam. The time the particle stays in the beam will depend on the sedimentation velocity. The characteristic time that the particle will spend in one wavelength is $\tau_s = \lambda^g/w_s$, where λ^g is the vertical wavelength of the wave generator, and w_s the sedimentation velocity of the particle. Where the vertical drift, smaller than the sedimentation velocity, is neglected.

If the particle does not settle and stays in the fluid, each period of the wave the particle will be dragged upwards and slightly to the right. On the other hand, if the particle sediments very fast, then it will not spend enough time in the wave to feel the drift generated by the wave. In the intermediate case, the most probable case is that the particles perceive a drift towards the upper left direction. How much this drift affects the motion of the particle, will depend on the time the particle stays in the wave, and the magnitude of the drift. The largest drift to the left will be generated when the particle stays a time τ in the wave, so that $\omega\tau \sim \pi$. If the particle stays more time, let us say more than several periods $T = 2\pi/\omega$ of the wave, then we can decompose this time in the form, $\tau = nT + \tau'$, where n is an integer number and $\tau' < T$. The term nT adds a drift to the right (which increases linearly with n), while τ' adds a drift to the left. We neglect the upwards drift velocity, since experimentally this velocity is always smaller than the sedimentation velocity of the particles by several orders of magnitude. The time the particle stays in the wave depends, as mentioned, on w_s , whereas w_s depends on the stratification, characterized here by the buoyancy frequency N . In addition, the frequency ω plays a part as crucial as the time τ , as the horizontal drift is largest for $\omega\tau \sim \pi$.

Comparison with sedimentation velocity and frequency

We will use the hypothesis mentioned previously to make an attempt to predict the dependency of the displacement of the column with the forcing frequency ω_0 .

Two sedimentation velocities concerned in the experiments performed in this chapter, $w_s = 0.14$ cm/s for $N = 0.85$ rad·s⁻¹, and $w_s = 0.09$ cm/s for $N = 1.1$ rad·s⁻¹. The time the particles spend in the wave is, $\tau = 28$ s for $N = 0.85$ rad·s⁻¹, and $\tau = 44$ s for $N = 1.1$ rad·s⁻¹. We explored a range of frequencies ω between 0.17 s⁻¹ and 0.25 s⁻¹ (T between 25 s and 37 s) for $N = 0.85$ rad·s⁻¹, and between 0.12 s⁻¹ and 0.6 s⁻¹ (T between 10 s and 50 s) for $N = 1.1$ rad·s⁻¹.

In figure 5.24 is shown the computed horizontal velocity and horizontal position drift as a function of ω_0/N for two buoyancy frequencies, where the parameters are set equal to the experimental parameters. Figures (a) and (b) correspond to the experiment with $N = 1.1$ rad·s⁻¹ and therefore smallest sedimentation velocity. We can observe the horizontal velocity and horizontal position drift oscillate between negative values, and for some reduced intervals of ω_0/N slightly positive values. The amplitude of the oscillations decreases for increasing time. The largest negative drift is found at $\omega_0/N \approx 0.2$. On the other hand, the computed drift for the experimental parameters corresponding to the experiment with $N = 0.85$ rad·s⁻¹, show less number of oscillations for the same forcing frequency interval.

We have neglected that the intensity of the drift will decrease for decreasing forcing frequency, as the intensity of the wave will be $u_o \propto A\omega \cos\beta$. The corrected drift will present slightly smaller values for ω_0/N small, and slightly larger values for ω_0/N large.

When comparing the computed drift with the experimental drift, we observe for the experiment with $N = 1.1$ rad·s⁻¹, the horizontal position and velocity displacement of the

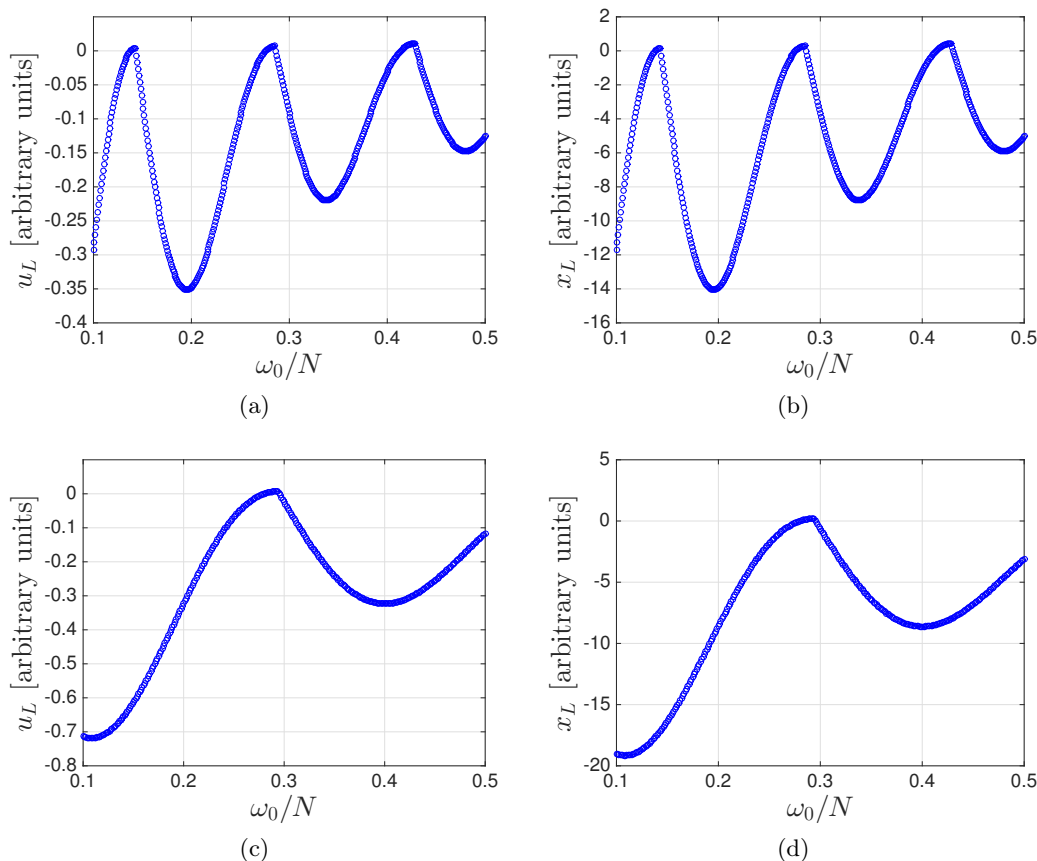


Figure 5.24: Horizontal velocity ((a) and (c)) and horizontal position ((b) and (d)) drift as a function of ω_0/N . Figures (a) and (b) correspond to the experiment with buoyancy frequency $N = 1.1 \text{ rad}\cdot\text{s}^{-1}$. Figures (c) and (d) correspond to the experiment with buoyancy frequency $N = 0.85 \text{ rad}\cdot\text{s}^{-1}$.

column is maximal for $\omega_0/N \approx 0.22$ (figures 5.17 and 5.20). For smaller values of ω_0/N we observe a decrease of the displacement followed by an increase. For larger values of ω_0/N the drift decreases continually. The computed drift presents agreement with the maximal displacement frequency, and for smaller values of ω_0/N . On the other hand, although the displacement decreases in the computed drift, the oscillations are not measured in experiments. For the experiment with $N = 0.85 \text{ rad}\cdot\text{s}^{-1}$ the displacement of the column has been studied for the frequency interval $0.2 \lesssim \omega_0/N \lesssim 0.32$. The experiments performed with the upwards and downwards beam do not present much differences. Almost no displacement has been observed with the exception for the largest wave amplitude for values of frequency $\omega_0/N \approx 0.28$. For the computed drift, there will be no difference between considering that the beam propagates upward or downward, as we are only considering the horizontal drift. Contrary to what observed in the experiment, the computed displacement drift will be almost null for $\omega_0/N \approx 0.28$, and will increase for increasing and decreasing values of ω_0/N .

This hypothesis will be further investigated by taking into account the modification of the sedimentation time because of the vertical drift. In addition, we will compute the drift of the particles considering their size and their inertia.

5.7 Conclusions

We have developed a particle injector which allows to generate a column of particles in sedimentation. The column is two-dimensional, conserving the same symmetry as the internal waves. The concentration of particles c in the column and the size of the column can be easily adjusted. The dynamics of the column present a stage in which the concentration of particles is fairly constant.

We observed a dependency of the sedimentation velocity with respect to the buoyancy frequency N . In particular, the sedimentation velocity varies with depth for largest N used, and it remains constant in depth for the smallest N used. The column of particles will not generate any added dissipation to the propagation of the internal plane waves, for the range of concentrations explored in this work.

The waves will generate oscillations of the boundaries of the column and in its inside. The oscillations are mostly induced by the forcing frequency and harmonics. However, in some cases a natural frequency of the column seems to emerge for amplitudes of the wave large enough. The oscillations of the column exceeds the limits of the wave beam. The oscillations are perceived above and below the beam. The upper oscillation, we believe is related to the wake generated by the particles: each particle is slightly entrained by the wake of the particle below, so that the motion of a particle is perceived by the particle above, and the dynamics can be transmitted upwards in the column. This effect is not related to the phase velocity as the same experiment has been performed with the group velocity going upwards and the phase velocity going downwards. We believe that the downwards oscillations, is given by a group behavior of the particles that manifests as an elasticity of the column.

In some cases the boundaries of the column oscillate around an equilibrium position, and in some cases the column as a whole is displaced, manifesting a net transport of the settling particles. In particular, the displacement is always towards the source of waves. For a particular value of the buoyancy frequency N we found that the displacement of the column increases when approaching a particular frequency. The fact that the displacement depends of the forcing frequency, with a maximal value, is reminiscent of a resonance phenomena.

We computed the Lagrangian drift generated by unbounded internal plane waves propagating in a stratified fluid. We considered that the drift of the particles is given by the intensity of the wave induced drift, times the time the particles stays inside the wave beam. We obtained a result that could explained the displacement direction of the column. For our experimental parameters we attempt to estimate the frequency dependency of the displacement of the column and observed some qualitative agreements.

The further investigation will be based on performing a more extensive study of the effect on the suspension time given by the vertical Lagrangian drift generated by the waves. In addition, the particle size and inertia will be included in the estimation of the particle drift.

Conclusion

The principal objective of this work was to understand different mechanisms related to the transport properties of internal gravity waves. In a first stage we studied the bed load motion induced by internal gravity waves.

- In order to produce a large shear stress over settled grains, we have performed several explorative experiments contemplating different configurations of both the wave type, and the disposition of the particles. For the experiments explored, we have not observed bed load transport of particles, indicating that overcoming the threshold of particles motion is not a trivial task in our experimental conditions.
- In the particular case where a mountain of particles in the bottom of the tank was built, we observed a change in the shape of a mountain after the passage of a vertical mode wave, in particular, when the non-linearities in the wavefield increased. Nevertheless, we inferred that the change of shape and size of the mountain is a consequence of avalanches in the slope of the mountain and compaction in its interior.
- The particular intense focalization produced by a critical reflection was used to generate strong shears in a solid boundary and therefore generate transport of settled particles. Despite the fact that no particle motion was produced we observed an intensification of the mean velocities near the boundary.
- We performed high resolution measurements of internal waves near-critical reflections, in order to determine the conditions in which the reflection process will increase the shear stress σ at the boundary, enough to generate erosion of grains disposed in a bed.
- We have developed, in a collaborative work, and applied to our experimental measurements, an image processing technique which allows to decompose the wavefield in the various wave components involved in an internal wave reflection by using its particular spectral content. This method minimizes the boundary effects in the field of view and satisfactorily decomposes the waves involved. It allows to decompose the wavefield in as many modes as desired. This feature has been used in order to identify for the first time when a near critical reflection involves two (incident and reflected) or three (incident, reflected upward and reflected downward) wave components. This allows to identify not only the angle interval $\beta - \gamma$ where the linear theory fails in predicting a single reflected wave, but also allows to have a precise identification of the reflected wave in this interval composed by both the upward and downward reflected wave.

- The high resolution measurements of the velocity field of an internal wave reflection near the slope, together with the capability of decomposing the wavefield in a incident and reflected wave, allowed to compare for the first time experimental results with a theoretical solution of the velocity field near the boundary in an internal wave critical reflection developed by Dauxois & Young. We observed that the theory manages to represent the main features of the velocity field near the boundary.
- Through the theoretical solution of the velocity field in a critical reflection, we estimated the shear stress σ as a function of the experimental parameters. The shear stress obtained experimentally is in good agreement with the theory for the experimental parameters explored in this work. This allows to estimate under which condition erosion in a bed of grains is predicted for a given particle and experimental configuration, as well as for an oceanic situation.

In a second stage we performed experiments in order to study the effect of internal waves over particles in suspension.

- We have developed a particle injector which allows to generate a column of particles in sedimentation, conserving the same symmetry as the internal waves. The concentration of particles in the column and the size of the column can be easily adjusted. The dynamics of the column present a stage in which the concentration of particles is fairly constant.
- The column of particles will not generate any added dissipation to the propagation of the internal plane waves, for the range of concentrations explored in this work.
- The waves will generate oscillations of the boundaries of the column and in its inside. The oscillations are mostly induced by the forcing frequency and harmonics. However, in some cases a natural frequency of the column seems to emerge for large enough amplitudes of the wave.
- The oscillations of the column exceeds the limits of the wave beam. The oscillations are perceived above and below the beam. The upper oscillation, we believe is related to the wake generated by the particles: each particle is slightly entrained by the wake of the particle below, so that the motion of a particle is perceived by the particle above, and the dynamics can be transmitted upwards in the column.
- In some cases we observed that internal waves displace the column, manifesting a net transport of the suspended particles. In particular, the displacement is always towards the source of waves. For a particular value of the buoyancy frequency N we found that the displacement of the column increases when approaching a particular frequency. The fact that the displacement depends of the forcing frequency, with a maximal value, is reminiscent of a resonance phenomena.
- We computed the Lagrangian drift generated by unbounded internal plane waves propagating in a stratified fluid. We considered that the drift of the particles is given by the intensity of the wave induced drift, times the time the particles stays inside the wave beam. We obtained a result that could explained the displacement direction of the column. For our experimental parameters we attempt to estimate the frequency dependency of the displacement of the column and observed some qualitative agreements.

Perspectives

Many questions remain open. In particular, we can highlight what we consider the most relevant.

- Through the comprehensive study of internal waves near-critical reflection we were able to compare our results with a theory for internal waves reflection, and therefore, through this theory interpolate the experimental values to predict erosion of particles. Nevertheless, the experimental conditions required, overpasses the limits of our experimental setups. Performing internal waves reflections in a enlarge setup in order to observe bed load motion would allow to compare experimental values above the threshold motion with the theory of internal wave reflections and the measurements performed in this work.
- For the study of particles in suspension, the further investigation will be based on performing a more extensive study of the effect of the vertical Lagrangian drift generated by the waves over the particle suspension time. In addition, the size and inertia of the particles will be included in the estimation of the particle drift.

This work allowed us to understand the main limitations of transport properties of internal waves generated in laboratory conditions. We observed and measure accurately first time observed processes which may serve to understand the transport of sediments and nutrients in oceanic conditions.

Bibliography

- [1] B. Andreotti, Y. Forterre, and O. Pouliquen. *Granular Media, Between Fluid and Solid*. Cambridge University Press, 2013.
- [2] A. Bianchi, O. Tholosan, J. Garcin, T. Polychronaki, A. Tselepidis, R. Buscail, and G. Duineveld. Microbial activities at the benthic boundary layer in the Aegean Sea. *Progress in Oceanography*, 57(2):219–236, 2003.
- [3] B. Bigot, T. Bonometti, L. Lacaze, and O. Thual. A simple immersed-boundary method for solid-fluid interaction in constant- and stratified-density flows. *Computers & Fluids*, 97:126–142, JUN 25 2014.
- [4] C. E. Bluteau, N. L. Jones, and G. N. Ivey. Dynamics of a tidally-forced stratified shear flow on the continental slope. *Journal of Geophysical Research: Oceans*, 116, NOV 12 2011.
- [5] D. Bogucki, T. Dickey, and L. G. Redekopp. Sediment resuspension and mixing by resonantly generated internal solitary waves. *Journal of Physical Oceanography*, 27(7):1181–1196, JUL 1997.
- [6] G. Bordes. *Interactions non-linéaires d’ondes et tourbillons en milieu stratifié ou tournant*. PhD thesis, ENS de Lyon, JUL 2012.
- [7] B. Bourget. *Ondes internes, de l’instabilité au mélange. Approche expérimentale*. PhD thesis, ENS de Lyon, 2014.
- [8] B. Bourget, T. Dauxois, S. Joubaud, and P. Odier. Experimental study of parametric subharmonic instability for internal plane waves. *Journal of Fluid Mechanics*, 723:1–20, MAY 2013.
- [9] C. Brouzet, T. Dauxois, E. Ermanyuk, S. Joubaud, M. Kraposhin, and I. Sibgatullin. Direct numerical simulation of internal gravity wave attractor in trapezoidal domain with oscillating vertical wall. 2015.
- [10] J. W. M. Bush, B. A. Thurber, and F. Blanchette. Particle clouds in homogeneous and stratified environments. *Journal of Fluid Mechanics*, 489:29–54, AUG 25 2003.
- [11] B. Butman, P. S. Alexander, A. Scotti, R. C. Beardsley, and S. P. Anderson. Large internal waves in Massachusetts Bay transport sediments offshore. *Continental Shelf Research*, 26(17-18):2029–2049, NOV 2006.

- [12] D. A. Cacchione, L. F. Pratson, and A. S. Ogston. The shaping of continental slopes by internal tides. *Science*, 296(5568):724–727, APR 26 2002.
- [13] R. Camassa, S. Khatri, R. M. McLaughlin, J. C. Prairie, B. L. White, and S. Yu. Retention and entrainment effects: Experiments and theory for porous spheres settling in sharply stratified fluids. *Physics of Fluids*, 25(8), AUG 2013.
- [14] Darwin Volcanic Ash Advisory Centre. Report of volcanic eruption: Cordón caulle, chile, june 2011. Technical report, Darwin Volcanic Ash Advisory Centre.
- [15] V. K. Chalamalla, B. Gayen, A. Scotti, and S. Sarkar. Turbulence during the reflection of internal gravity waves at critical and near-critical slopes. *Journal of Fluid Mechanics*, 729:47–68, AUG 2013.
- [16] S. B. Dalziel, G. O. Hughes, and B. R. Sutherland. Whole-field density measurements by ‘synthetic schlieren’. *Experiments in Fluids*, 28(4):322–335, 2000.
- [17] T. Dauxois, C. Brouzet, E. Ermanyuk, S. Joubaud, and I. Sibgatullin. Laboratory and numerical simulation of internal wave attractors and their instability. *Geophysical Research Abstracts*, 2015.
- [18] T. Dauxois, A. Didier, and E. Falcon. Observation of near-critical reflection of internal waves in a stably stratified fluid. *Physics of Fluids*, 16(6):1936–1941, JUN 2004.
- [19] T. Dauxois and W. R. Young. Near-critical reflection of internal waves. *Journal of Fluid Mechanics*, 390:271–295, JUL 10 1999.
- [20] I. P. D. De Silva, J. Imberger, and G. N. Ivey. Breaking of super-critically incident internal waves at a sloping bed. *IUTAM*, 1998.
- [21] E. M. Dewan, R. H. Picard, R. R. O’Neil, H. A. Gardiner, J. Gibson, J. D. Mill, E. Richards, M. Kendra, and W. O. Gallery. MSX satellite observations of thunderstorm-generated gravity waves in mid-wave infrared images of the upper stratosphere. *Geophysical Research Letters*, 25(7):939–942, 1998.
- [22] K. Dragomiretskiy and D. Zosso. Two-Dimensional Variational Mode Decomposition. In E. Bae, T. F. Chan, and M. Lysaker, editors, *Energy minimization methods in computer vision and pattern recognition*, Hong Kong, China, January 13-16 2015.
- [23] M. Dykstra. *Principles of Tidal Sedimentology*. Springer, 2012.
- [24] P. Echeverri, M. R. Flynn, K. B. Winters, and T. Peacock. Low-mode internal tide generation by topography: an experimental and numerical investigation. *Journal of Fluid Mechanics*, 636:91–108, 10 2009.
- [25] G. D. Egbert and R. D. Ray. Estimates of M2 tidal energy dissipation from TOPEX/Poseidon altimeter data. *Journal of Geophysical Research: Oceans*, 106(C10):22475–22502, 2001.
- [26] G. D. Egbert and R. D. Ray. Semi-diurnal and diurnal tidal dissipation from TOPEX/Poseidon altimetry. *Geophysical Research Letters*, 30(17), 2003.
- [27] GD Egbert and RD Ray. Significant dissipation of tidal energy in the deep ocean inferred from satellite altimeter data. *Nature*, 405(6788):775–778, JUN 15 2000.

-
- [28] O. S. Eiff and P. Bonneton. Lee-wave breaking over obstacles in stratified flow. *Physics of Fluids*, 12(5):1073–1086, MAY 2000.
- [29] C. C. Eriksen. Observations of internal wave reflection off sloping bottoms. *Journal of Geophysical Research: Oceans and Atmospheres*, 87(NC1):525–538, 1982.
- [30] A. Fincham and G. Delerce. Advanced optimization of correlation imaging velocimetry algorithms. *Experiments in Fluids*, 29(S):S13–S22, DEC 2000. 3rd International Workshop on Particle Image Velocimetry, SANTA BARBARA, CALIFORNIA, SEP 16-18, 1999.
- [31] A. Folch, L. Mingari, M. S. Osorio, and E. Collini. Modeling volcanic ash resuspension – application to the 14–18 october 2011 outbreak episode in central patagonia, argentina. *Natural Hazards and Earth System Sciences*, 2014.
- [32] J. M. H. Fortuin. Theory and application of two supplementary methods of constructing density gradient columns. *Journal of Polymer Science*, 44(144):505–515, 1960.
- [33] C. Garrett. Internal tides and ocean mixing. *Science*, 301(5641):1858–1859, 2003.
- [34] H. Görtler. Über eine Schwingungserscheinung in Flüssigkeiten mit stabiler Dichteschichtung. *Journal of Applied Mathematics and Mechanics*, 23(2):65–71, 1943.
- [35] L. Gostiaux. *Etude expérimentale des ondes de gravité internes en présence de topographie. émission, propagation, réflexion*. PhD thesis, ENS de Lyon, 2006.
- [36] L. Gostiaux and T. Dauxois. Laboratory experiments on the generation of internal tidal beams over steep slopes. *Physics of Fluids*, 19(2):028102, 2007.
- [37] L. Gostiaux, T. Dauxois, H. Didelle, J. Sommeria, and S. Viboud. Quantitative laboratory observations of internal wave reflection on ascending slopes. *Physics of Fluids*, 18(5), MAY 2006.
- [38] L. Gostiaux, H. Didelle, S. Mercier, and T. Dauxois. A novel internal waves generator. *Experiments in Fluids*, 42(1):123–130, JAN 2007.
- [39] J. Hazewinkel. *Attractores in stratified fluid*. PhD thesis, University of Utrecht, 2010.
- [40] P. Hosegood, J. Bonnin, and H. van Haren. Solibore-induced sediment resuspension in the Faeroe-Shetland Channel. *Geophysics Research Letters*, 31(9), MAY 1 2004.
- [41] G. N. Ivey, K. B. Winters, and I. P. D. De Silva. Turbulent mixing in a sloping benthic boundary layer energized by internal waves. *Journal of Fluid Mechanics*, 418:59–76, SEP 10 2000.
- [42] B. King, H. P. Zhang, and H. L. Swinney. Tidal flow over three-dimensional topography in a stratified fluid. *Physics of Fluids*, 21(11), NOV 2009.
- [43] YV Kistovich and YD Chashechkin. The reflection of beams of internal gravity waves at a flat rigid surface. *PMM Journal of applied Mathematics and Mechanics*, 59(4):579–585, 1995.
- [44] J. M. Klymak, S. Legg, M. H. Alford, M. Buijsman, R. Pinkel, and J. D. Nash. The Direct Breaking of Internal Waves at Steep Topography. *Oceanography*, 25(2):150–159, JUN 2012.

- [45] L. R. M. Maas, D. Benielli, J. Sommeria, and F. P. A. Lam. Observation of an internal wave attractor in a confined, stably stratified fluid. *Nature*, 388(6642):557–561, AUG 7 1997.
- [46] M. Mercier. *Etude expérimentale de la génération de structures linéaires et non-linéaires (solitons, solitons) en milieu stratifié*. PhD thesis, ENS de Lyon, 2010.
- [47] M. J. Mercier, N. B. Garnier, and T. Dauxois. Reflection and diffraction of internal waves analyzed with the Hilbert transform. *Physics of Fluids*, 20(8), AUG 2008.
- [48] M. J. Mercier, D. Martinand, M. Mathur, L. Gostiaux, T. Peacock, and T. Dauxois. New wave generation. *Journal of Fluid Mechanics*, 657:308–334, 2010.
- [49] K. O. Moeller, M. St John, A. Temming, J. Floeter, A. F. Sell, J. Herrmann, and C. Moellmann. Marine snow, zooplankton and thin layers: indications of a trophic link from small-scale sampling with the Video Plankton Recorder. *Marine Ecology Progress Series*, 468:57–69, 2012.
- [50] S. E. Moore and R. Lien. Pilot whales follow internal solitary waves in the South China Sea. *Marine Mammal Science*, 23(1):193–196, JAN 2007.
- [51] D. Moreira, C.G. Simionato, F. Gohin, F. Cayocca, and M. L. C. Tejedor. Suspended matter mean distribution and seasonal cycle in the rio de la plata estuary and the adjacent shelf from ocean color satellite (modis) and in-situ observations. *Continental Shelf Research*, 2013.
- [52] D. E. Mowbray and B. S. H. Rarity. A theoretical and experimental investigation of the phase configuration of internal waves of small amplitude in a density stratified liquid. *Journal of Fluid Mechanics*, 28(01):1–16, 1967.
- [53] J. D. Nash, E. Kunze, J. M. Toole, and R. W. Schmitt. Internal tide reflection and turbulent mixing on the continental slope. *Journal of Physical Oceanography*, 34(5):1117–1134, MAY 2004.
- [54] J. Nycander. Generation of internal waves in the deep ocean by tides. *Journal of Geophysical Research: Oceans*, 110(C10):C10028, 2005.
- [55] G. Oster and M. Yamamoto. Density gradient techniques. *Chemical Reviews*, 63(3):257–268, 1963.
- [56] J. Pedlosky. *Waves in the Ocean and Atmosphere*. Springer, 2003.
- [57] O. M. Phillips. *The Dynamics of the Upper Ocean*. Cambridge University Press, 1966.
- [58] J. Pineda, V. Starczak, J. C. B. da Silva, K. Helfrich, M. Thompson, and D. Wiley. Whales and waves: Humpback whale foraging response and the shoaling of internal waves at Stellwagen Bank. *Journal of Geophysical Research: Oceans*, 120(4):2555–2570, APR 2015.
- [59] L. Quaresma, J. Vitorino, A. Oliveira, and J. C. B. da Silva. Evidence of sediment resuspension by nonlinear internal waves on the western Portuguese mid-shelf. *Marine Ecology*, 246(2-4):123–143, DEC 7 2007.
- [60] X. Riedinger, P. Meunier, and S. Le Dizes. Instability of a vertical columnar vortex in a stratified fluid. *Experiments in Fluids*, 49(3):673–681, SEP 2010.

-
- [61] J. Schmitt, E. Horne, N. Pustelnik, S. Joubaud, and P. Odier. An improved variational mode decomposition method for internal waves separation. In *European Signal Processing Conference (EUSIPCO)*, 2015.
- [62] H. Scolan, E. Ermanyuk, and T. Dauxois. Nonlinear Fate of Internal Wave Attractors. *Physical Review Letters*, 110(23), JUN 7 2013.
- [63] A. Scotti. Inviscid critical and near-critical reflection of internal waves in the time domain. *Journal of Fluid Mechanics*, 674:464–488, MAY 2011.
- [64] D. N. Slinn and J. J. Riley. Turbulent mixing in the oceanic boundary layer caused by internal wave reflection from sloping terrain. *Dynamics of Atmosphere and Oceans*, 24(1-4):51–62, JAN 1996. 4th International Symposium on Stratified Flows.
- [65] K. Snow and B. R. Sutherland. Particle-laden down a slope in uniform stratification. *Journal of Fluid Mechanics*, 755, SEP 2014.
- [66] J. Sommeria. *Uvmat toolbox for matlab*. LEGI/CNRS-UJF-INPG, <http://coriolis.legi.grenoble-inp.fr>.
- [67] B. R. Sutherland. *Internal Gravity Waves*. Cambridge University Press, 2010.
- [68] B. R. Sutherland, S. B. Dalziel, G. O. Hughes, and P. F. Linden. Visualization and measurement of internal waves by 'synthetic schlieren'. Part 1. Vertically oscillating cylinder. *Journal of fluid mechanics*, 390:93–126, 1999.
- [69] S. A. Thorpe. On the interactions of internal waves reflecting from slopes. *Journal of Physical Oceanography*, 27(9):2072–2078, SEP 1997.
- [70] C. Tropea, A. L. Yarin, and J.F. Foss. *Springer Handbook of Experimental Fluid Mechanics*. Springer, 2007.
- [71] P. Wang. *Principles of Tidal Sedimentology*. Springer, 2012.
- [72] C. Wunsch. Progressive internal waves on slopes. *Journal of Fluid Mechanics*, 35(1):131–&, 1969.
- [73] C. Wunsch. Some Reynolds stress effects of internal waves on slopes. *Deep-Sea Research*, 18(6):583–&, 1971.
- [74] C. Wunsch and R. Ferrari. Vertical mixing, energy, and the general circulation of the oceans. *Annual Review of Fluid Mechanics*, 36:281–314, 2004.
- [75] K. Y. Yick, C. R. Torres, T. Peacock, and R. Stocker. Enhanced drag of a sphere settling in a stratified fluid at small Reynolds numbers. *Journal of Fluid Mechanics*, 632:49–68, AUG 10 2009.
- [76] H. P. Zhang, B. King, and Harry L. Swinney. Resonant generation of internal waves on a model continental slope. *Physical Review Letters*, 100(24), JUN 20 2008.

Abstract

Internal waves are produced as a consequence of the dynamic balance between buoyancy and gravity forces when a particle of fluid is vertically displaced in a stably stratified environment. Geophysical systems such as ocean and atmosphere are naturally stratified and therefore suitable for internal waves propagation. Furthermore, these two environments stock a vast amount of particles at their boundaries and in their bulk. Therefore, internal waves and particles will inexorably interact in these systems.

In this work, exploratory experiments are performed to study wave generated erosive transport of particles. In order to determine a transport threshold, the peculiar properties of internal waves (“critical reflection”) are employed to increase the intensity of the wave field at the boundaries. A method was developed in collaboration with a signal processing team to improve the determination of the wave components involved in near-critical reflection. This method enabled us to compare our experimental results with a theory of critical reflection, showing good agreement and allowing to extrapolate these results to experiments beyond ours and to oceanic conditions.

In addition, we study the interaction of internal waves with a column of particles in sedimentation. Two main effects are observed: the column oscillates around an equilibrium position, and it is displaced as a whole. The direction of the displacement of the column is explained by computing the effect of the Lagrangian drift of the waves. This effect could also explain the frequency dependence of the displacement.

Résumé

Les ondes internes sont produites par suite de l'équilibre dynamique entre les forces de flottabilité et la gravité quand une particule de fluide est déplacée verticalement dans un milieu stratifié stable. Les systèmes géophysiques tels que océan et l'atmosphère sont naturellement stratifiés et donc favorables à la propagation des ondes internes. En outre, ces deux environnements stockent une grande quantité de particules tant dans leur intérieur que sur les bords. Par conséquent, les ondes internes et les particules vont inévitablement interagir dans ces systèmes.

Au cours de ce travail, des expériences exploratoires sont réalisées pour étudier le transport par érosion des particules, généré par les ondes internes. Afin de déterminer un seuil de transport, les propriétés particulières des réflexions d'ondes internes («réflexion critique») sont utilisées pour augmenter l'intensité du champ d'ondes à la surface de réflexion. Une méthode a été développée en collaboration avec une équipe de traitement du signal pour améliorer la détermination des composantes de l'onde impliquées dans une réflexion quasi critique. Cela nous a permis de comparer nos résultats expérimentaux avec une théorie de la réflexion critique, montrant un bon accord et permettant d'extrapoler ces résultats à des expériences au-delà de la nôtre et à des conditions océaniques.

Nous avons aussi étudié l'interaction des ondes internes avec une colonne de particules en sédimentation. Deux effets principaux ont été observés : la colonne oscille autour d'une position d'équilibre, et elle est déplacée dans son ensemble. La direction du déplacement de la colonne est expliquée par le calcul de l'effet de la dérive Lagrangienne produite pour des ondes. Cet effet pourrait également expliquer la dépendance en fréquence du déplacement.
